ALMA MATER STUDIORUM · UNIVERSITÀ DI BOLOGNA

SCUOLA DI INGEGNERIA E ARCHITETTURA
CORSO DI LAUREA MAGISTRALE IN INGEGNERIA BIOMEDICA (LM)

TESI IN
MODELLI E METODI PER LA CARDIOLOGIA
COMPUTAZIONALE LM

Multiscale analysis of an HCN4 channel double mutation in a human sinoatrial computational model

Relatore:
STEFANO SEVERI
Correlatori:
FILIPPO CONA
ALAN FABBRI

Candidato:
EUGENIO RICCI

SESSIONE III
ANNO ACCADEMICO 2018/2019

Ai miei genitori

Contents

Abstract

The Double Mutation (DM) I479V/A485E has been reported (Servatius et al., 2018) to determine a loss of function of the funny current (I_f), which is a key player of the onset of the action potential in the Sinoatrial Node (SAN). Thus, the DM can result in bradycardia. This work presents a multiscale study that links the DM (i.e. genotype) to the bradycardia (i.e. phenotype). To do this, first a tool to display and analyse electrophysiological data was developed. Thanks to it, the decrease in I_f conductance was quantified and used as an input for a computational model of a human SAN cell. The simulation of the action potential of this model gave a Cycle Length (CL) of 1019 ms (compared to 814 ms of the Wild Type condition, +20.1 %). After this, a 1D and 2D model of the SAN were implemented, in order to test the behaviour of more complex systems (fibre and tissue), since these can show phenomena not present at the channel or single cell level. Several values of cellular heterogeneity (σ) and coupling (ρ) were considered, in order to investigate the most physiologic degree of these properties. This was assessed relying on the most realistic results obtained for CL, Action Potential Amplitude (APA) and Conduction Velocity (CV). The results show that:1) increasing σ leads to shorter mean CLs and wider CL and APA distributions; 2) increasing ρ provides wider CL and APA distributions, whereas their mean values are the highest for $\rho = 1000$ M$\Omega \cdot$m. A complete synchronization is therefore a trade-off between σ and ρ; 3) for physiological values of σ (0.1873) and ρ (~ 100 M$\Omega \cdot$m) cells manage to synchronize their pacing frequency and show a conduction velocity similar to that reported in literature ($\sim$ 11 cm/s) in both 1D and 2D models. This is true for both WT and DM but, in the last case, the mean CL is significantly shorter. This fact proves the detrimental effect of these mutations: in 2D, the heart rate drops from 75.6 bpm (WT) to 60.2 bpm (DM, -18.3 %).

Introduction

The sinoatrial node (SAN) has been known to be the spot from which the electrical pulse originates in the heart for a very long time ([1], [2] and [3]). In physiological conditions indeed, the SAN is able to deliver a stimulus to the right atrium and, through it, to the entire heart. This is possible since the cells found in the sinoatrial node present autorhythmicity, i.e. they can depolarize - up to the threshold value at which the action potential is triggered - without any external stimulus. Other kinds of cardiomyocytes (e.g. atrioventricular node cells, His bundle cells and Purkinje fibers cells) also present autorhythmicity, but at a lower frequency. For this reason, the stimulus coming from the SAN prevails, making the latter the responsible for the normal heart rate.

The self-pacing ability in the SAN is guaranteed by the sum of many mechanisms that underlie the onset of the action potential (AP), which is a change in the membrane voltage, V_m. The start of this mechanism is given by the activation of the funny current (I_f) at low potentials, that causes the SAN cells to depolarize (by the intake of Na^+ ions) without any external inputs. The growth in membrane potential makes the Ca^{2+} channels (first the T-types, then the L-type) to open, letting calcium ions enter the cell and further depolarize it. The outward K^+ current will at the end hyperpolarize the cell, bringing it at low potentials, where the cycle restarts. Unlike other types of cardiomyocytes, the role of the Na^+ current (I_{Na}) was thought to be secondary in the SAN because of the slower rise in the AP upstroke. However, a recent work by Li et al. [4], resized this belief by proving that a block of this current impairs the functioning of the SAN, especially in diseased hearts. Therefore I_{Na} seems to be fundamental also in the sinoatrial node, particularly for what it concerns the AP conduction.

In the heart, the conduction of the AP is guaranteed thanks to the connection among the cells through the intercalated discs. The electrical coupling is provided by the gap junctions through which ions can flow, thus propagating the stimulus from one cell to the other. As already said indeed, the electrical pulse originates in the SAN and travels through the atria up to the AV node, the only excitable path connecting the atria to the ventricles. From here, and through the His bundle, the stimulus arrives to the Purkinje fibers, from which it is delivered to the

whole ventricles. Indeed, the action potential (in the heart but also in neurons) is the mechanism that nature has developed in order to deliver information at long distances. In this case, the propagation of the change of the membrane potential (the aforementioned information) is coupled with the release of calcium from the sarcoplasmic reticulum, that makes possible the binding of the filaments of actine and myosine and thus the contraction of cardiac tissue.

Despite of the complexity of the mentioned mechanism and the specialization of the tissues involved, the normal function of the heart can in some cases be altered by many diseases, such as arrhythmias. In order to predict and treat these pathologies, a deep understanding of the physiology of the SAN is necessary. Unluckily however, few structural and physiological experimental data are available for the human SAN, since few studies explanted and analysed this very small (12-29.5 mm in length, 3.3-6.7 mm in width and 1-1.8 mm in depth [5]) and complex-shaped tissue. This is because, apart from the technical difficulties of explanting and preserving an intact SAN, it is hard to have available such a precious human tissue in a good condition.

Computational models and computer simulations can therefore provide a valuable solution to this deficiency, since they allow to test hypothesis and to suggest new ones, without the necessity of handling human tissue. This was demonstrated by Joyner et al. [6], who used a computational model to explain how a small number of SAN cells can drive all the atrium by keeping a balanced source-sink relationship. From the very first work of Hodgkin and Huxley [7], which opened the era of the mathematical description of ionic currents, many steps forward have been made in the direction of an accurate mathematical modeling of the electrophysiology of the heart. The history of this progress, and what has been so far understood, can be found in the works of Denis Noble [8] and Yoram Rudy [9], respectively. Many models have indeed been proposed in the past for every type of cardiomyocytes (sinoatrial, atrial, ventricular, Purkinje fibers), especially for animal APs (since there are more electrophysiological data available). The single cell models have also been extended to 1D and 2D models, in order to study the propagation between different cells and the effects of both gap junction coupling and cellular heterogeneity. Very importantly indeed, the main aspect of the action potential is that it is not a phenomenon driven by a single factor. Instead, it appears as a complex mechanism to which lower-level events participate in different extent. This concept is known as *emergent behaviour*: only at higher levels (i.e.: tissue or organ level) it is possible to appreciate phenomena not present at smaller scales (e.g.: channel or cell level), since they are the result of many combined factors. The AP and its conduction are examples of emergent behavior as all of the cellular currents contribute to the functioning of the first one and the second one is the result of the interaction between many different cells.

The starting point of this thesis is the study by Servatius, Porro et al. [10]. This work presented the case of a patient with a double HCN4 channel isoform mutation, which provided an almost complete loss of function of the I_f current in a HEK-293 cellular line (that only expressed this type of channel). As it is known from literature, a loss of function in I_f determines a decrease in the heart rate; the patient reported in the study showed indeed a deep bradycardia. The aim of this thesis is therefore to assess this bradycardic effect on systems of increasing complexity: single channel, single human SAN cell, SAN fiber (1D model) and SAN tissue (2D model). This is in order to study the mutations in more physiologic conditions, taking for example into account the cellular heterogeneity at the fiber and tissue level, to see if their consequences are different from those observed in a single cell. Indeed, the interaction between cells with different properties can show phenomena that are not predictable at the single cell level.

This work therefore started from the assessment of the effects at the channel level, by developing a Graphical User Interface (GUI) that could serve as a tool for analysing electrophysiological data. The data of the cited study were analysed in order to obtain the parameters (specifically the conductance of the funny current, g_f) with which to feed a computational model of the human SAN cell. The single cell model by Fabbri et al. [11] was used to evaluate the consequences of the mutations on the whole cell. Finally, starting from the single cell model, 1D and 2D human SAN models were implemented in MATLAB and simulated (at several levels of cellular heterogeneity and coupling) taking advantage of the computational power offered by the GPUs.

The thesis is divided in two parts: Part I illustrates the building of the graphical user interface (GUI) and the analysis of *in vitro* data regarding the characterization of loss of function of HCN4 channels. Part II reports the *in silico* experiments carried out to observe the effects of the HCN4 at tissue level. In Part I, Chapter 1 will discuss the SAN anatomy and physiology, the HCN4 channel structure and the mathematical modeling of the SAN. Chapter 2 will present the Elements Read GUI tool, realized during an internship at Elements srl, and the results that could be achieved thanks to it (in terms of the evaluation of the effects of the mutations on the I_f current). The effects of the mutation at the single cell level are also presented. In Part II, Chapter 3 will explain how the 1D and 2D models were designed and obtained, whereas in Chapter 4 the results of these models will be shown and discussed. Finally, Chapter 5 will summarize and highlight the most interesting results of the whole work.

Part I

Chapter 1

The sinoatrial node

In this Chapter the anatomy and physiology of the sinoatrial node, with special attention to its structure-function relationship, will be briefly presented. Also, the mathematical description of SAN cells will be discussed, with reference to the work of Fabbri et al. [11]. Finally, the structure and the importance of the HCN channel family (and specifically of the HCN4 isoform) will be discussed.

1.1 Structure-function relationship of the SAN

The sinoatrial node "is a compact mass of specialized cardiomyocytes enmeshed in a dense matrix of collagen, fibroblasts and fatty tissue" [5]. It is located in the intercaval region of the right atrium, adjacent to the crista terminalis, a muscular tissue. Its dimensions (12-29.5 mm in length, 3.3-6.7 mm in width and 1-1.8 mm in depth), and its banana-like shape, are quite agreed upon, but many micro-structural aspects are still debated [5].

The main dispute concerns the way the SAN is electrically connected to the right atrium: some researchers think that the stimulus is delivered thanks to discrete SinoAtrial Conduction Pathways (SACPs) , whereas other state that the SAN is entirely connected to the atrial tissue through diffuse interdigitations. This is a crucial topic, since the structure of the SAN deeply influences its function, namely its pacemaking activity. Evidence of both hypotheses have been proposed in the past ([13]), but lately many works ([5], [17]) provided proofs in favour of a discrete conduction system. In the study of Csepe et al. [5], an integrative approach combining functional and structural analysis at high resolution, allowed them to identify different SACPs in the SAN of two human hearts - one healthy and one diseased. This was achieved thanks to high-resolution optical mapping and 3D computer reconstruction of the SAN complex. As can be seen from Figure 1.2a, these evidences are both histological and functional, since the existence of SACPs

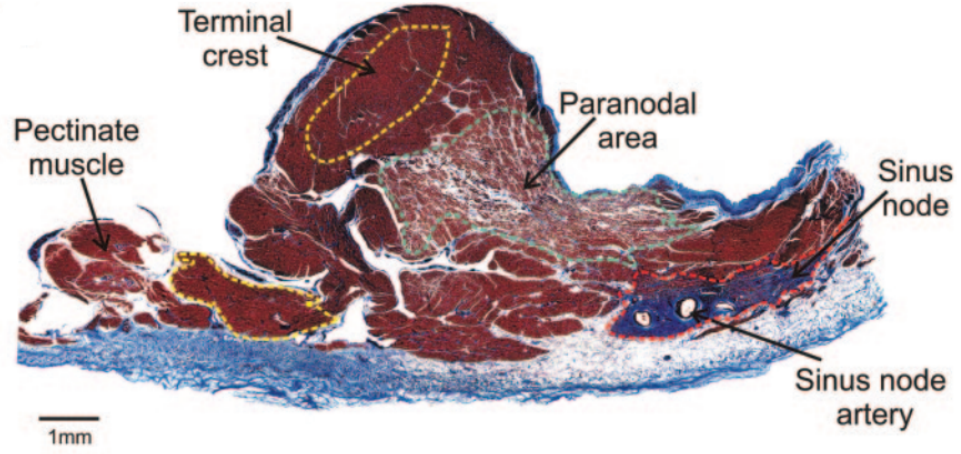

Figure 1.1: Histological section of the SAN [12].

allows to explain the different sites through which the electrical stimulus is delivered by the SAN to the atrium. Despite this, the authors report how the functional block zone correlates to the anatomical border (made of fibrosis, fat, discontinuous myofiber) in a degree dependent from the region considered. Therefore, the alternative hypothesis of an extensive connection between sinoatrial node and atrium can not be discarded, as precisely no evidence of the complete insulation of the structural border has been obtained so far. Nevertheless, for Li et al [17] SACPs allow to explain how the SAN maintains its pacemaking function even in pathological condition: by blocking signals coming from the atrium during fibrillation, they protect the SAN from overdrive suppression.

Another important characteristic of the SAN, for what it concerns its function, is its heterogeneity: this highly specialized tissue is not homogeneous, but on the contrary presents a transition from central SAN cells to atrial ones. Also in this case, two theories have been proposed, as can be seen in Figure 1.3. The first hypothesis, called the "mosaic" model (Figure 1.3a), suggests that the density of SAN cells decreases away from the center, while at the same time the number of atrial ones grows. For the second hypothesis, known as the "gradient" model (Figure 1.3b), there is a progressive transition in cellular properties from the SAN center to the crista terminalis [18].

A study from Inada et al. [14], reports these trends in the rabbit SAN according to the gradient model:

- *Dimensions*: central cells are smaller ($\sim 63\ \mu m$ in length, $C_m \sim 40\ pF$), whereas peripheral ones are bigger ($\sim 101\ \mu m$, $C_m \sim 64\ pF$);

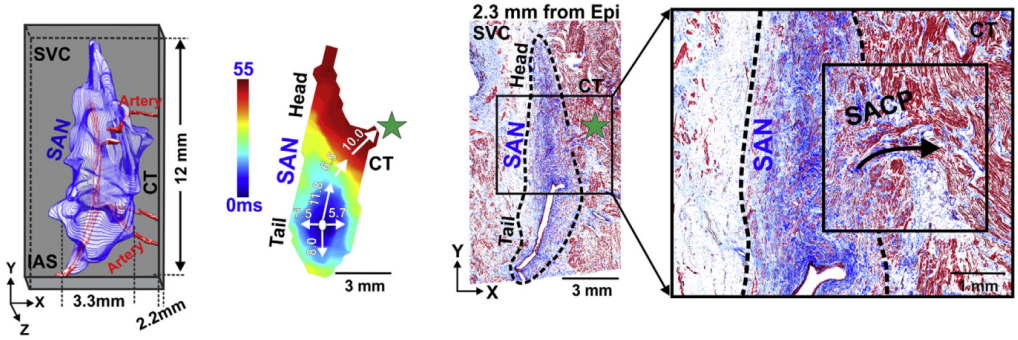

(a) 3D reconstruction of the SAN, functional and histological SACPs evidences of a healthy heart.

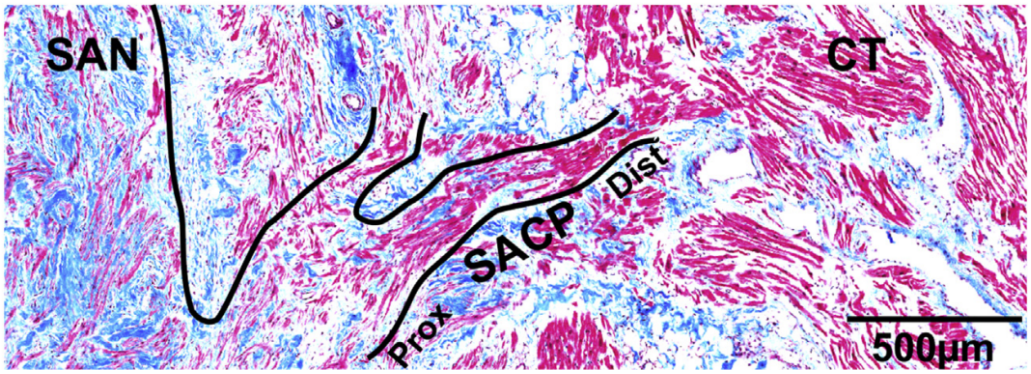

(b) Zooming of the SACP complex.

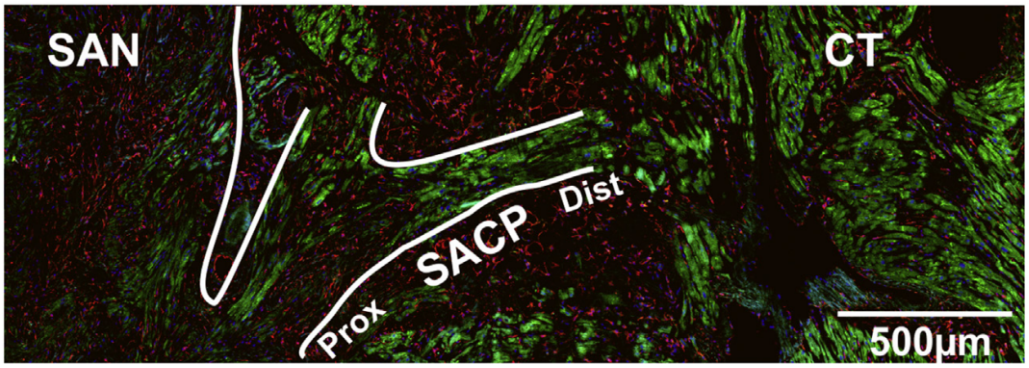

(c) Distribution of the Cx43 connexin along the SACP.

Figure 1.2: Results of the study from Csepe et al. [5].

- *Maximum upstroke velocity* (dV_m/dt_{max}): this parameter is low in central cells ($\sim 2\,V/s$), but rises in the periphery ($\sim 50\,V/s$);

- *Maximum Diastolic Potential (MDP)*: central cells are more depolarized (MDP $\sim -60\,mV$) with respect to the peripheral ones, which have a more negative MDP ($\sim -75\,mV$).

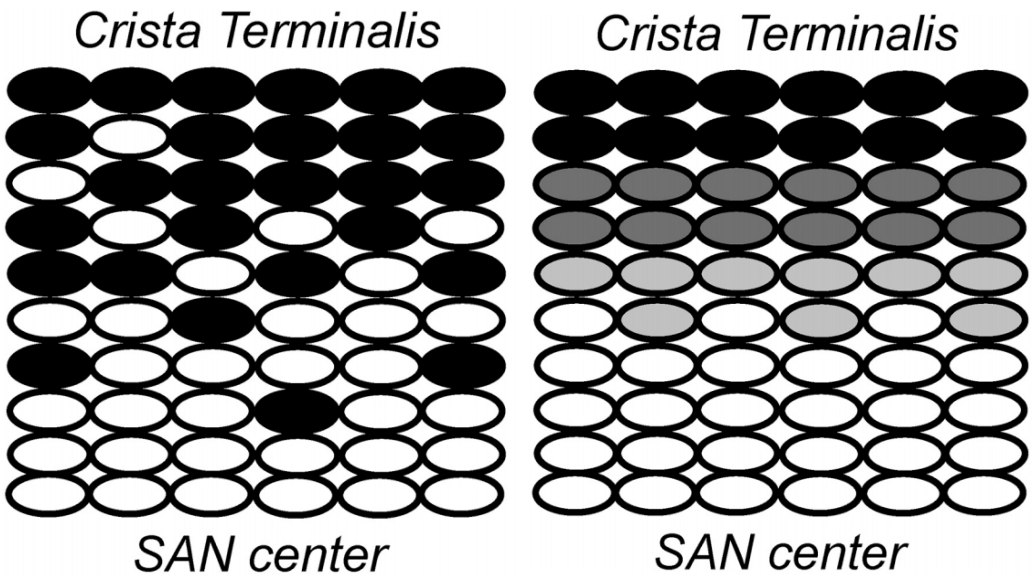

(a) Mosaic model. *(b) Gradient model.*

Figure 1.3: Main theories for the transition in cellular properties from the SAN to the atrium: (a) Mosaic model, (b) Gradient model [18].

- *Gap junctions*: conductance is low ($0.5-25$ nS) at the center of the SAN, compared to that in the atrium ($30-635$ nS). This is because electrical coupling is granted in the atrium by Cx43 and Cx40 connexin isoforms, which respectively form medium ($60-100$ pS) and high conductance gap junctions. In the center of the SAN, Cx43 and Cx40 are not expressed, leaving the place for the low conductance Cx45 ($20-40$ pS). This also causes the conduction velocity (CV, in cm/s) to be low in the center (~ 2 cm/s) and high in the atria (~ 70 cm/s). Peripheral cells are coupled via both Cx43 and Cx45 and therefore show halfway properties (~ 30 cm/s).

Regarding human SAN, new CV measures were found in literature: while Riera et al. [15] and Desplantez et al. [16] reported indicative values of 5 and 3-5 cm/s respectively, Fedorov's group reported a CV of 11.8 ± 3.1 cm/s in a healthy heart [5]. This value was obtained thanks to a voltage activation map using a high-resolution near-infrared optical mapping, and showed a substantial decrease in a diseased heart: 3.6 ± 1.1 cm/s.

Going back to the transition theories, the fact that central cells show a lower conductance is because they have to be uncoupled from the atrium, because otherwise the latter would have an inhibitory effect on them: the lower MDP and the significant load it represents, would cause the SAN to fail in the rhythm generation ([13], [14]). Thus, in silico simulations show how a transition layer of cells

with a bigger expression of I_{Na} and a stronger cell-to-cell coupling, is needed in order to supply enough depolarizing current to the whole atrium and to deliver it efficiently. For these reasons, peripheral cells show a higher expression of $Nav1.5$ (an I_{Na} channel subunit) and $Cx43$ [14]. This study also proposes a cause to the absence of I_{Na} in central cells: AP of Purkinje fibres relies on I_{Na}, and for this reason they can be subject to overdrive suppression. This means that if a high-frequency source (such as an ectotopic focus) stimulates them, their activity is interdicted, since intracellular Na^+ concentration grows and therefore $Na^+ - K^+$ pump current rises. Being this current an outward (hyperpolarizing) current, it prevents the cells from depolarizing, blocking the onset of the AP. To avoid this potentially lethal mechanism, pacemaking activity in the SAN centre is entrusted to I_{CaL} instead of I_{Na} [14].

Despite this, the role of I_{Na} in the SAN seems to be crucial, especially in diseased hearts. As reported by a recent study [4] indeed, voltage-gated sodium channels (Nav) are fundamental in preventing conduction failure. If blocked, both cardiac and neuronal Nav isoforms ($cNav$ and $nNav$) lead to beat-to-beat variability and reentry by impairing and depressing nodal conduction. These conditions can bring to Sinus Node Dysfunction (SND), which can only be treated with pacemaker implantation. This disease has indeed been linked to loss-of-function mutations in $SCN5A$ [14], the gene encoding for the cardiac $Nav1.5$ channel subunit. Although this gene is more expressed in the atria (Figure 1.4a) than in the SAN, its block via tetrodotoxin (TTX) or the administration of adenosine to mimic a stress condition, caused rhythm generation failure, thus highlighting its roles in pacemaking and conduction. $nNav$ is more abundant in the SAN instead (Figure 1.4b), and its blocking showed an increased probability of failure in intranodal conduction.

In conclusion, these facts demonstrate an only suspected importance of I_{Na} in the SAN, even though its implications, and the whole SAN functioning, have not been fully understood yet.

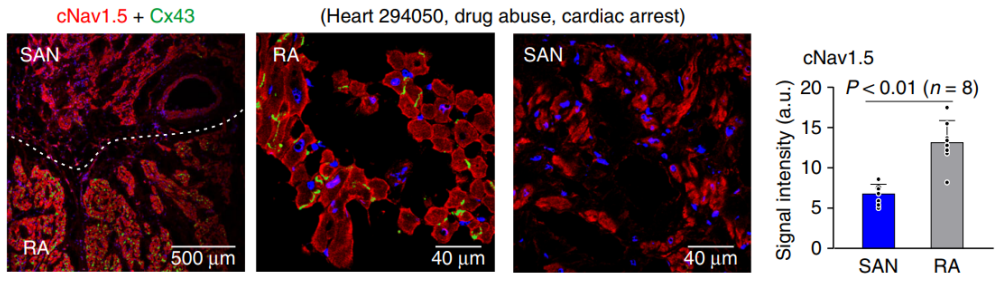

(a) cNav expression in the SAN and right atrium.

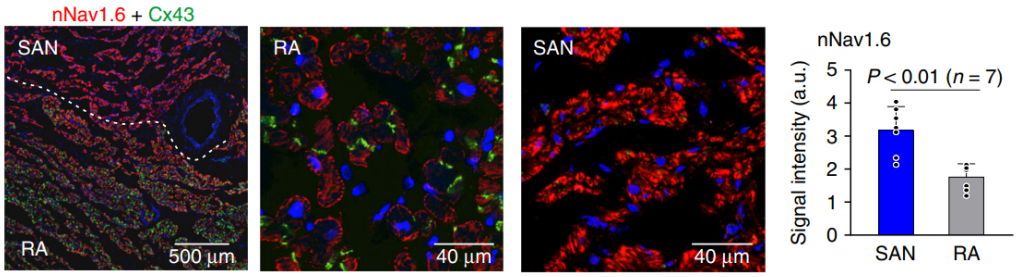

(b) nNav expression in the SAN and right atrium.

Figure 1.4: I_{Na} genes expression in SAN and atrium [4].

1.2 Mathematical modeling of the SAN

The action potential generation is a complex and dynamic phenomenon. In the sinoatrial node, three phases of the action potential can be distinguished [15], as shown in Figure 1.5:

- **Phase 4**: spontaneous diastolic depolarization, due to the slow intake of Na^+ and K^+ (I_f current) and Ca^{2+} (I_{CaT}) ions. This phase ends with the AP triggering, when V_m is in the range of -40/-30 mV;

- **Phase 0**: depolarization phase, driven by Ca^{2+} currents: L-type channels - which are activated at higher potentials with respect to the T-type ones - determine the upstroke. In addition, L-type current is also important in the other types of cardiomyocytes, since it is responsible for the plateau phase. In working cardiac myocytes (atrial and ventricular), Phase 0 is instead due to I_{Na} which, having faster kinetics and a larger maximum current, determines a steeper upstroke with respect to that of SAN cells;

- **Phase 3**: repolarization phase, characterized by the closing of L-type calcium channels, and the rise of rectifying potassium currents (I_{Kr} and I_{Ks}).

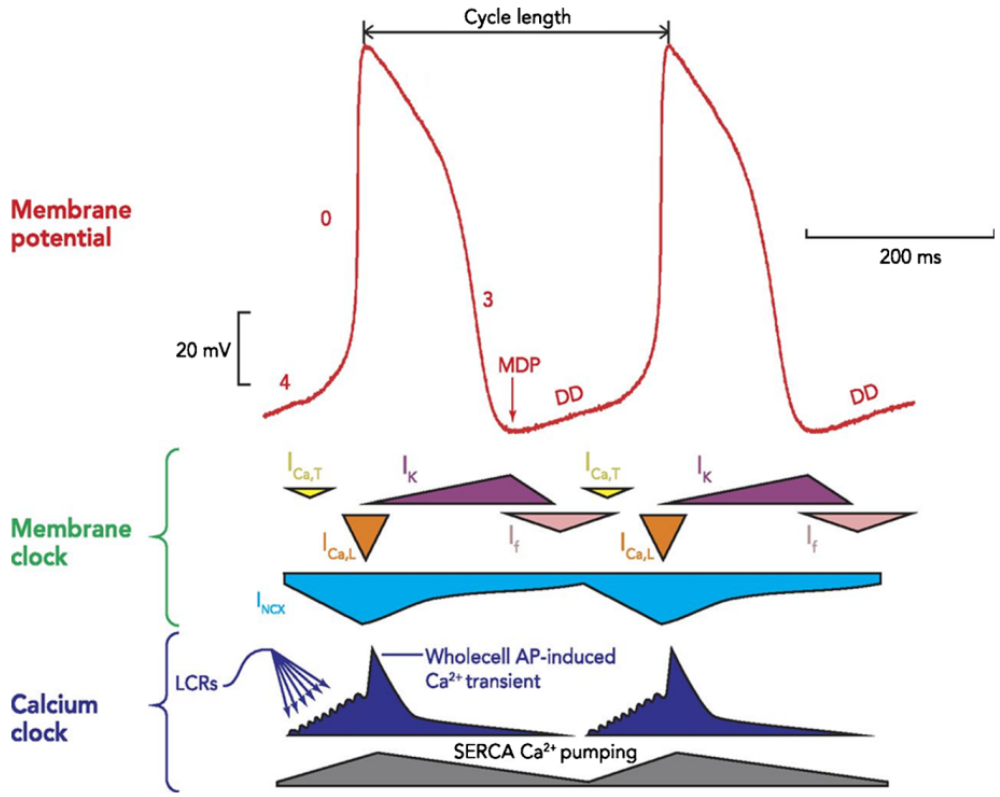

Figure 1.5: Action potential of the rabbit SAN (red trace) and involved currents for both membrane clock (green bracket) and calcium clock (dark blue bracket) theories (LCRs: Local Calcium Releases). The three phases of the sinoatrial AP are also labeled. [19].

The autorithmicity lies in the spontaneous depolarization during phase 4 of the AP. Two theories have been proposed to explain this phenomenon: one is called the *membrane clock* and it is the oldest and most accepted one, even if it has been lately questioned by a novel hypothesis, named *calcium clock*. The first says that: I) all of the involved mechanisms are located in the membrane; II) diastolic depolarization is mainly due to the I_f current, which is responsible of bringing V_m to the threshold value at which the AP is triggered. For this reason, I_f is believed to determine the heart rate. The latter theory resizes the role of both the membrane and the funny current, in favour of the rhythmic and spontaneous Local Calcium Releases (LCRs, mediated by the ryanodine receptors) from the sarcoplasmic reticulum ([19], [20]). This release brings into play the $Na^+ - Ca^{2+}$ (NCX) exchanger, and can therefore change the membrane voltage and trigger the AP. So far, it is not clear what the predominant mechanism is; however, the membrane clock and the calcium clock are closely related, since they can both

modify the membrane potential.

In addition to this still debated issues, many more aspects contribute to the complexity of the physiology of the SAN. Examples can be: I) the heart rate modulation from the sympathetic and parasympathetic nervous system and II) the fail-safe mechanisms that protects the SAN from failure. All these considerations make a full mathematical description of the SAN very difficult, even because there is little anatomical and electrophysiological data available for humans. Consequently, many models are based on animal (especially rabbit) data, and therefore represent more or less good approximations of what happens inside the human heart.

Thus, the lack of human data make in silico simulations of utmost importance to advance in our understanding of the physiology of the heart. This work indeed proposes a new 1D and 2D computational model of the human SAN, based on the single cell model by Fabbri et al. [11], in order to shed light on the mechanisms responsible for the generation of the heart rate and the conduction of the electrical signal.

1.2.1 Fabbri model

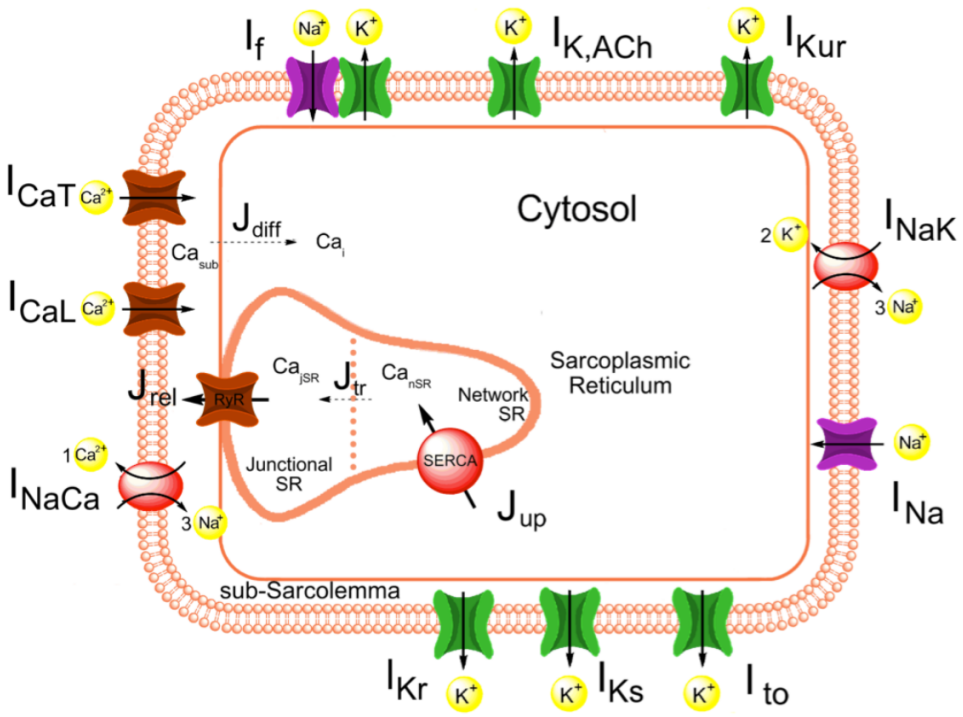

Figure 1.6: Schematic diagram of the human SAN Fabbri model [11].

The human single cell SAN model was based on the Severi-DiFrancesco rabbit SAN cell model [21] and updated including human data and automatic optimization to better reproduce the electrical activity of the human SAN.

The result reproduced indeed the main features of the AP in the SAN, according to literature [11]:

- *Cycle length*: 814 ms compared to 828 $\pm$ 21 ms found in literature;
- APD_{90}: 161.5 vs 143.5 $\pm$ 49.3 ms;
- DDR_{100}: 48.1 vs 48.9 $\pm$ 25.4 mV/s;

The mechanisms of pacemaking are mainly explained thanks to the role of I_f, which manages to drive the diastolic depolarization and to participate to vagal and adrenergic stimulation together with $I_{K,ACh}$ and I_{CaL}, respectively. The role of the *calcium clock* was considered to be minor, since the work by Himeno et al. [22] showed how an impairment of this mechanism (through chelation of cytosolic Ca^{2+}) did not affect the heart rate in guinea pig SANs. Despite the importance of the funny current, other actors are included in this mathematical description of the human SAN (see Figure 1.6):

- I_{CaL}, responsible for the upstroke and the sympathetic stimulation;
- I_{CaT}, responsible for the early diastolic depolarization;
- $I_{K,ACh}$: modulates the parasympathetic stimulation;
- I_{Kr} and I_{Ks}: repolarizing (outward) currents;
- I_{Na}: depolarizing current. Even if it is less expressed in the SAN with respect to the atria, its importance is still debated (as discussed in section 1.1);
- I_{Kur} and I_{to}: outward potassium currents. Of secondary importance in the SAN;
- $Na^+ - K^+$ *pump* and $Na^+ - Ca^{2+}$ *exchanger*. These complexes help to repolarize the cells, by restoring the original ionic concentrations;
- J_{rel}, J_{tr} *and* J_{up}: these calcium current densities take into account respectively: I) the Ca^{2+} release from the Junctional Sarcoplasmic Reticulum (JSR); II) the transfer of Ca^{2+} ions from the Network Sarcoplasmic Reticulum (NSR) to the JSR and III) the uptake of Ca^{2+} from the cytosol to the NSR;

– *Cellular compartments*: the cell is divided in four compartments, namely: subsarcolemma, cytosol, junctional sarcoplasmic reticulum (JSR) and network sarcolplasmic reticulum (NSR), that can be physically (e.g.: sarcoplasmic reticulum) or virtually (subsarcolemma and cytosol) separated one between another. The latter case, as for the sub-sarcolemmal space and the transition from NSR to JSR, reflects a different behaviour in ionic dynamics with respect to other compartments.

To conclude, the model consists of 33 first-order, non-linear differential equations, which are responsible for the updating of the state variables (such as V_m, gating variables and ionic concentrations).

1.3 HCN channels

1.3.1 Structure and physiology

Hyperpolarization-activated cyclic nucleotide-gated cation (HCN) channels are part of the voltage-gated cation channels super-family. Four isoforms constitute these channels: HCN1, HCN2 and HCN4 have been found in both heart and brain, whereas HCN3 seems to be specific of neurons. For what it concerns the heart, HCN channels have shown to be the molecular corresponding of the I_f current, which has been known to have a primary role in autorhythmicity for a long time [23]. In fact, HCN channels have the properties of the "funny channels" [24]:

1. They open upon membrane hyperpolarization, contrarily to most voltage-gated channels;

2. They are permeable to both Na^+ and K^+ ions (with a P_{Na}/P_k ratio of $\sim$ 0.15-0.4); the glycine-tyrosine-glycine (GYG) sequence (Figures 1.7a and 1.7b) is indeed shared with potassium channels. This does not mean that they are non-selective, since they are impermeable to Li^+ and to divalent anions or cations. Furthermore, they can be blocked by extracellular Cs^+. Their reversal potential (that can be computed with the Goldman-Hodgkin-Katz (GHK) equation) is around -25 mV and the current is therefore inwardly directed at rest (-65/-75 mV), thus bringing V_m toward threshold;

3. They are modulated by cyclic adenosine monophosphate (cAMP), which accelerates their activation kinetics and shifts their V_{50} to more positive potentials, resulting in a faster and deeper opening of the channel and consequently in a higher pacemaking frequency (especially for HCN2 and HCN4).

HCN channels isoforms are formed by six helices (S1-S6) spanning through the cellular membrane (Figure 1.7a). Unit S4 is positively charged and acts as a voltage sensor; S5 and S6 instead, represent the pore-forming helices. Another important feature is the cyclic nucleotide binding domain (CNBD) in the C terminus, which is responsible for the interaction with cAMP. The central region of these channels is shared by all the four isoforms, whereas the N and C terminus vary in a higher measure, thus determining a difference in the properties of the isoforms. HCN1 has indeed the fastest kinetics (τ between 25-300 ms), followed by HCN2 and HCN3 (180-500 ms). HCN4 is the slowest isoform: its time constant spans from hundreds of milliseconds at low potentials (-140 mV), to many seconds at less negative voltages (-70 mV). V_{50} varies in a wide interval (from -73 to -103 mV). Also the senstivivity to cAMP is different between the isoforms: this molecule deeply shifts V_{50} of HCN2 and HCN4 as already explained, whereas HCN1 is immune to its action. Despite of this, ion selectivity and pharmacological response are quite similar between the four isoforms [24].

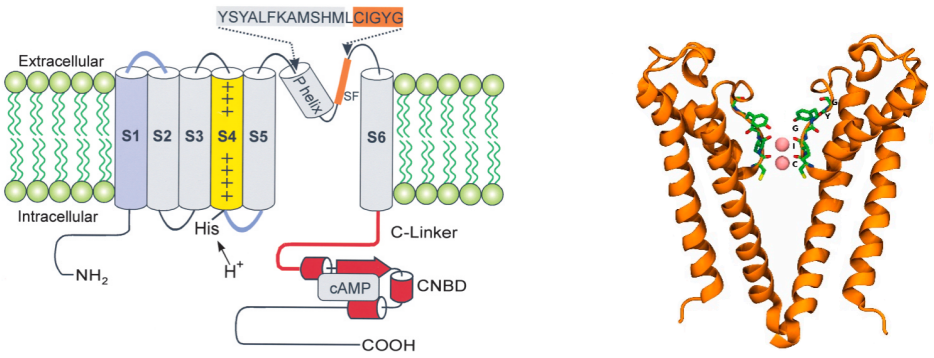

(a) (b)

Figure 1.7: (a) Structural model of HCN channels [24]; (b) HCN channel filter structure: weak K^+ selective filter [25].

I_f channels are made of 4 HCN subunits, thus constituting tetrameric complexes. Potentially, the same isoforms could build an entire channel, but more probably different isoforms contribute to its structure. This is because, as reported by Altomare et al. [26] for the rabbit, the channels responsible for I_f show properties far from those of specific isoforms (HCN1 and HCN4 in particular, since they are the more expressed isoforms in the rabbit SAN). However, heteromeric channels - formed by both HCN1 and HCN4 - reproduce more faithfully the electorphysiological features of I_f channels, thus suggesting that they are indeed heteromeric structures.

Two hypotheses have tried to explain the gating mechanisms of HCN channels [24]. One states that their function is similar to that of K^+ channels (e.g.:

hERG channel): the opening is the result of the recovery from the inactivation. The alternative model proposes the activation from a closed state as the explanation. This latter theory suggests that the mechanism is the opposite of what happens in depolarization-activated channels: the channel is closed at positive voltages when S4 is in its outermost configuration, whereas it would be open in depolarization-activated channels. The coupling between S4 and channel gate has - for this hypotheses - an inverted polarity in HCN channels. Furthermore, the speed of channel opening seems to be mainly determined by S1 and S1-S2 linker activity.

HCN4 is the more expressed isoform in murine and rabbit SAN, followed by HCN1 and HCN2. Regarding humans, similar results were obtained by Chandler et al. [12], but Li et al [27] highlighted that HCN1 had a major expression ratio between SAN and atria compared to HCN4 and HCN2, thus suggesting its importance in the SAN. The importance of HCN4 in the spontaneous activity of the SAN is out of question, since its mutations greatly affect the pacemaking activity [27], as the next section (1.3.2) will further analyse.

HCN isoforms structure and kinetics are almost identical in all mammals. This brings to the conclusion that, in order to obtain the wide range of heart rates (from $\sim$ 600 bpm in mice, to $\sim$ 70 in humans) seen in mammals, it is necessary to act on both the expression and up/down-regulation of HCN and other AP-related channels, rather than on their structure [24].

1.3.2 HCN4 mutations

As already mentioned, HCN4 is the most important HCN channel isoform in the human SAN, since the funny current (i.e. the main player of autorhythimicity) flows through it. Mutations in the HCN4 gene are therefore critical, as they may lead either to a loss or a gain of function in the channel, thus determining bradycardia or tachycardia respectively.

The way a mutation can affect a cellular current is dual. On one hand, the channel structure can be changed, so that it does not work as it should, due to a functional impairment. On the other hand, the complex process of transcription from the genes to the 3D channel (trafficking) fails at some point, and as a result the channel is not even present in the plasmatic membrane. The latter mechanism is the most frequent.

HCN4 mutations have been linked to pathological conditions such as bradycardia and sinus node dysfunction (SND). Verkerk et al. [28] report 22 HCN4 known mutations in humans up to 2015, that can cause insensibility to cAMP, shift of V_{50} towards hyperpolarization and reduced expression of the channels. All this changes resulted in the reduction of I_f, thus leading to the mentioned pathologies.

In 2018 two new mutations were reported and analyzed by Servatius, Porro et al. [10]: I479V and A485E, affecting the pore loop region between the S5 and S6 transmembrane helices, which contain the highly conserved CIGYG selectivity filter sequence of the HCN4 channel (Figures 1.7a and 1.7b). One of the aims of this thesis work is therefore that of providing more proof of the correlation between the genotype (these mutations) and the phenotype (the bradycardia of the patient, in this case).

Chapter 2 will show how electrophysiological data of HCN4 channels were analyzed in order to obtain parameters for in silico simulations, followed by the results of these simulations.

Chapter 2

Elements Read GUI: a User Interface to display and analyze electrophysiology experimental data

2.1 Introduction

The purpose of the first part of this thesis work was dual. On one hand, the development of a Graphical User Interface (GUI) for loading, displaying, analysing and exporting data coming from cellular electrophysiology experiments. The functioning of the GUI was tested by replicating the experimental results of a study regarding mutations of the HCN4 channel, which - as explained in the previous chapter - is responsible for the funny current in the sinoatrial node. On the other hand, the conductance of the mutated HCN4 channels extracted from this analysis was used as a parameter of the single cell model by Fabbri et al. [11]. This was made as a first a step to link the reduced available I_f current shown in the study (channel level) to the bradycardia the patient was affected by (organ level).

The interface was developed for and thanks to Elements Srl - the company where I carried out the internship for this thesis - which will distribute this tool as an open source software. The final name of the tool has not been decided yet, and therefore it could be distributed under another acronym in the next software release. Anyway, this tool will allow researchers to use the interface to perform simple analyses on their data, but also modify it or add code to it in order to implement the functionalities they desire.

2.1.1 Aims

This GUI aims to provide an easy and versatile tool for analysis, which can be easily adapted to the needs of every electrophysiology laboratory. The interface was entirely developed in MATLAB (2019b, Mathworks) using App Designer, a MATLAB tool dedicated to the creation of GUIs. Only the Home license was used to develop the GUI, so its use does not need any additional toolbox.

The Elements Read GUI owns several functionalities, namely:

- Loading .abf (later described in section 2.2.1) or .mat format files;
- Visualization of basic data information (file name, sampling frequency, number of samples, number of sweeps);
- Cursors handling to extract portions of signal to be analyzed;
- Data Analysis: I/V and G/V graphs, histograms, power spectral densities (Welch's method [29]);
- Fittings (linear, exponential, Gaussian, Boltzmann's curve) of both raw data and data coming from analyses;
- Exporting of original data, analyses and fittings in a .mat file.

  In this work only some of these functionalities will be presented, namely the ones that have been used to extract the parameters necessary for this thesis: I/V graphs, fitting with a Boltzmannn's curve, plot of parameters (τ [ms] in this case) againts others (V [mV])

2.2 GUI Implementation

2.2.1 ABF format

(adapted from Unofficial Guide to the ABF File Format [30])

The ABF, which stands for Axon Binary Format, is a file format very common in cellular electrophysiology, used by the largely diffused Axon Instruments devices. Since it is coded in a proprietary code, to access the data produced by these instruments the knowledge of the internal structure of the file is needed. This was known for the first ABF distributed format, but the situation changed with the release of the new ABF2 format, which was distributed without documentation, if not for a general user guide [31] from which Figure 2.1 was extracted.

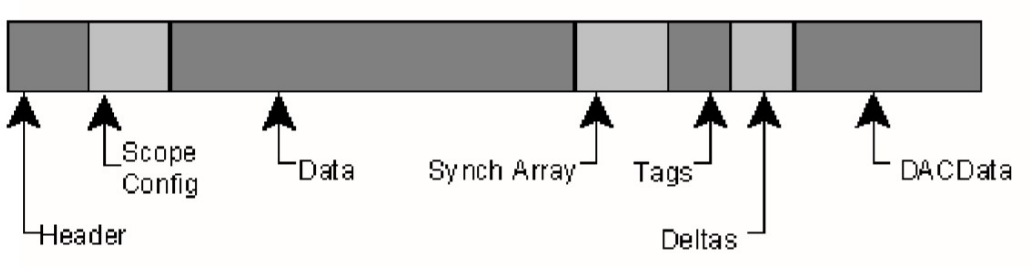

Figure 2.1: Internal structure of ABF format [31]

Despite this lack, some programmers managed to extract the fundamental information from the file, and the results are open source software that load data and their information in many languages: Matlab, Python, ecc. As can be seen in Figure 2.1, and as reported in the *Unofficial guide to the ABF file format* [30] indeed, ABF files are composed by several sections, where the most important ones are Header and Data. The first one contains the information about the positions of the other sections, and it is therefore necessary to find the desired information, whereas the latter contains the true experimental data. Another useful section is Sync Array, containing information about the used experimental protocols (e.g.: number of sweeps, that is the number of acquired episodes such as the onset of an action potential). Every section is divided in blocks of 512 bytes, indicized by a block number: to extract data it is therefore necessary to know the starting position of the section, how much space one data takes (e.g.: a 16 bit integer takes 2 bytes), and how much data are present (i.e. how many bytes must be read). The problem with ABF2 is that the Header does not have a fixed dimension, so the positions of the sections are not known a priori; it is this fact that does not allow the direct access to the data. Nevertheless, the information on the position of the blocks is always stored in the same position of the Header, so, knowing this, it is possible to move to the position of the desired block. The work of the above mentioned programmers, was consequently that of deduce in which position of the Header the pointer to every section was; for example the information on the Data section are found in the 236th byte of the Header. In this byte (and in the next one), the position in which the section starts, the dimension of the data and how much data are present are saved, namely the three information needed to extract experimental data.

In order to load ABF files with this interface, the MATLAB script abfload.m (available open source [32], and which implements all this operations), was used.

2.2.2 ABF file acquisition modalities

(adapted from Axon^{TM} Binary File Format (ABF) User Guide [31])

Inside ABF files it is possible to find data acquired in many ways, depending on the type of studied signal. These modes are:

- **Gap-Free Mode**: the file contains a unique sweep acquired with a uniform sampling interval; no stimulus waveform is associated to the signal. This modality is usually employed for continuous acquisitions of data where it is present a uniform activation in time;
- **Event-Driven Mode**: the acquisition starts after a specific triggering event, such as the exceeding of a threshold. In this case also, there is no stimulus waveform associated to the data. The variable-length mode is usually used to acquire data with peaks of activity separated by long quiescent periods, of unknown duration. If the activity has always the same duration, the Fixed-length mode is preferable, since it is possible to divide the acquisition in different sweeps (that is, episodes of the same length that could be compared with each other);
- **High-Speed Oscilloscope Mode**: similar to Event-Driven Fixed-Length mode, with the difference that in this case the exceeding of a threshold does not necessarily trigger an acquisition, so that it is possible for the analog-to-digital converter (ADC) to operate at its maximum sampling frequency;

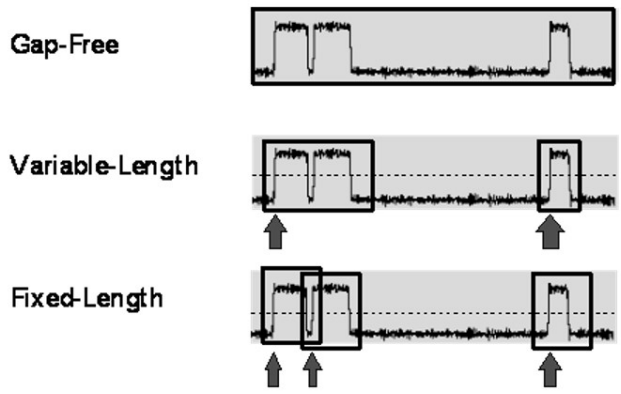

Figure 2.2: Examples of data acquisition modes in ABF files [31]

- **Episodic Stimulation Mode**: in this mode, a certain number of sweeps of different length is acquired, forming a so-called “run”. If more “runs” are acquired, the values of the correspondent sweeps are averaged between

them, so that a "trial" is created and saved in the file. Only one "trial" can be stored inside an ABF file. The digital-to-analog converter (DAC) can generate one waveform for every sweep. This waveform can be composed by up to 10 "epochs", in turn made up by signals such as steps, ramps and digital pulses. The length of these signals can be automatically increased from one sweep to another. It is also possible to use two different sampling frequencies: the "Fast" one, which is the DAC's real one, and the "Slow" one, which is obtained through decimation of the signals, and employed to reduce the number of samples stored in the file.

2.2.3 Graphic interface functionalities

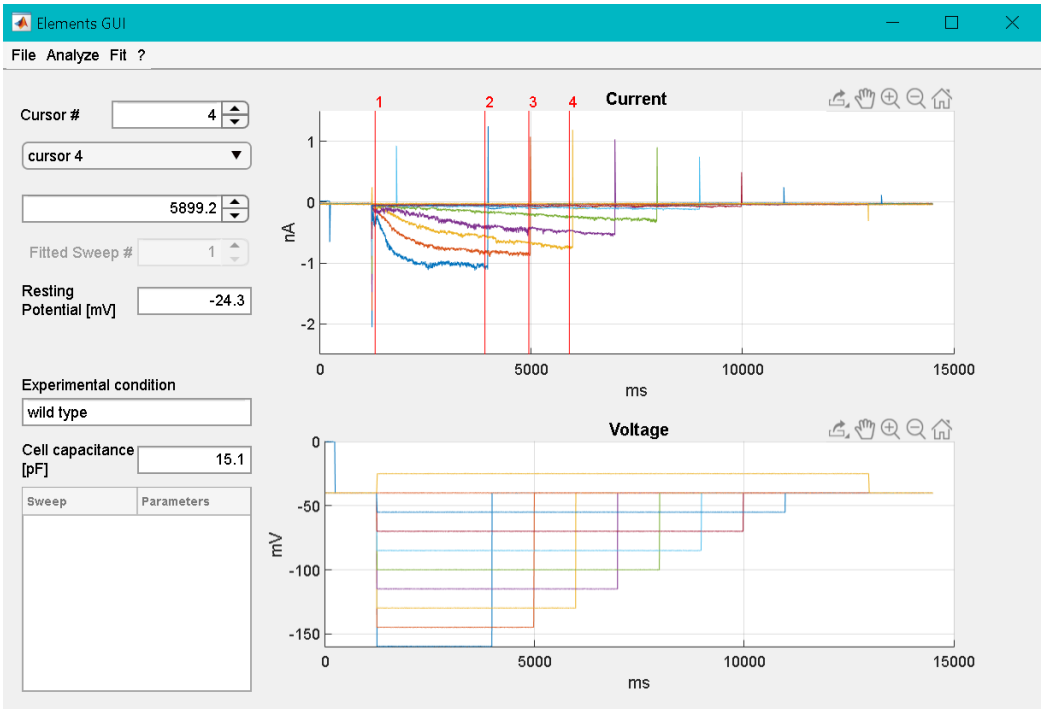

Figure 2.3: Appearance of Elements Read GUI graphical interface: in the upper graph, current data are showed, whereas in the bottom graph one can find the voltage steps of the protocol adopted. Cursor handling is on the high left. Always on the left, other information can be inserted, such as the Resting Potential and the Capacitance of the cell and the Experimental condition in which the data were obtained, in order to name the file to be exported.

The GUI allows one to load files through the drop down menu (Figure 2.3); this operation brings to the visualization of current data (top graph) and voltage

data (bottom graph). Every sweep is plotted in a different colour. It is possible to select up to 10 cursors, in order to define the portion of signal to analyse or fit. The cursors can be selected and located with the related fields in the top left, or by dragging them with the mouse. Further fields present in the interface allow to specify the experimental condition (in order to label the data to be exported) and to insert the values of the resting potential and of the capacitance of the cell. The first of these values can be used to calculate the conductance $g = I/(V - Ek)$ of the cell. This is anyway a risky operation if the resting potential of the cell is in the range of the voltage steps applied in the experimental protocol, since $V - E_k$ will be close to 0 and therefore the computed conductance will approach infinity. The capacitance of the cell can be instead used to normalize current data, in order to obtain a current density measure. Indeed, bigger cells tend to have more channels, thus they express higher currents. By normalizing with respect to this parameter, it is therefore possible to obtain a measure of the current flowing through a single channel.

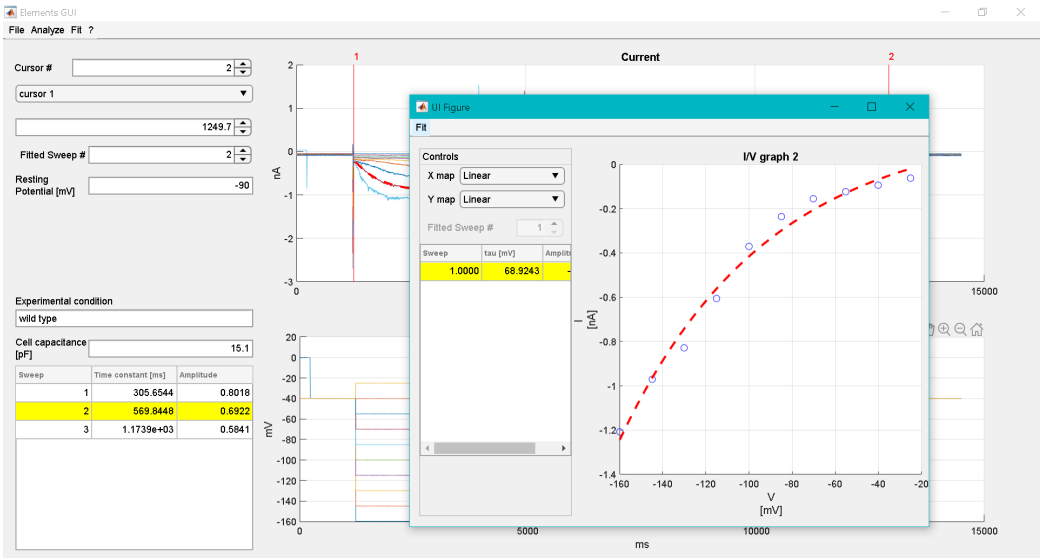

Figure 2.4: Example of analysis and fitting performed through the GUI: exponential fitting of an I/V graph, with fitting parameters highlighted on the left (window in the foreground).

About the analyses, it is possible to perform I/V graphs, G/V graphs (activation graphs), histograms, power spectral densities or to plot fitting parameters one against the other (e.g.: time constant of the current curve, obtained through an exponential fitting, against voltage). In Figure 2.4, an example of the I/V relationship obtained from data showed in Figure 2.3 is depicted. Note how the analysis is showed in a new window, which first of all presents the possibility to execute fittings on the analysis itself (in this case an exponential fitting was performed), but

also to change the axes mapping from linear to quadratic, logarithmic or square root. This can be useful if the data have a particular trend (e.g.: an exponential curve will appear as a straight line if y axis mapping is set to logarithmic).

Fittings can be performed on raw current data as well, in both cases the fitting parameters are showed in a table on the left, with the values of the selected curve highlighted. Finally, the GUI allows one to export raw data, analyses data and fitting parameters in a .mat file, so that one can perform more complex analyses directly in MATLAB.

2.3 Results

2.3.1 Current Features Extraction with Elements Read GUI

The purpose of the first part of this thesis work is to develop the graphical interface Elements Read GUI. Then, once this tool was available, it has been used to replicate the experimental results of Servatius, Porro et al. [10] in order to obtain parameters with which to feed a single cell computational model of the human sinoatrial node. This was made to assess the effects of the mention double mutation not only on the HCN4 channel, but on the SAN cell as a more complex system. In the study by Servatius, Porro et al. [10] indeed, the case of a patient affected by two different mutations of HCN4 channel was presented. This channel is well known for having a primary role in the self-excitation of specialized cardiomyocytes and neurons. Because of these mutations, the patient showed mood disorders, anxiety, ventricular fibrillation and sick sinus syndrome associated with a deep bradycardia. For the authors of this study, these symptoms were due to the fact that the mutations produce a partial loss of function of the funny current. This is because the mutations reduce the number of available channels, more than to altered current properties.

This can be assessed in Figure 2.5, where the results of the electrophysiological measures in several experimental conditions are shown:

- **WT (1 μg)**: wild type (healthy) condition: all of the expressed channels are functioning. 1 μg is the plasmid quantity used to transfect the HEK 293 cells [10];

- **WT (0.5 μg)**: only functioning channels are present, but in half the quantity of the WT (1 μg) condition;

- **WT (0.5 μg) + I479V/A485E (0.5 μg)**: half of the expressed channels are healthy, half are mutated (heterozygous condition);

– **I479V/A485E (1 μg)**: all of the expressed channels are mutated (homozygous condition).

The kinetics of the mutated current and of the non-mutated one are basically the same (Figure 2.5: D, activation graph; E, activation time constant). What changes is the entity of the current (Figure 2.5: C, I/V relationship), which in the case of heterozygous mutation (WT (0.5 μg) + I479V/A485E) is the half of the WT condition, but equal to the current produced by WT (0.5 μg) cells (Figure 2.5: A and B). This means that the mutated channels do not express an appreciable current.

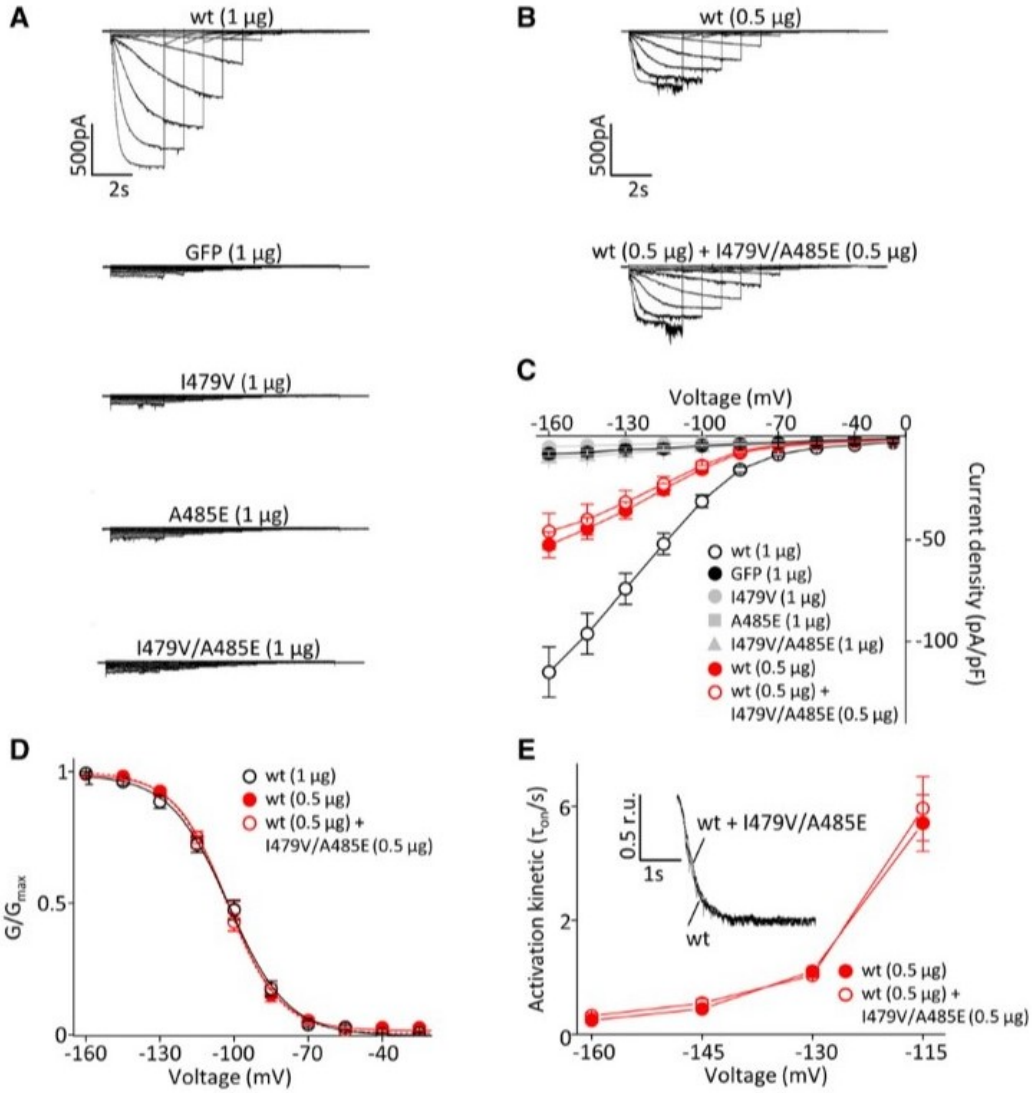

Figure 2.5: Results of the study of Servatius, Porro et al. [10]. A) Current data in the different experimental conditions; B) Comparison between the current data of the WT 0.5 µg condition and the WT 0.5 µg + DM one. C) I/V curves for the different experimental conditions. D) Activation curves for the wild type, half expressed wild type and WT 0.5 µg + DM conditions. E) Comparison between the activation time costants of WT 0.5 µg and WT 0.5 µg + DM.

The same graphs (mean +/- SEM) were obtained thanks to the GUI (Figure 2.6). Also, parameters of the mean Boltzmann curves were obtained, to perform a validation against the values reported in the study (Table 2.1).

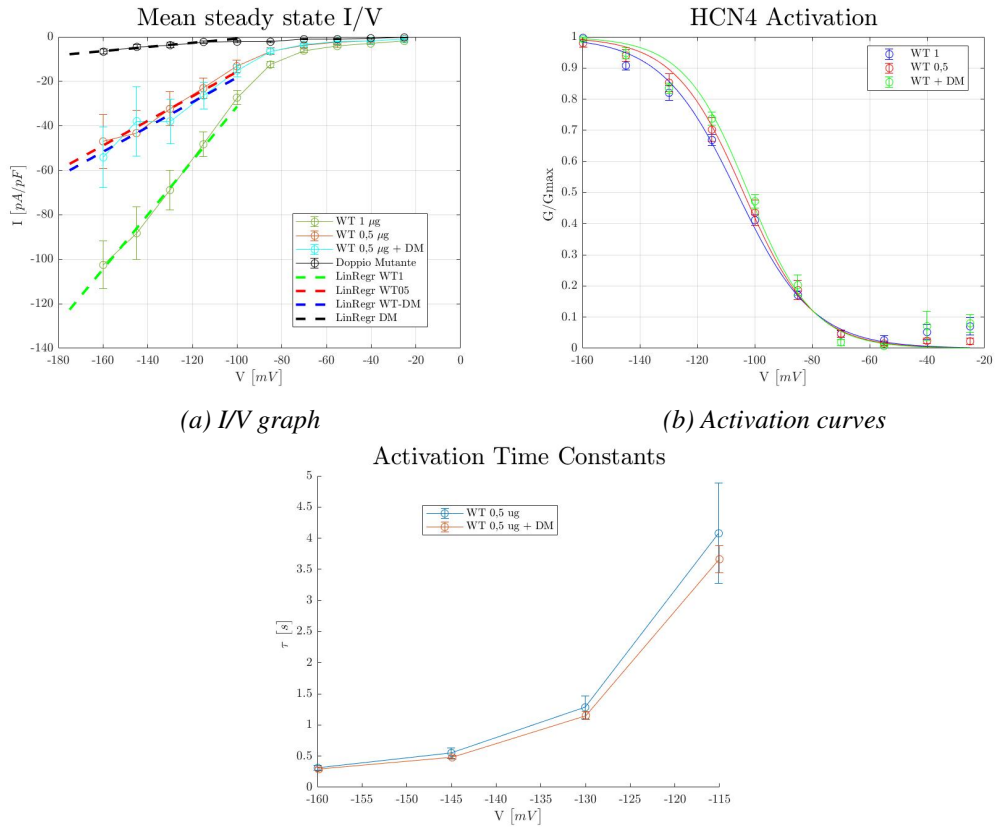

(a) I/V graph

(b) Activation curves

(c) Time constants

Figure 2.6: Replication of the results of the study of Servatius, Porro et al. [10] using the GUI: a) I/V graphs for the 4 experimental conditions and relative linear regressions on the 4 most negative potentials: -160, -145, -130 and -115 mV; b) Activation curves of the 4 experimental conditions except for I479V/A485E, which does not express any current; c) Time constants of WT 0.5 μg and WT 0.5 μg + DM.

In Table 2.1, the V_{50} and *Slope factor* values for human SAN cells, as measured by Verkerk et al. [33], are also reported. The differences between these values, the ones obtained with the tool developed during this work and the ones reported by Servatius et al., highlight two aspects. First, different experimental conditions and protocols (ionic solutions, absence of cAMP, amplitude and duration of voltage steps) were used. Second, and most importantly, there is difference between an heterologous system (e.g.: HEK-293 cells) and a real human cell, because the latter presents many mechanisms that are not found in HEK cells (an example

	WT 1 μg	**WT 0.5 μg**	**WT 0.5 μg + DM**	**Human SAN cell**
V_{50} $[mV]$	-106.2 $\pm$ 0.9	-103.9 $\pm$ 2.4	-102.2 $\pm$ 0.8	-96.9 $\pm$ 2.7
	-103.1 $\pm$ 0.2	-102.1 $\pm$ 0.8	-102.6 $\pm$ 0.9	
$Slope$ $[mV^{-1}]$	-13.3 $\pm$ 1.1	-12.1 $\pm$0.8	-11.3 $\pm$ 0.7	-8.8 $\pm$ 0.5
	-11 $\pm$ 0.2	-10.7 $\pm$ 0.7	-12 $\pm$ 0.8	

Table 2.1: Comparison between Boltzmann's fitting parameters extracted with the GUI from HCN4 activation curves (black) and the same parameters as reported by Servatius, Porro et al. [10] (grey). In light blue the same features for a human SAN cells, as reported by Verkerk et al. [33], are presented.

could be the already mentioned cAMP), but have a real effect during patch-clamp experiments. Human cells also express other HCN isoforms and for this reason real I_f channels can have properties different from channels only formed by the HCN4 isoform. Moreover, to delete the effect of all types of channels that are expressed in a human SAN cell, except the I_f ones, the curves for human cells are obtained as follows: first, a patch clamp recording of the whole cell is made (thus considering every channel); second, Cs^+ - which as said in Section 1.3, is able to block HCN channels - is added and a new recording is performed; finally, the difference between the two acquisition is computed, and this difference is meant to provide the effect of I_f alone. These operations can clearly involve errors that contribute to explain the difference between the reported parameters.

2.3.2 Effects of I479V and A485E mutations at the single cell level

After evaluating the effect that the mutations induces to the I_f current, the next step was that to link the genotype, that is the mutation, to the phenotype, namely the symptoms expressed by the patient (the bradycardia in particular). It is indeed known from literature that a knock-out of the funny current, even if partial, leads to a slowdown of the cardiac frequency [34]. Having indeed less current available, more time is needed for the triggering of the action potential and therefore the frequency is reduced.

To assess the correspondence between the mutations and the bradycardia, a computational model of a human sinoatrial node cell (Fabbri [11]) was used: action potentials of this cell were simulated varying the HCN4 channel maximum conductance. As already mentioned, HCN4 is responsible of the self-pacing current of the myocardium, the funny current. The maximum conductance expresses indeed a measure of the number of available channels, which is strongly reduced under a mutated condition, according to the above reported experimental data.

This parameter was obtained as the slope of the straight lines given by the linear regressions of the last 4 points of the I/V graph (-160, -145, -130 and -115 mV, Figure 2.6), normalized with respect to the cell capacitance. Since the cell capacitance values were unfortunately missing, they were estimated for every cell as the ratio between the charge Q absorbed by the cell during a voltage step stimulation ΔV, and the voltage step itself. The charge Q was the sum of two contribution: I) the integral of the current with respect to the steady-state value after the voltage step, obtained by numerical integration and II) the integral of the current that flows through the membrane resistance with respect to the steady-state value. This second term was computed as the product between the current step at steady-state (difference in current before and after the stimulation) and the time constant of the response to the stimulus, obtained through an exponential fitting.

Maximum conductances were obtained as the slope of linear regression of I/V graphs since at low potentials, where there is a high probability that all of HCN4 channels are opened, the relationship between current and voltage of the Hodgkin-Huxley model $I_f = Gf_{max} \cdot n_\infty \cdot (V - E_{inv})$ becomes a simple linear relationship (Ohm's law: $I_f = Gf_{max} \cdot (V - E_{inv})$), because n_∞, the gating variable, is equal to 1. Given however that in the study the experiments were executed on HEK-293 cells (in order to over-express HCN4 channels), it is not possible to use the absolute value of the maximum conductance of the cell, but it is necessary to use a relative measure. The values obtained were therefore normalized with respect to the maximum conductance of the wild type condition (in which the conductance and therefore the current is maximum), thus getting a percentage measure of the decrease of the conductance of the funny current with respect to the healthy condition.

Table 2.2 shows the conductance values used in the single cells simulations, obtained by scaling the WT 1 μg value respectively of the 45 %, 46 %, 33 %, 8 % and 2.6 %, which represent the residual activations obtained in the different experimental conditions. In Table 2.2 the results of the simulations are also shown.

	WT 1 μg	**WT 0.5 μg**	**WT 0.5 μg + DM**	**WT 1 μg + Amio**	**DM**	**DM + Amio**
$\mathbf{Gf_{max}/Gf_{max}(WT1)}$	100 %	45 %	46 %	33 %	8 %	2.6 %
$\mathbf{g_f}$ $[\mu S]$	0.00427	0.00192	0.00196	0.00141	0.000342	0.00011
CL $[ms]$	814	907	890	946	1019	1030
HR $[bpm]$	73.7	66.2	67.4	63.4	58.9	58.3
ΔHR	-	+10.2 %	+8.6 %	+14 %	+20.1 %	+20.9 %

Table 2.2: Percentage values of maximum I_f conductance with respect to the wild type condition ($Gf_{max}/Gf_{max}(WT1)$) and correspondent absolute g_f values; Duration of the action potential (CL, Cycle Length, in ms); Heart rate (HR, in beats per minute) and HR percentage variation.

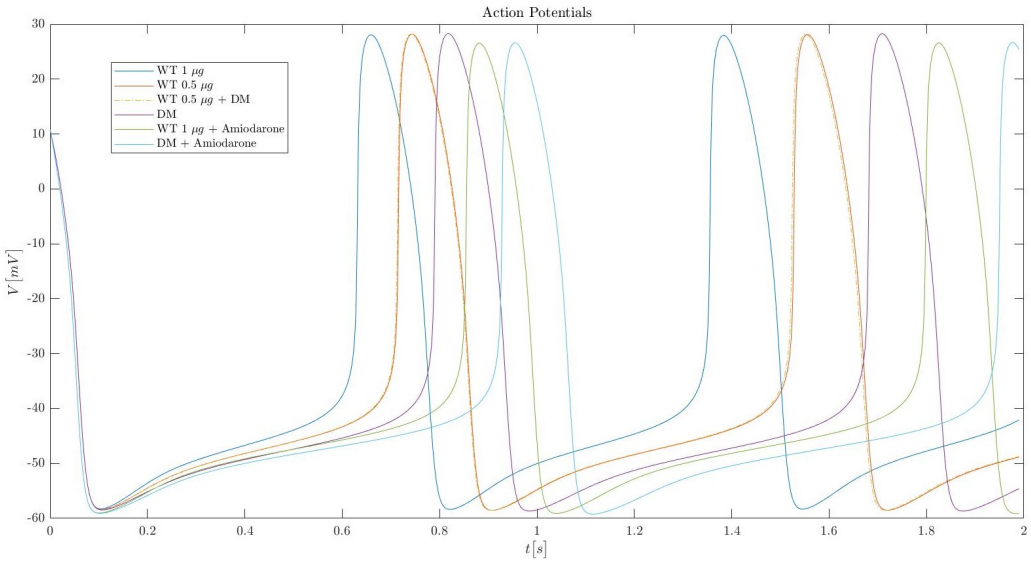

Figure 2.7: Comparison between the APs of the cells in the different experimental conditions: both the double mutation and the Amiodarone contribute to slow down the beating frequency. Their combined effect provides the longest CL: 1030 ms.

As it can be seen from the results reported in Table 2.2, at the decrease of the maximum conductance, the duration of the cycle length (CL) increases from 814 ms of the WT condition to 1019 ms of the case in which only mutated channels are expressed in the cell (DM condition). This is also visually assessable in Figure 2.7. Consequently, the heart rate drops from about 74 bpm of the healthy condition, to the 59 of the pathological one. The simulation gives therefore a confirmation, regarding the bradycardia, of the study by Servatius, Porro et al. [10], for which this symptom is due to the reduced current expressed by the cells affected by the double mutation under investigation.

As reported in the study, the patient was also treated with an anti-arrhythmic drug, the amiodarone, which it is known to have a bradycardic effect. This was tested by reducing the conductances for I_{kr}, I_{to}, I_{NaL}, I_{Na} and the permeability of late calcium current P_{CaL} respectively of the 2.9 %, 6.0 %, 5.1 %, 0.3 % and 2.4 % (Table 2.3).

	$\mathbf{I_{Kr}}$	$\mathbf{I_{to}}$	$\mathbf{I_{NaL}}$	$\mathbf{I_{Na}}$	$\mathbf{P_{CaL}}$	$\mathbf{I_f}$
Reduction [%]	2.9 %	6.0 %	5.1 %	0.3 %	2.4 %	66 %

Table 2.3: Effects of Amiodarone on the conductances and permeabilities of a SAN cell at a concentration of 3 · Free Cmax ([35], [36]).

This is indeed the effect the amiodarone has on these currents at a concentra-

tion of 2.1 μM, which was considered to be 3 times the maximum concentration achievable by the drug after its administration (Free Cmax). This data was extracted from the study of Crumb et al. [35]. This study did not report data about HCN4 channel and I_f current, so the values presented in the work by Tamura et al. [36] were considered. This study reported an IC_{50} of 2.1 ± 1.9 and a Hill coefficient $h = 0.9 \pm 0.2$. Using the Hill equation,

$$Activation(\%) = \frac{1}{1 + (IC_{50} + 3 \cdot FreeCmax)^h}$$

and considering the worst case ($IC_{50} = 2.1 + 1.9$ and $h = 0.9 + 0.2$), a percentage activation of 33% was obtained for the HCN4 channel. This means that I_f is reduced of 2/3.

Considering the consequences of amiodarone only, the AP duration of the single cell model changes from 814 ms to 946 ms (HR = 63.4 bpm). Combining the effects of both mutations and amiodarone instead, a total activation of 2.6% is achieved, bringing the CL to 1030 ms and the HR to 58.3 bpm. For this human SAN cell model, the onset of an AP is guaranteed even in the case of complete block of the funny current ($g_f = 0$), opposite to what happens in the model of a rabbit sinoatrial node cell [11], from which the human one was derived. This proves the robustness of the mechanisms at the base of the functioning of the human heart, although a relevant decrease in the heart rate is still present.

Regarding the replication of the experimental results of the study by Servatius, Porro et al. [10], some clarification is necessary. First of all, cell capacitance values, used to normalize the current in I/V graphs (Figure 2.6), were not available. The normalization is a necessary operation since it allows to obtain a measure of the current independently from the dimensions of the cell: in fact, the bigger the cell is, the more channels it owns and therefore the more current it expresses. The capacitance of the cell provides a measure of its size and consequently of the number of channels; normalizing with respect to it means to obtain a measure of current density, specific of a single channel. The estimation of the capacitance was performed as already described in section 2.3; here, we point out that all the estimation process can have introduced some errors, that can explain the bigger variability shown by the replicated graphs with respect to the original ones. This is anyway a qualitative observation, since the state of the art of the experimental acquisitions does not reckon on automated methods of feature extraction (e.g.: steady-state value of the current signal) as the developed tool does. The measure is entrusted to the researcher, with consequent intra- and inter- operator variability, which makes the comparison unreliable.

Another critical issue, observable in the conductance graph of Figure 2.6b, is given by the fact that at high potentials, the current seems not to inactivate

completely, in contrast with what it should happen. This is because the extraction of the absolute maximum value of the tail currents is a sensitive operation, that can introduce a high variability depending on the algorithm used and on the signal preprocessing.

The experimental protocol used in the study, namely voltage steps with variable durations (just enough to get to a steady-state value, so as not to stress the cells) is very specific and uncommon. Furthermore, considering that such results were not used to obtain simulation parameters, it was chosen not to implement a solution to this issue. The implementation of a more robust algorithm went indeed beyond the aims that this GUI proposes to satisfy, so it was not undertaken. This way, on one hand a future development of this tool remains possible, and on the other hand the user is free to implement specific methods for other protocols.

Part II

Chapter 3

Materials and Methods

The aim of the second part of this thesis work was the development of a 1D and a 2D models of the human sinoatrial node, and the assessment of the effect of the mutations reported by Servatius, Porro et al. [10] on the models themselves. About this, the main question was if the bradycardic effect seen on the single cell model is of the same entity on more complex systems (i.e. at fiber and tissue levels). This chapater will therefore explain how these models were designed and implemented.

3.1 Hardware and software

All the simulations were executed on a workstation running with a 16-core AMD Ryzen Threadripper 2950x, an NVIDIA Titan V GPU and 64 GB RAM. The models were entirely developed using Mathwork's MATLAB, version 2019b. For the 1D model, 100 cells were considered; given an approximate length of 50 μm for a human central SAN cell, this mimicked the behaviour of a 5 mm fiber. In the 2D model, a matrix of 50x50 cells was implemented, simulating a 2.5x2.5 mm tissue. A total of 2500 elements - obtained dividing the dimensions of the SAN by the dimensions of a single cell - is a good esteem of the magnitude of the cells composing the rabbit SAN [40]. This qualitative computations surely underestimates the number of cells in the human SAN, but can be a realistic start. However, considering them as symmetric and all of the same size is surely an approximation.

The length of the simulations was 20 s, a time span that allows the cells to get to a steady-state condition. For the 1D model, this took about 300 s, whereas the 2D model needed around 1100 s to be solved.

3.2 Connecting the single cell models implementing gap junctions

The 1D and 2D computational models were first obtained in MATLAB as a multi-dimensional union of human SAN single cell models from Fabbri [11]. This was achieved by connecting the models with an equation representing the inter-cellular linking due to gap junctions. In fact, if two neighbouring cells are at different potentials, there will be a current flowing from the cell at higher potential to the one at lower potential. Depending on the resistance offered by the gap junctions, this coupling can be more or less strong: in an extreme situation ($R \to \infty$) the cells are totally uncoupled and beat at their intrinsic frequency.
In the 1D model, the gap junction current is obtained as the sum of the differences in voltage between one cell and the cells right before and after this cell, divided by the resistance of the gap junction. First the voltage difference was calculated:

$$V_{net} = V_m(2:end,end) - 2 \cdot V_m + V_m(1,1:end-1)$$

This reflects a linear relationship between current and voltage (Ohm's law) in the gap junctions, as reported by Hagen et al. [38] and generally accepted.

Similarly this is made in the 2D model, but this time another dimension on which to calculate the difference in voltage must be considered:

$$V_{net} = V_{oriz} + V_{vert}$$

where V_{oriz} is:

$$V_{oriz} = Vm(:,[2:end,end]) - 2 \cdot Vm(:,:) + Vm(:,[1,1:end-1])$$

and similarly V_{vert} is:

$$V_{vert} = Vm([2:end,end],:) - 2 \cdot Vm(:,:) + Vm([1,1:end-1],:)$$

To get a current, we divide V_{net} by the resistance of the gap junctions between each cell. In this way the final equation that updates Vm at each time step is achieved:

$$\frac{\delta V_m}{\delta t} = \frac{-i_{tot}}{C_m} + \frac{V_{net}}{R_{gap} \cdot C_m}$$

The i_{tot} term is the sum of all the currents present in the model:

$$i_{tot} = i_f + i_{Kr} + i_{Ks} + i_{to} + i_{NaK} + i_{NaCa} + i_{Na} + i_{CaL} + i_{CaT} + i_{KACh} + i_{Kur}$$

whereas C_m is the capacitance of the cell, equal to 57 pF. Either in 1D and 2D, no-flux boundary conditions were considered.

For both models a main script was designed to:

1. Set the simulation parameters (e.g.: number of cells, duration of the simulation, integration step, gap junction resistance and standard deviation for the cell variability. These last two topics will be respectively described in sections 3.5 and 3.6);

2. Set the initial conditions for every cell. These were obtained by randomly sampling 2s of a single cell simulation using MATLAB *datasample* built-in function. The same random seed was fixed for every simulation so that comparisons between simulations with different parameters settings could be made;

3. Set the cellular heterogeneity, as will be discussed in section 3.6;

4. Preallocate the state variables vector on the GPU, through the *gpuArray* MATLAB command;

5. Call the function that solves the ODEs system;

6. Save the workspace variables.

In order to integrate the differential equations of the model, a forward Euler's method with fixed step was implemented. A function containing this algorithm was therefore built and called from the main script (the code for this function in the 2D case can be seen in Figure 3.1).

As shown in Figure 3.1, the states are updated by calling another function, $Model\_2D\_GPU$, which calculates the variation of the state variables for every cell at every time step. This is made by calling the function which implements the single cell model by Fabbri et al. [11] and by computing $I_{gap} = V_{net}/R_{gap}$ as already described at the beginning of this section (Figure 3.2).

For every simulation, a fixed step of 10 μs was used, except for the 2D case with $R \to \infty$ and $\sigma = 0.4$, that required a step of 8 μs to be integrated (both in WT and DM condition). This small integration steps caused the state vector to have dimensions equal to 33x50x50x2 $\cdot 10^6$ ($2.5 \cdot 10^6$, with a time step of 8 μs). 33 is indeed the number of state variables of the single cell model; 50 is

```
function yOut = GPU_2D_Euler(t,h,yOut,yOld,dy,gJ,cV) %#codegen

% Add kernelfun pragma to trigger kernel creation
coder.gpu.kernelfun;

% Update state variables with Euler's method
rep = length(t);
for idx = 1:rep

    % calculating new states
    yNew = yOld + h * Model_2D_GPU(t(idx),yOld,dy,gJ,cV);
    % the update state is the initial condition of the next iteration
    yOld = yNew;
    % save every step in an output vector
    yOut(:,:,:,idx) = yNew;

end
```

Figure 3.1: MATLAB code for Euler's method

```
function dV = Model_2D_GPU(time,V,dV,gJ,constVars) %#codegen

% Add kernelfun pragma to trigger kernel creation
coder.gpu.kernelfun;

% Update state variables for every cell
for i = 1:size(V,2)
    for j = 1:size(V,3)
        dV(:,i,j) = GPU_HumanSAN_Fabbri_Fantini_Wilders_Severi_2017...
            (time,V(:,i,j),constVars(i,j));
    end
end
% Compute difference in Membrane Potential
Voriz = V(15,:,[2:end, end]) - 2 * V(15,:,:) + V(15,:,[1, 1:end-1]);
Vvert = V(15,[2:end, end],:) - 2 * V(15,:,:) + V(15,[1, 1:end-1],:);
Vnet= Voriz + Vvert;

% Add propagation current : dY(15,1) = -i_tot/C + (Vj-Vi)/(Rm*Cm);
dV(15,:,:) = squeeze(dV(15,:,:)) + squeeze(Vnet)./gJ;

end
```

Figure 3.2: MATLAB code for Model_2D_GPU

the number of cells considered both on x and y dimensions and $2 \cdot 10^6$ ($2.5 \cdot 10^6$) is the number of time steps necessary to simulate 20s of activity. The 1D model state vector was 33x100x2 $\cdot 10^6$. Such vectors were too big for the GPU memory (12 GB), so it was necessary to split them in smaller and less memory-consuming

variables. It was chosen to allocate to the GPU vectors with 1000 time step (so 33x50x50x1000 (1250) and 33x100x1000), representing 10 ms of simulation, and to execute repeated calls to the Euler function in Figure 3.1 through a *for* loop in the main script (Figure 3.3).

```
w = waitbar(0,'0%','Name','Solving ODEs');
for idx = 1:rep

    y = GPU_2D_Euler_mex(t,fixedStep,y,yOld,dy,gapJunct,constVars);

    yOld = y(:,:,:,end);
    stateVect(idx,VmIndex,:,:,:) = squeeze(gather(y(VmIndex,:,:,1:underSamp:end)));

    if mod(idx, gpuRes) == 0 || idx == rep
        stateVect(idx,:,:,:,:) = squeeze(gather(y(:,:,:,1:underSamp:end)));
        reset(g)
        y = zeros(stateVectorDim,nCells,mCells,length(t),'gpuArray');
        dy = zeros(size(yOld),'gpuArray');
        yOld = squeeze(gpuArray(stateVect(idx,:,:,:,end)));
    end

    waitbar(idx/rep,w,[sprintf('%3.0f',idx/rep*100),'%'])
end
delete(w)
```

Figure 3.3: MATLAB code for the loop in the main script

As can be seen in Figure 3.3, after the call to the integrating function, the last time step of the updated states is saved in the variable *yOld*, representing the initial condition of the next iteration. After this, the membrane voltage signal hosted in *y*, the state vector, is first undersampled (1 sample every 100 (125) is kept, in order to have a step of 1 ms instead of 10 µs), then transferred from the GPU to the local workspace and finally stored in a variable named *stateVect* of dimensions 2000x33x50x50x10. 10 is the result of the undersampling: at every iteration, of the 1000 (1250) 10 µs-timesteps necessary to simulate 10 ms, only 10 samples are collected (spaced 1 ms one between the other); 2000 is the number of iterations the main loop is executed, in order to obtain 20 s of simulation. A sequence of 2000 repetitions of 10 ms give in fact 20 s. The operation of retrieving data from the GPU is really time-expensive [37]; for this reason, only the voltage signal is transferred to the workspace at every iteration. All this process was necessary since it is not possible to use variables bigger than the GPU memory because they can not be allocated on it. In addition, the converted code (see later in this section) did not automatically free space when the allocated variables were not necessary anymore, and this caused the GPU memory to go on overflow every few iteration. To avoid this, a reset of the GPU memory was done every 10 iterations (variable *gpuRes*), after storing all the undersampled state variables in the *stateVect* array. Later, the *y* and *yOld* vectors, together with the *dy* vector (which will be filled with the variations of the state variables, as returned by the single cell model) are

once again preallocated on the GPU. Since after the reset the simulation restarts from the final condition of the previous iteration, its first step coincides with this previous condition and was subsequently removed.

3.3 The Matlab GPU coder

In order to exploit the high computational speed provided by the GPU, the code was translated to CUDA kernels obtained thanks to MATLAB GPU Coder. This useful tool allows to convert MATLAB functions to computationally efficient CUDA code contained inside a MEX file (MATLAB Executable). MEX files are the MATLAB interface to machine code (in this case the GPU-tailored CUDA, which is discussed in section 3.4).

Of course the GPU Coder has many restrictions, namely not every MATLAB built-in function can be translated to CUDA, but its simplicity and the efficiency that can be achieved without knowing another programming language, make it an easy and valuable instrument. Furthermore, any kind of C, C++ or CUDA kernel written by the user can be included inside a MEX file, making up for the lack of built-in functions that can be directly converted.

In order to use the GPU Coder, some preparation steps are necessary:

1. The CUDA toolkit must be installed ([42]). On MATLAB, it is possible to check if this is true by running the *gpuDevice* command. Other requisites for the use of GPUs on MATLAB, such as the availability of the Parallel computing toolbox, are explained on Mathwork's site ([43]);

2. It is necessary to add the directive *%#codegen*, that enables the error checking specific to code generation, after the function declaration of every function that is wanted to be converted;

3. To convert the functions to CUDA code, the coder.gpu.kernelfun pragma must be added in the body of the function;

4. Preallocate all the output variables at the beginning of the functions.

Steps 2 and 3 can be visualized in Figures 3.1, 3.2 and 3.3, whereas the preallocation step can be appreciated in Figure 3.4.

To sum up, the simulations were obtained by running a script that iteratively calls the Euler's method function, which in turn iteratively calls the function that I) computes the state variable variations by calling the single cell function and II)

```
function dY = GPU_HumanSAN_Fabbri_Fantini_Wilders_Severi_2017(time, Y,S) %#codegen

% Add kernelfun pragma to trigger kernel creation
coder.gpu.kernelfun;

%--------------------------------------------------------------------------
% Computation
%--------------------------------------------------------------------------

dY = zeros(33,1);
```

Figure 3.4: Function declaration for the single cell model function by Fabbri et al. [11]

calculates I_{gap}. So there are 3 functions nested one inside the other. All of them must satisfy steps 2, 3 and 4 of the GPU Coder prerequisites, but only the top level one (in this case the function implementing Euler's method) has to be converted, since the tool automatically translates all the functions called inside the external one.

The process is quite simple: once opened the GPU Coder tool, from the "Apps" drop-down menu, it is possible to select the .m file of the function that is wanted to be converted (Figure 3.5). By clicking on "next", the tool checks if there are any issues inside the code (such as non-preallocated variables); if everything is fine, the user will be asked to define the function input variables. This can be made by hand, declaring the variable size and data type, or automatically, by clicking on "Autodefine Input Types". Anyway, the input variables must exist in the workspace. The result of this operation is shown in Figure 3.6. The next step is a check for run-time issues, for which it is necessary to select "GPU" in the radio button choice (Figure 3.7). The final step allows to actually generate the CUDA code by selecting "MEX" as the Build Type (Figure 3.8). If this process is successful, .cu files containing CUDA kernels are created and stored inside the "codegen" folder in the current path, the MEX file that calls these kernels is generated and a success message is displayed. More information, together with a tutorial, can be found in MATLAB documentation [44].

Now that the MEX file has been built, it is possible to use it as a normal MATLAB function, with its inputs and outputs: an example is shown in Figure 3.3, where *GPU_2D_Euler_mex* is called inside the main loop.

The usage of CUDA kernels enables great computational power: even though the integration of a system of ODEs is a recursive problem, which is not parallelizable, updating the state variables is an operation that can be made independently for every cell. At every time step the variation of the state variables can be computed simultaneously for every cell, and here lies the possibility of parallelization. Simplifying, GPUs allow to speed up the integration of the equations since the calculations are no more executed one after the other, but at the same time on dif-

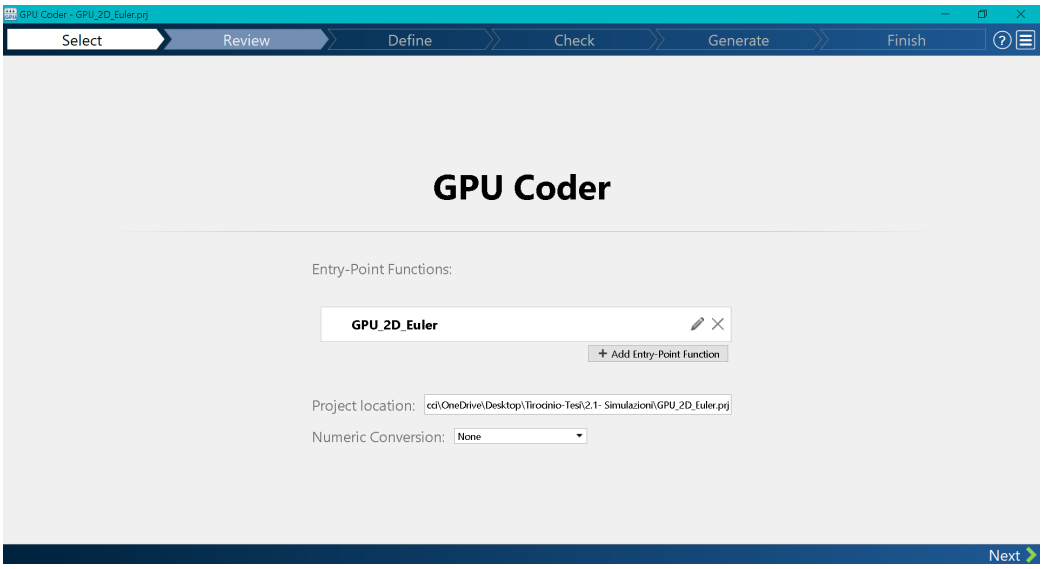

Figure 3.5: Step 1. Function selection

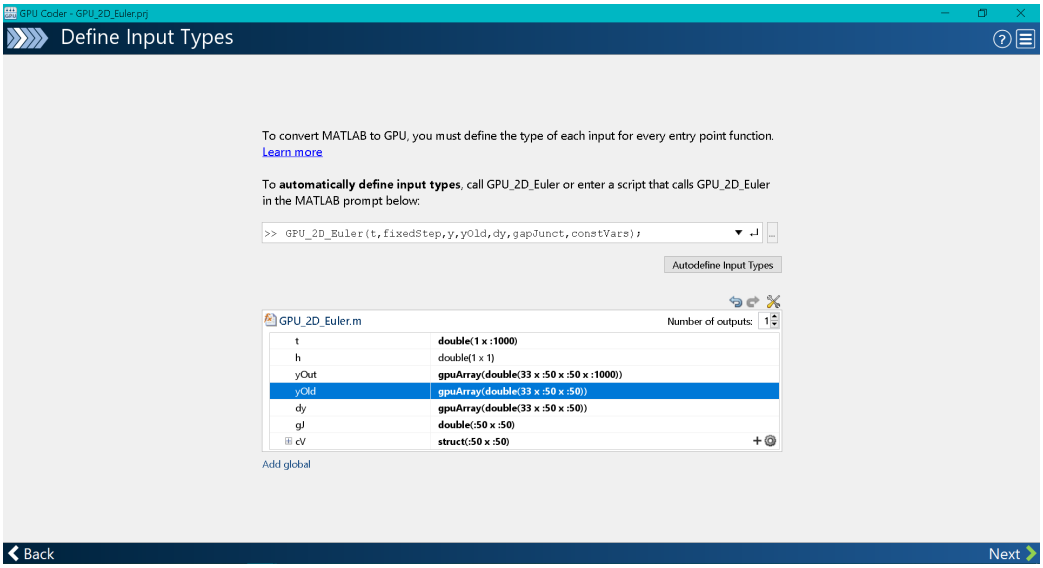

Figure 3.6: Step 2. Input definition

ferent cores.

As already mentioned, the very small integration step caused the state vector to be too big for the GPU, this way forcing to simulate shorter time lapse in sequence. This is critical because the operations of data transfer to and from the GPU, as well as the memory reset, are very slow. Being called many times, they increased

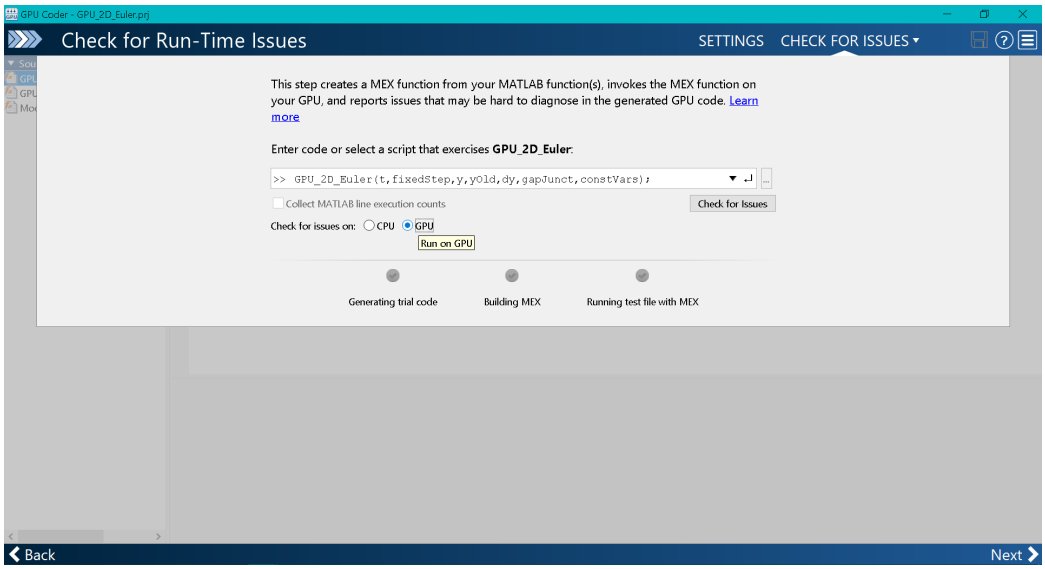

Figure 3.7: Step 3. Run-time errors check

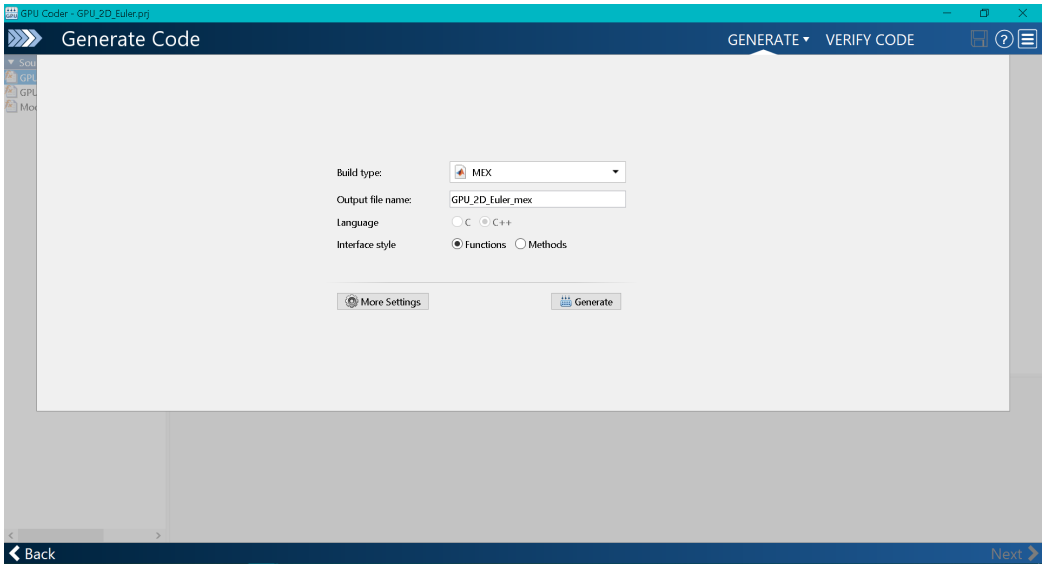

Figure 3.8: Step 4. MEX file generation

the run time of the script, and thus represented the bottleneck of the simulations. Anyway the performance of this solution was much better compared to solving the ODEs without the GPU: a 1D 2 second simulation with 10 cell took 30 s to be solved using the MEX file, but almost 1100 with only the CPU.

3.4 GPU & CUDA

The "Compute Unified Device Architecture" (CUDA), is a general purpose parallel computing platform introduced by NVIDIA in 2006. This platform incorporates the architecture with which the GPUs are organized and the programming language owning specific commands to exploit this architecture. Differently from the CPUs in fact, GPUs are composed of thousands of arithmetic logic units (ALUs), but lack in data caching and flow control (Figure 3.9). This is because a GPU is designed to perform billions of repetitive, low-level tasks: the ratio between arithmetic and memory operations must be very high. This allows to execute the same routine on many data elements at the same time, namely in parallel, this way hiding the memory access latency [46].

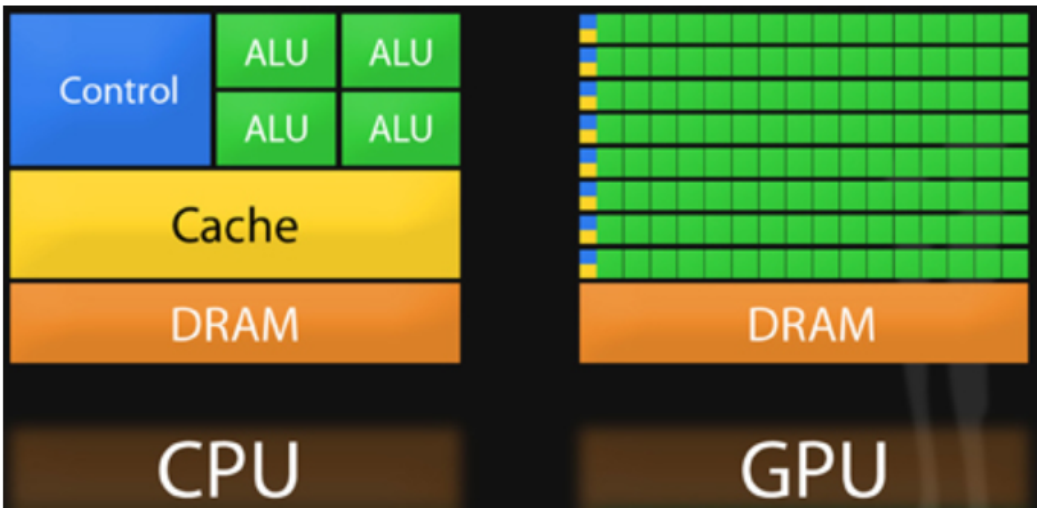

Figure 3.9: Comparison between CPU and GPU architectures [46]

These basic operations are executed by mini-programs known as "kernels", which are constituted by "threads" running simultaneously. More threads are organized in batches called "thread blocks", in a number which is dependent on the available memory and its access latency. Anyway, in this architecture the maximum number of threads per block is 512. More thread blocks, with the same thread dimensions and executing the same kernel, form a "grid" (Figure 3.10, left). This is made in order to perform more than 512 threads in parallel; however, threads of different blocks don not share the same memory and therefore may not be synchronized with one another. Indeed, the GPU memory is organized on three different levels, as shown in Figure 3.10:

- *Global memory*: memory accessible by all the threads and also by the host (CPU), which can allocate and de-allocate it. It is mainly used to initialize

the data handled by the GPU;

- *Shared memory*: memory specific of each thread block. It is accessible by all the threads inside the block and it is therefore much faster than the global one. It exists only for the lifetime of the block;
- *Local memory*: private memory of every thread, assigned for as long as the thread exists.
- *Constant and texture memory*: read-only memories accessible by all threads.

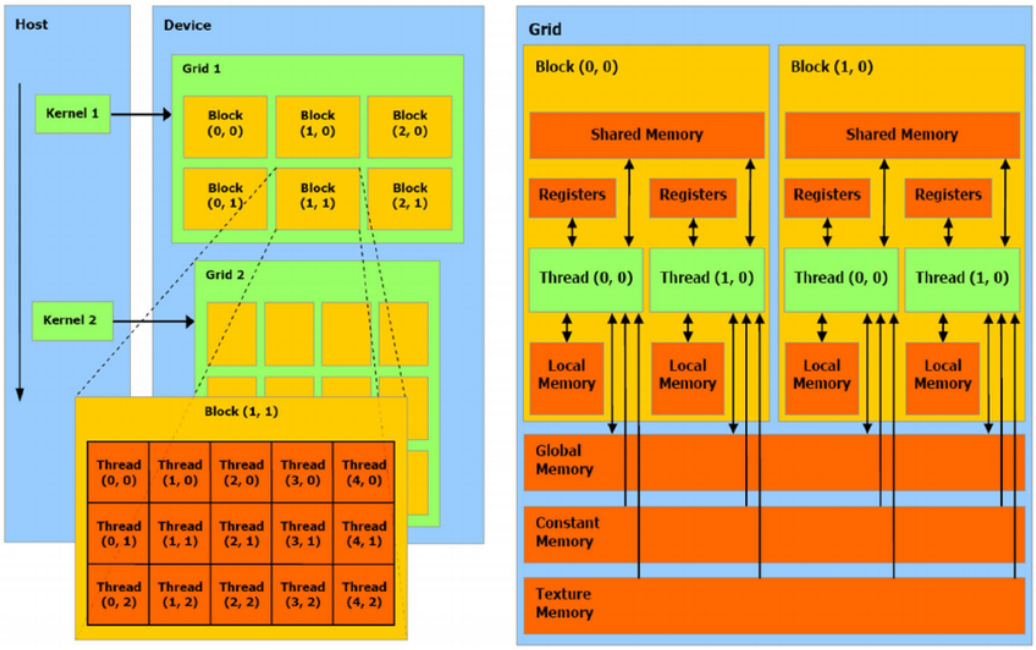

Figure 3.10: CUDA architecture [47]

Furthermore, GPUs work well with 1D, 2D and also 3D vectors (since the thread blocks architecture was designed with this organization [45], Figure 3.10) which are allocated on its memory. To efficiently use GPUs, all the operations on data must be performed when they are stored inside the GPU memory. Data should be transferred back to the local workspace only at the end of these operations [37]. This is because the transfer relies on the PCI bus, which has a high bandwidth in terms of moving data from the host memory to other slots, but much smaller than that of both GPU and CPU (see Figure 3.11). Furthermore, when collecting data from the GPU to the local workspace, MATLAB waits for the completion of every pending operation on the device [48].

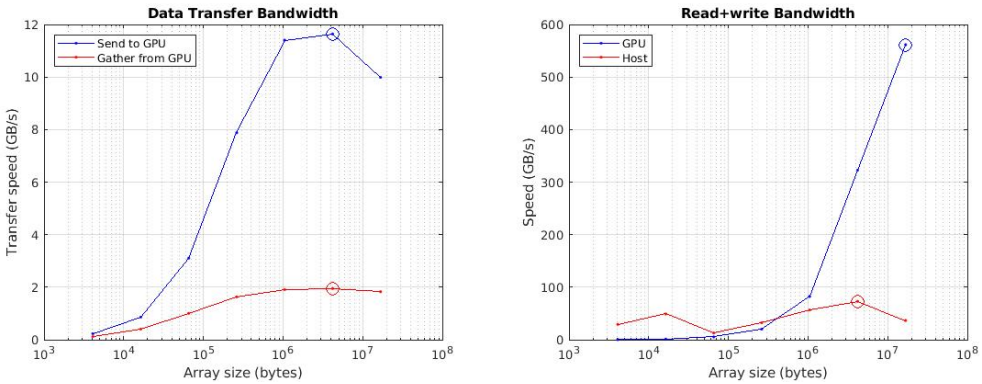

Figure 3.11: Comparison between PCI bus, CPU and GPU performances for the workstation used in this work

This weakens the advantage - in terms of performance - granted by the GPU, so it is a best practice to limit the transfers to and from the GPU device, if possible. Obviously, data transfer rate also depends on the hardware in general (motherboard, CPU, chip set) in addition to the specifics of the GPU.

3.5 Cellular coupling

To study the effect that different gap junction conductances had on the coupling of the cells, and therefore on their synchronization in terms of frequency, several values of resistance were used: 10, 100, 1000, 10000 and $\rightarrow \infty$ M$\Omega \cdot$m. The resistance is expressed relatively to meters (and so as ρ, resistivity) since these models do not consider the dimensions of the cells, only resolving a system of ODEs. The values used are in accordance to the range reported by Inada et al. [14] for rabbit SAN cells, since no data about human SAN cells could be found in the literature. Furthermore, every cell was connected to the other with the same resistance, simulating an homogeneous conduction system. This is far from the physiological condition, but allows to simplify the model and to focus on the effect of other parameters, such as the cellular heterogeneity.

3.6 Cellular heterogeneity

To mimic the physiological variability that can be found inside human tissues, a certain degree of randomness was considered for the main conductances, permeabilities and maximal activities of the cell model by Fabbri et al. [11]. The pa-

Permeability	$[nA/mM]$	**Conductance**	$[\mu S]$	**Current**	$[nA]$
P_{CaL}	0.4578	g_{KACh}	0.00345	I_{NaKmax}	0.08105
P_{CaT}	0.04132	g_{Kr}	0.00424	$_{NaCa}$	3.343
		g_{Ks}	0.00065		
		g_{Kur}	$1.539 \cdot 10^{-4}$		
		g_{Na}	0.0223		
		g_f	0.00427		
		g_{to}	$3.5 \cdot 10^{-3}$		

Table 3.1: Nominal values of the model parameter that have been randomized.

rameters considered were: P_{CaL}, P_{CaT}, g_{KACh}, g_{Kr}, g_{Ks}, g_{Kur}, g_{Na}, g_f, g_{to}, I_{NaKmax}, K_{NaCa}, since these are the key players in the onset of the action potential in the sinoatrial node. The standard deviations considered were: 0.05, 0.1, 0.1873, 0.3 and 0.4. The 0.1873 value was used since it has been reported as a physiological level of heterogeneity in the rabbit SAN [39]. Once again, no data were found for human SAN, so this value was adopted also because a comparison with the results of the thesis work of Jonathan Koussis [40] and Chiara Campana [41] could be made.

Starting from the nominal values in Table 3.1, permeabilities, conductances and maximum currents were randomized using a log-normal distribution, this way avoiding negative values. This distribution was achieved by exponentially transforming the random numbers obtained through MATLAB *randn* built-in function. Multiplication of this factor by the different standard deviation values, provided the desired variability of cellular parameters. The same random generator seed was used among different simulations in order to investigate the effects of coupling and heterogeneity. The code used for this calculation is shown below.

$$
\begin{aligned}
&standardConductances = [P_{CaL}, P_{CaT}, g_{KACh}, g_{Kr}, g_{Ks}, \cdots \\
&\quad g_{Kur}, g_{Na}, g_f, g_{to}, i_{NaKmax}, K_{NaCa}]; \\
&scaling = exp(\sigma * randn(1, length(standardConductances))); \\
&heterConductances = standardConductances. * scaling;
\end{aligned}
$$

Obviously, another seed would have provided other results, which anyway would not have been statistically different.

3.7 Features extraction

The main features extracted and analized were the Cycle Length (CL, in ms) and the Action Potential Amplitude (APA, in mV). The first allows to characterize the

	Cycle Length		Action Potential Amplitude	
	1D	**2D**	**1D**	**2D**
X limits	[300, 2700] ms	[500, 6000] ms	[45, 125] mV	[45, 125] mV
Y limits	[0, 100] cells	[0, 2500] cells	[0, 100] cells	[0, 2500] cells
Bin width	100 ms	100 ms	5 mV	5 mV

Table 3.2: Histogram properties used to show extracted features.

response of the cells in terms of frequency, that is Heart Rate (HR, in bpm); the latter gives information about the current available to the cells. This two features - especially CL - were used to make comparisons between the single cells results and the 1D and 2D results. CL is computed as the difference in time between the last two Overshoots (OS) of the AP of every cell, since at the end of the 20 s the cells are supposed to be in steady-state. APA is obtained as the difference between the most positive potential (the OS), and the most negative one (MDP: Maximum Diastolic Potential).

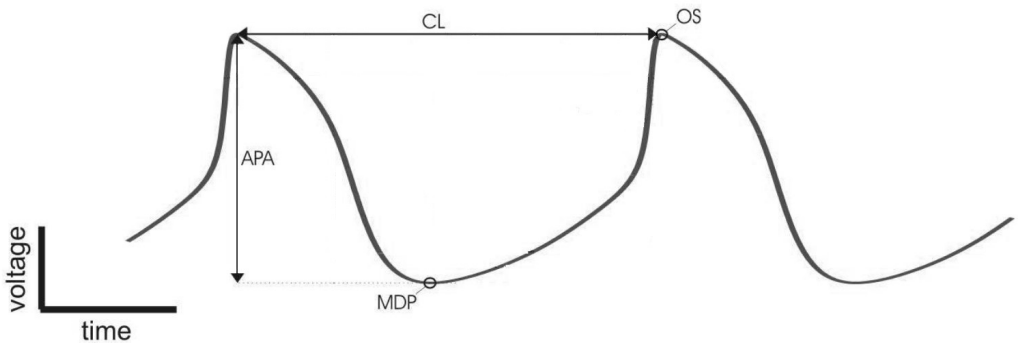

Figure 3.12: Features extracted from the APs. OS, Overshoot: maximum value of the action potential (in mV); MDP, Maximum Diastolic Potential: maximum absolute value of the diastolic phase (in mV); APA, Action Potential Amplitude: difference between maximum and minimum values of the AP (in mV); CL, Cycle Length: time difference between two consecutive OS (in ms).

To show the results, histograms for both CL and APA were made, fixing x and y axes limits and bin width and number, since this allowed to compare WT and DM condition data (Table 3.2). All the x axes in the 2D case have larger limits since the dispersion was bigger with respect to 1D. Both in 1D and 2D some y axes can have instead restricted limits, since in some cases the bins were hardly visible.

The results coming from these parameter settings were then used as a sensitivity analysis to get the values of ρ and σ that provided the most realistic re-

sults in terms of CL, particularly. Another important feature, especially in multi-dimensional models, is the Conduction Velocity (CV, in cm/s), since this feature is not assessable in 0D. CV was computed as the difference in time between the occurrence of the zero-crossing of the AP of the cell that triggered the propagation and that of a cell distant 20 position from it (in the 2D case, x and y velocity were obtained). To get a value in cm/s, the cells were supposed to be 50 µm long (central SAN cell); the space between 20 of them (1 mm) was then divided by the time difference that occurred for the 1^{st} and 20^{th} cell to be at the same voltage (0 mV with a tolerance of 0.5 mV). The 1^{st} cell is the earliest activation point of the last AP occurrence on the 20 s. CV allowed to evaluate another effect of the mutations and the most physiologic value of ρ, since this parameter was set in order to obtain a CV in the range reported in literature (section 1.1).

Therefore, the final part of the results (Chapter 4), will discuss the data coming from the simulations run with the tuned parameters settings.

Chapter 4

Results

In this chapter, the results of the 1D simulations will be presented first, followed by the 2D case. In both sections, the data obtained in the control (WT) condition and then the mutated ones (DM) will be shown; the results at different level of standard deviation - starting from the homogeneous case - are reported in sequence.

4.1 1D Model Analysis

4.1.1 1D Parameter Randomization

In Figure 4.1 it is possible to appreciate the randomized parameters distributions of the single cell human SAN model. The parameters taken into account were: P_{CaL}, P_{CaT}, g_{KACh}, g_{Kr}, g_{Ks}, g_{Kur}, g_{Na}, g_f, g_{to}, i_{NaKmax} and K_{NaCa}, for increasing values of standard deviation $\sigma = 0.05$, 0.1, 0.1873, 0.3, 0.4. Even if in this case the cells were few (100), it can be seen that the distributions have a log-normal trend around the nominal value of the parameters. In addition, the bigger the σ, the wider and more dispersed the distribution.

For the two analysed conditions (WT and DM), all the distributions were the same except the g_f one, which in the DM scenario was scaled by a factor 0.08 with respect to the control condition. Consequently, the nominal value went from $0.004\,27\,\mu S$ to $3.42 \cdot 10^{-4}\,\mu S$. The maximum, mean and minimum values for this conductance are reported in Tables 4.1 and 4.2 respectively for the WT and DM conditions.

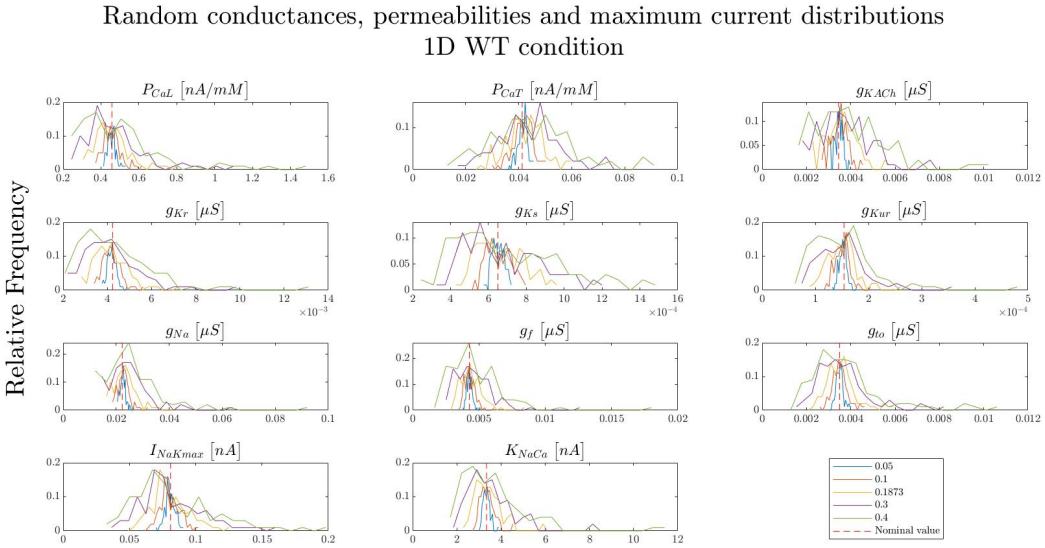

Figure 4.1: Comparison between the distributions of the randomized parameters in the study for the WT condition at different levels of standard deviation. The DM condition has the same distribution of the WT one, except for g_f which is multiplied by a factor 0.08. Exact values for g_f are reported in Tables 4.1 and 4.2 respectively for the WT and DM conditions.

			σ		
g_f	**0.05**	**0.1**	**0.1873**	**0.3**	**0.4**
mean	0.00429	0.00432	0.00439	0.00455	0.00475
min	0.00377	0.00333	0.00268	0.00203	0.00157
max	0.00511	0.00611	0.08346	0.01249	0.01786

Table 4.1: Conductance values for funny current at different values of standard deviation; 1D WT condition (nominal value $g_f = 0.00427\,\mu S$)

			σ		
g_f	**0.05**	**0.1**	**0.1873**	**0.3**	**0.4**
mean	$3.43 \cdot 10^{-4}$	$3.46 \cdot 10^{-4}$	$3.52 \cdot 10^{-4}$	$3.64 \cdot 10^{-4}$	$3.80 \cdot 10^{-4}$
min	$3.02 \cdot 10^{-4}$	$2.66 \cdot 10^{-4}$	$2.14 \cdot 10^{-4}$	$1.62 \cdot 10^{-4}$	$1.26 \cdot 10^{-4}$
max	$4.09 \cdot 10^{-4}$	$4.89 \cdot 10^{-4}$	$6.68 \cdot 10^{-4}$	$9.99 \cdot 10^{-4}$	0.0014

Table 4.2: Conductance values for funny current at different values of standard deviation; 1D DM condition (nominal value $g_f = 3.42 \cdot 10^{-4}\,\mu S$)

4.1.2 1D Wild Type condition

The randomization of the parameters led to the expected cellular heterogeneity: if uncoupled, the cells beat at their own intrinsic frequency, since they do not undergo the influence of the neighbouring cells. Therefore, CL and APA appear distributed around the control value depending on the standard deviation with which the model was fed (Figure 4.2). For CL this value was 814 ms, whereas for APA it was 85.3 mV, namely the values of the single cell model.

The CL distribution has a shape that resembles the log-normal one. However, being the CLs the output of a highly non-linear system, it can not be stated that CL and APA have this kind of distribution (as the APA graph in Figure 4.2 on the right shows). It is only possible to say that the distributions are more dispersed if the heterogeneity is higher (bigger σ) and that the CL one is asymmetric.

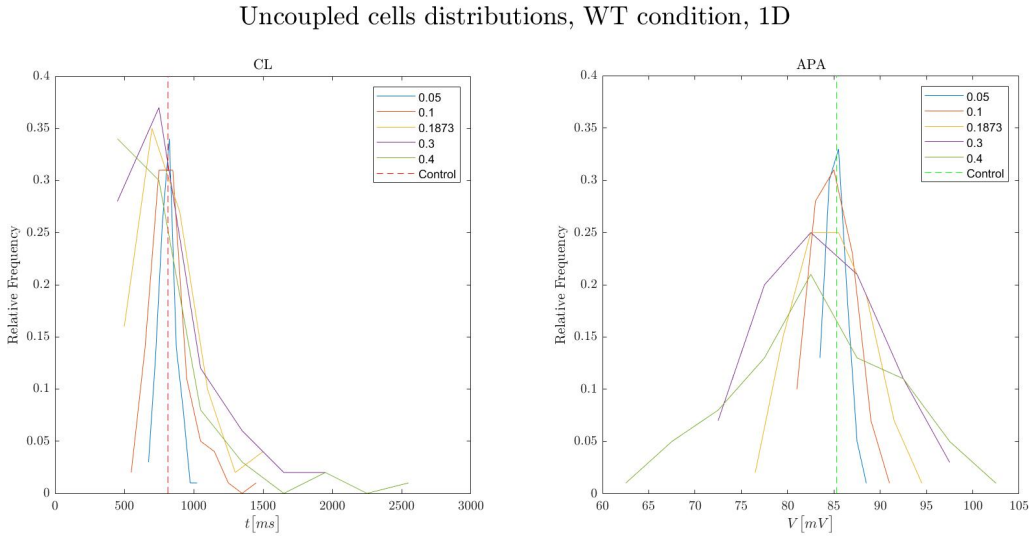

Figure 4.2: CL (left) and APA (right) distributions for uncoupled cells for different values of standard deviation ($\sigma = 0.05, 0.1, 0.1873, 0.3, 0.4$) and nominal values (CL = 814 ms, APA = 85.3 mV, dashed lines); 1D WT condition.

The behaviour is totally different if the cells are coupled with different values of resistance: in general lower resistivity (ρ), which means higher conductance in the gap junctions, allows the cells to synchronize the pacing frequency and phase, whereas a higher ρ prevents the cells from beating together, providing a dispersion in terms of frequency and phase between the cells. For intermediate values of ρ, the synchronization happens in terms of frequency but not of phase. Generally, the bigger is the given σ, the larger is the dispersion, but when ρ is under a certain level, the dispersion is almost zero, since all the cells are synchronized.

Homogeneous cells ($\sigma = 0$)

As can be seen in Figure 4.3, CL is the same for every cell if they are uncoupled. This is expected, as expected is its value, equal to the one of the single cell case (814 ms). Also with $\rho = 10, 100, 1000$ MΩ · m all the cells are coupled and no propagation can be seen between them (814 ± 1 ms, 813 ± 1 ms and 814 ± 1 ms respectively). For $\rho = 10000$ MΩ · m, CLs appear distributed on different values, but this is only for the fact that some of them are less than 800 ms and therefore fall inside another bin. The obtained standard deviation (7 ms) does not justify indeed the presence of two different bins. Anyway, this little dispersion is present even if the cells are homogeneous because they started from different initial conditions. They tried to influence each other without completely succeeding in synchronizing because of the poor coupling.

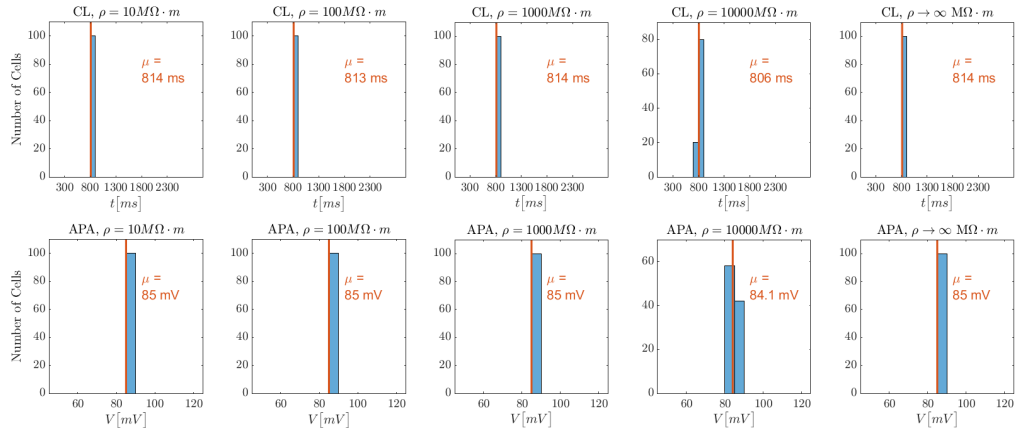

Figure 4.3: Histograms for 1D WT homogeneous condition: CL (top, bin width = 100 ms) and APA (bottom, bin width = 5 mV) at different gap junctions coupling ($\rho = 10, 100, 1000, 10000$ and $\to \infty$ MΩ · m from left to right). Vertical orange lines represent the mean value of the distributions, whose value is displayed on the right.

$\sigma = 0.05$

Introducing a variability in the model parameters provides cells with different behaviour: some have a higher intrinsic pacing frequency with respect to the others. This can be appreciated in Figure 4.4 on the right, where the results for uncoupled cells are shown: in this case indeed, cells do not affect each other and therefore keep on beating at their own frequency; the values of CL are therefore distributed around a mean value of 811 ms. Notably, in all the other cases the cells manage to synchronize, but at higher frequencies: 799 ± 1 ($\rho = 10$ MΩ · m), 783 ± 1 ($\rho =$

100 MΩ · m), 771 ± 11 ($\rho = 1000$ MΩ · m) and 727 ± 14 ($\rho = 10000$ MΩ · m) ms. Uncoupled cells have a CL of 811 ± 65 ms.

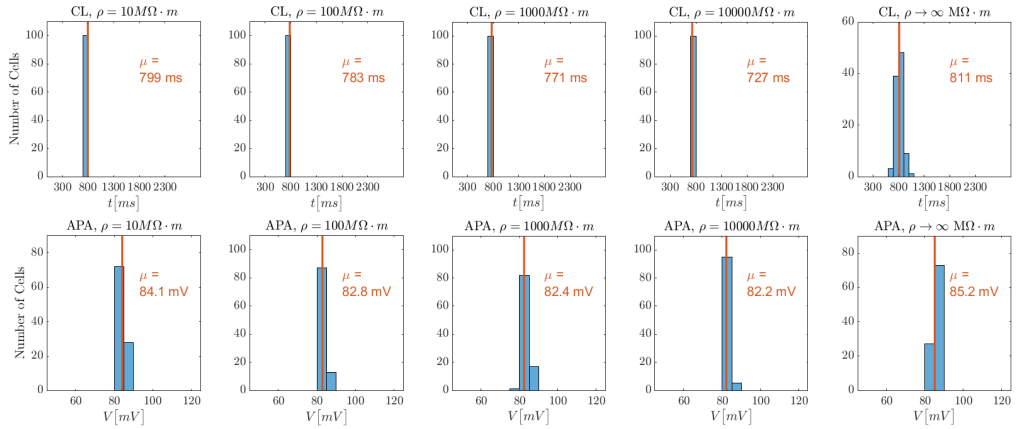

Figure 4.4: Histograms for 1D WT condition with $\sigma = 0.05$: CL (top, bin width = 100 ms) and APA (bottom, bin width = 5 mV) at different gap junctions coupling ($\rho = 10, 100, 1000, 10000$ and $\to \infty$ MΩ · m from left to right). Vertical orange lines represent the mean value of the distributions, whose value is displayed on the right.

$\sigma = 0.1$

In this case, cellular heterogeneity is already too big to allow cells coupled with medium-high resistivities ($\rho = 1000, 10000$ MΩ · m) to completely synchronize (Figure 4.5, CL = 704 ± 27 and 624 ± 31 ms respectively). This happens despite the fact that cells that beat at higher frequencies (with respect to the previous results) are present: CL tends to be shorter, since faster-pacing cells try to drive all the others, but are still too weak and too few to achieve this driving. For $\rho = 10$ and 100 MΩ · m, this does not happen since the role of these high frequency cells is resized by the better coupling: being the normal-pacing cells in a greater number, their contribution predominates (CL = 773 ± 1 and 746 ± 1 ms). Uncoupled cells have a mean CL of 820 ± 147 ms.

$\sigma = 0.1873$

As already said, this is the degree of heterogeneity that can be found inside the rabbit SAN [39]. In this case, the effect seen with $\sigma = 0.1$ is clearer (Figure 4.6), with the difference that now there are more and stronger fast-pacing cells that manage for $\rho = 1000$ MΩ · m to synchronize all the others. The frequency at which the cells synchronize is indeed higher (CL = 544 ± 1 ms) than the mean frequency of the population (uncoupled condition, CL = 808 ± 228 ms). For the

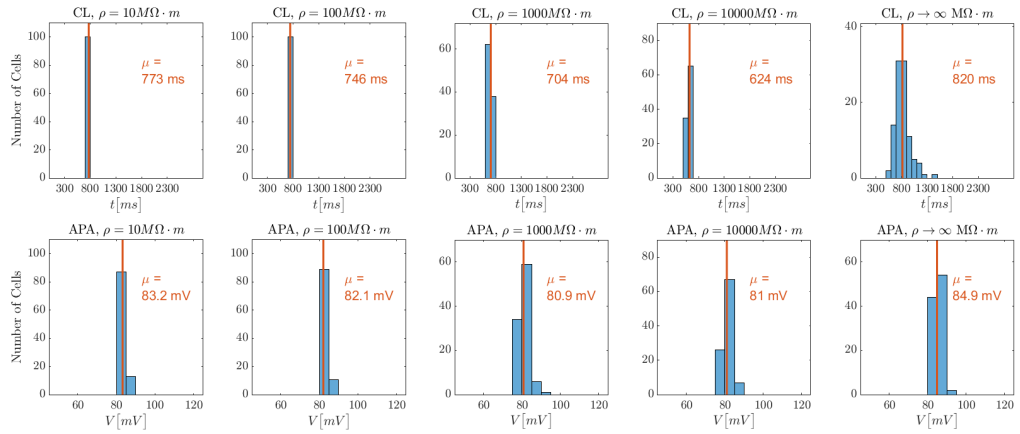

Figure 4.5: Histograms for 1D WT condition with $\sigma = 0.1$: CL (top, bin width = 100 ms) and APA (bottom, bin width = 5 mV) at different gap junctions coupling ($\rho = 10, 100, 1000, 10000$ and $\to \infty$ M$\Omega \cdot$m from left to right). Vertical orange lines represent the mean value of the distributions, whose value is displayed on the right.

same reason this happens also for $\rho = 100$ M$\Omega \cdot$m (CL = 681 $\pm$ 1 ms), and in a lower extent also for $\rho = 10$ M$\Omega \cdot$m (CL = 723 $\pm$ 1 ms), since the role of the normal-pacing cells is still predominant with low ρ. When $\rho = 10000$ M$\Omega \cdot$m, the contribution of the faster cells shifts the CL towards smaller values (581 $\pm$ 72 ms), but the coupling is too weak to allow a perfect synchronization.

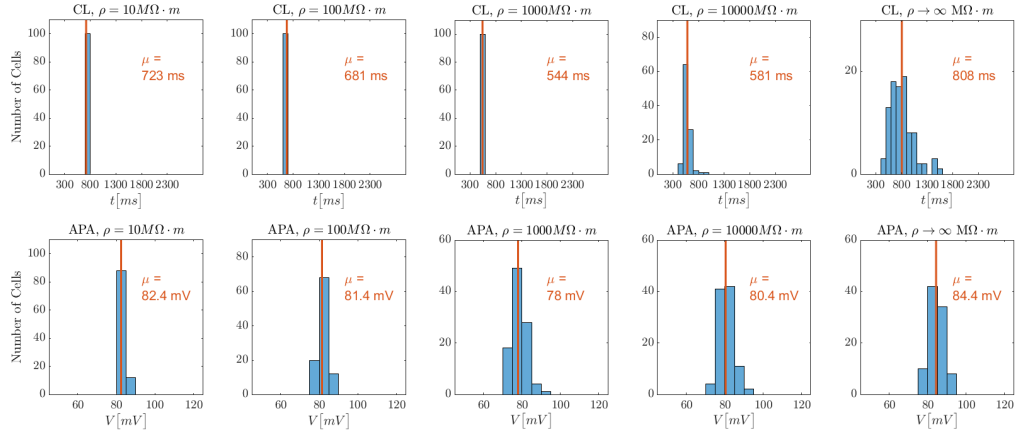

Figure 4.6: Histograms for 1D WT condition with $\sigma = 0.1873$: CL (top, bin width = 100 ms) and APA (bottom, bin width = 5 mV) at different gap junctions coupling ($\rho = 10, 100, 1000, 10000$ and $\to \infty$ M$\Omega \cdot$m from left to right). Vertical orange lines represent the mean value of the distributions, whose value is displayed on the right.

$\sigma = 0.3$

With this level of heterogeneity, cells still manage to synchronize at medium-low resistivities, but - especially for $\rho = 1000\ \mathrm{M\Omega \cdot m}$ - at a higher frequency (CL is 653 ± 1 ms for $\rho = 10\ \mathrm{M\Omega \cdot m}$, 589 ± 1 ms for $\rho = 100\ \mathrm{M\Omega \cdot m}$, 422 ± 1 ms for $\rho = 1000\ \mathrm{M\Omega \cdot m}$, Figure 4.7). For high resistivity ($\rho = 10000\ \mathrm{M\Omega \cdot m}$) CLs are less spread than if the cells are uncoupled, but no synchronization could be achieved by far (CL = 570 ± 136 ms). Uncoupled cells beat at a CL of 790 ± 328 ms.

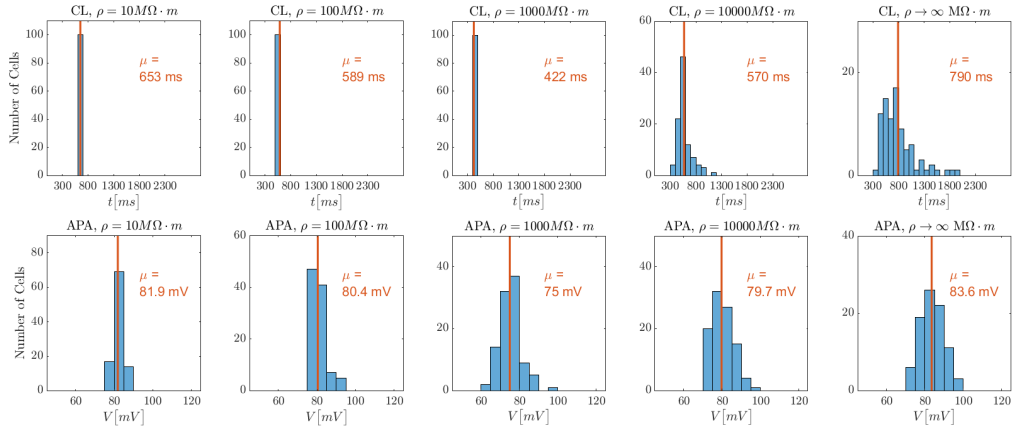

Figure 4.7: Histograms for 1D WT condition with $\sigma = 0.3$: CL (top, bin width = 100 ms) and APA (bottom, bin width = 5 mV) at different gap junctions coupling ($\rho = 10, 100, 1000, 10000$ and $\to \infty\ \mathrm{M\Omega \cdot m}$ from left to right). Vertical orange lines represent the mean value of the distributions, whose value is displayed on the right.

$\sigma = 0.4$

Even with the maximum variability given as an input to the 1D model, the cells synchronize in terms of frequency at medium-low resistivities, even if this happens at a very short mean CL for a human cell (CL is 596 ± 1 ms for $\rho = 10\ \mathrm{M\Omega \cdot m}$, 519 ± 1 ms for $\rho = 100\ \mathrm{M\Omega \cdot m}$, 370 ± 1 ms for $\rho = 1000\ \mathrm{M\Omega \cdot m}$). For $\rho = 10000\ \mathrm{M\Omega \cdot m}$ instead, only a very partial coupling can be obtained, leading to a very large frequency distribution (CL = 582 ± 282 ms), which is anyway smaller than the one that uncoupled cells have (CL = 732 ± 371 ms), because of the residual interaction between them.

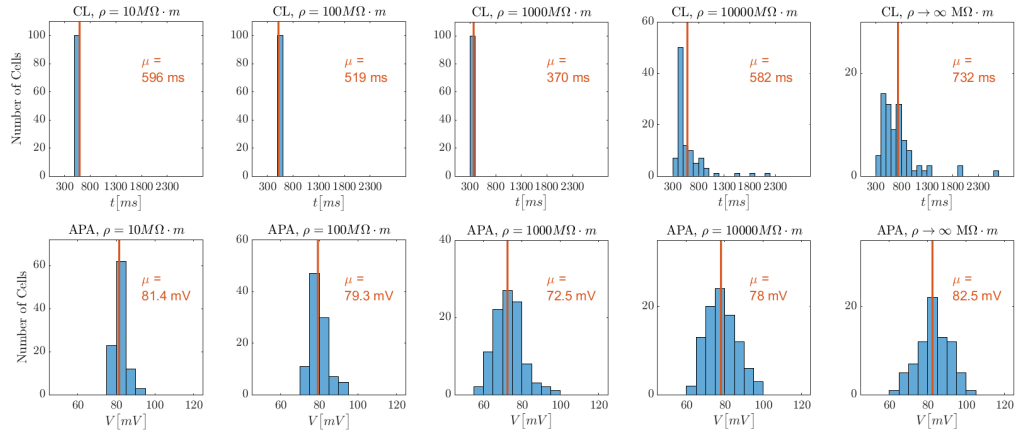

Figure 4.8: Histograms for 1D WT condition with $\sigma = 0.4$: CL (top, bin width = 100 ms) and APA (bottom, bin width = 5 mV) at different gap junctions coupling ($\rho = 10, 100, 1000, 10000$ and $\to \infty$ M$\Omega \cdot$ m from left to right). Vertical orange lines represent the mean value of the distributions, whose value is displayed on the right.

4.1.3 1D WT Model Results at a glance

The graphs in Figures 4.9 and 4.10 sum up what it has been shown so far. At the increase in gap junctions resistance, which reflects a poorer coupling between the cells, it corresponds an increase in the dispersion and a decrease in the duration of the CL. The effect on the dispersion is particularly clear for high resistivities ($\rho = 10000$ M$\Omega \cdot$ m), for which cells are too poorly coupled to achieve a good synchronization. For lower values of ρ instead, cells synchronize completely at every level of heterogeneity (Figure 4.9a). Moreover, the decrease in cellular coupling increases the importance of the cells that have a higher intrinsic frequency. On one hand, in this condition they are protected from the slower ones - which would have an inhibitory effect, being them in a more hyperpolarized phase; on the other hand, they manage to deliver a sufficient depolarizing current to their neighbouring cells. This role persists as long as the coupling is strong enough, whereas it ends for high resistivities ($\rho = 10000$ or $\rho = \to \infty$ M$\Omega \cdot$ m), where high frequency cells are unable to stimulate the other ones. The trends for the APA are similar (Figure 4.9b), but they surely show a bigger variability also at low resistivities, as it is assessable from the previous histograms. This result highlights the fact that cells have a minor tendency to couple their APA with the respect to the above discussed CL.

The effect of the heterogeneity is similar but with some peculiarities (Figure 4.10a): in general, to higher standard deviations corresponds - apart from the expected larger dispersion in the features - a lower mean CL, since there are more fast-pacing cells that tend to drive the entire fiber model. Opposite to this, it is the

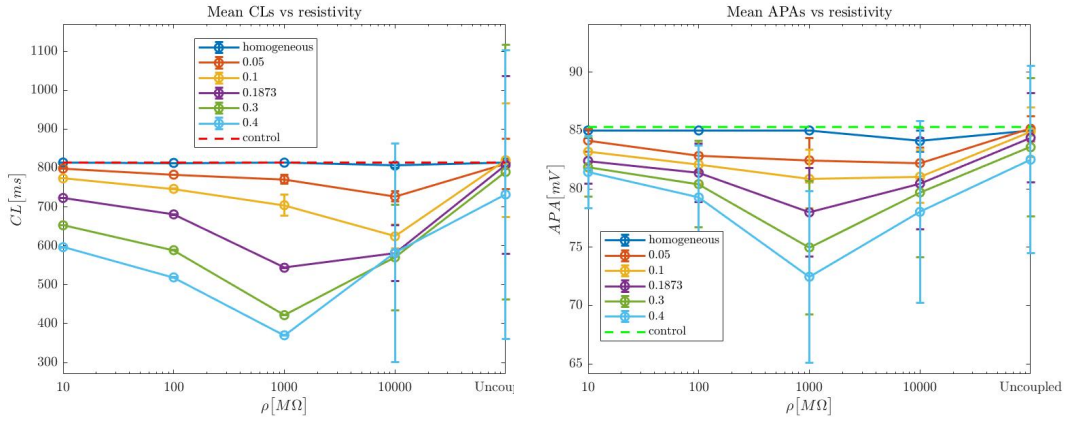

(a) *(b)*

Figure 4.9: Trends of CL and APA (± standard deviation) with respect to resistivity for different levels of cellular heterogeneity ($\sigma = 0.05, 0.1, 0.1873, 0.3$ and 0.4) and nominal values (CL = 814 ms, APA = 85.3 mV, dashed lines); 1D WT condition.

result for $\rho = 10000\ \mathrm{M\Omega \cdot m}$, where at high standard deviations there seems to be a "saturation" effect: from $\sigma = 0.1873$, through $\sigma = 0.3$ to $\sigma = 0.4$ the mean CL remains more or less the same (581, 570, 582 ms respectively). This is probably due to the fact that even if fast-pacing cells are more and faster, the poor coupling prevents them from delivering the stimulus current to other cells beyond a certain level. About the APA, Figure 4.10b confirms the previously reported dispersion of this feature even at low ρ. A notable thing is that for $\rho = 10000\ \mathrm{M\Omega \cdot m}$, the curve has the same trend as the other ones - contrarily to the CL - showing a decrease in mean APA at the increase in σ. An excessive decrease in APA can be dangerous, since this could mean that the MDP is too high (i.e. depolarized), leading to a minor contribution of I_f and therefore to a longer CL, being this current activated at low potentials. A reduced amplitude could also be due to a lower OS, but this condition is less critical, even if it highlights an increased struggle by the cells.

If the cells are uncoupled, with increasing values of heterogeneity, many cells progressively stop beating. This is the reason why in an uncoupled condition, CL is shorter at high σ and this also explains why in some cases the distributions of CL are less dispersed for bigger values of σ. For example, cell number 26 has a CL of 1483 ms at $\sigma = 0.1873$, but stops beating at $\sigma = 0.3$ (Figure 4.11).

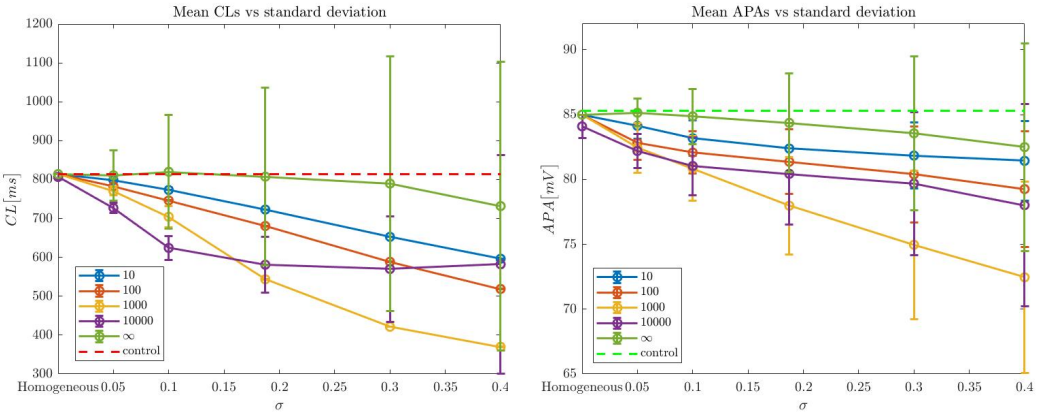

(a) *(b)*

Figure 4.10: Trends of CL and APA (± standard deviation) with respect to standard deviation for different values of gap junctions resistivity ($\rho = 10, 100, 1000, 10000$ and $\rightarrow \infty$ MΩ · m) and nominal values (CL = 814 ms, APA = 85.3 mV, dashed lines); 1D WT condition.

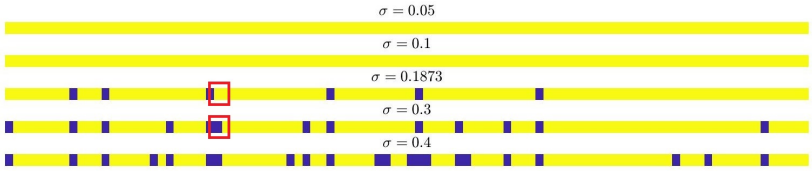

Figure 4.11: Color maps of the 1D WT model ($\rho \rightarrow \infty$ MΩ · m): the color blue represents the cells that do not show action potentials, yellow represents cells with electrical activity. With the increase of cellular heterogeneity, the number of non-excitable cells grows: 0 for $\sigma = 0.05$ and 0.1; 6 (6 %) for $\sigma = 0.1873$; 13 (13 %) for $\sigma = 0.3$; 22 (22 %) for $\sigma = 0.4$. Red squares highlight cell number 26, which stops beating in the transition between $\sigma = 0.1873$ and $\sigma = 0.3$.

4.1.4 1D Double Mutant condition

The distributions of the features appear similar to the wild type condition, but with the difference that in this case the mutation affects the mean duration of the CL. In Figure 4.12 indeed, it can be noticed that the mode values of the distributions depart from the dashed line of the nominal control value. For homogeneous cells, the mean CL is 1019 ms, with respect to 814 ms (+20.1 %) of the healthy condition. This is expected, since it is just the replication of the single cell result. If the cells are coupled with different conductances instead, the model behaves similarly to the control condition: the pacing frequency tends to increase proportionally with the growth of heterogeneity. Also the rise in gap junction resistivity

leads to a faster pacing, but only until this parameter is not too big for the cells to interact with one another.

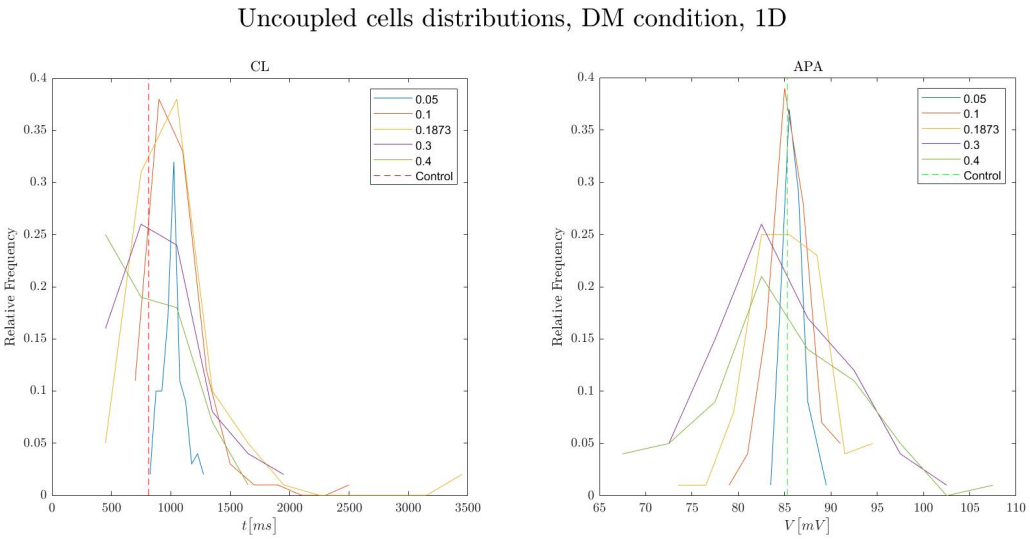

Figure 4.12: CL (left) and APA (right) distributions for uncoupled cells for different values of standard deviation ($\sigma = 0.05, 0.1, 0.1873, 0.3, 0.4$) and nominal values (CL = 814 ms, APA = 85.3 mV, dashed lines); 1D DM condition.

Homogeneous cells ($\sigma = 0$)

As previously stated, uncoupled cells beat all with a CL of 1019 ms; they do the same if they are coupled with resistivities of 10, 100 and 1000 $M\Omega \cdot m$, therefore in this conditions they are synchronized, even if at a lower frequency with respect to the wild type because of the mutations (Figure 4.13). Instead, if cells are connected through low-conductance gap junctions ($\rho = 10000\ M\Omega \cdot m$), they are slightly faster (CL = 1010 $\pm$ 9 ms).

$\sigma = 0.05$

With this variability uncoupled cells ($\rho \to \infty\ M\Omega \cdot m$) have a mean CL of 1017 $\pm$ 93 ms; thanks to the coupling, the dispersion and the mean frequency decreases with the concurrent decrease in resistivity: cells coupled with $\rho = 10000\ M\Omega \cdot m$ have CL = 901 $\pm$ 22 ms, for $\rho = 1000\ M\Omega \cdot m$, CL is 966 $\pm$ 15 ms and for $\rho = 100\ M\Omega \cdot m$, CL = 977 $\pm$ 1 ms (Figure 4.14). For $\rho = 10\ M\Omega \cdot m$, CLs appear distributed on different values, but this is only for the fact that some of them are

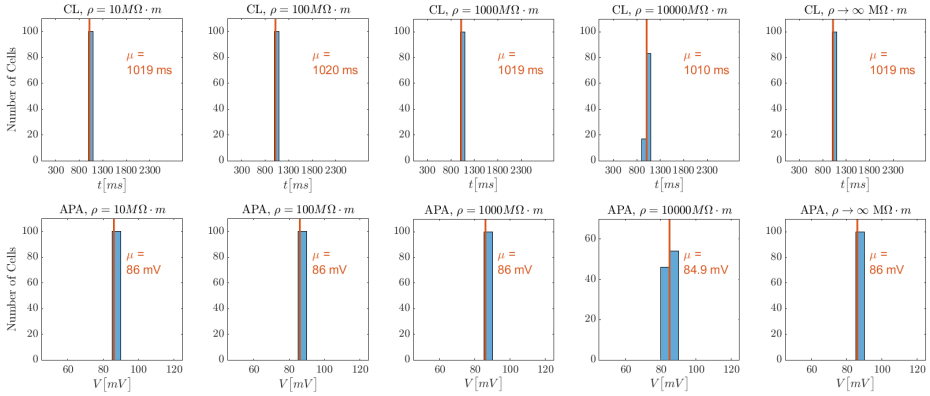

Figure 4.13: Histograms for 1D DM condition homogeneous condition: CL (top, bin width = 100 ms) and APA (bottom, bin width = 5 mV) at different gap junctions coupling ($\rho = 10, 100, 1000, 10000$ and $\to \infty$ M$\Omega \cdot$ m from left to right). Vertical orange lines represent the mean value of the distributions, whose value is displayed on the right.

slightly more than 1000 ms and therefore fall inside another bin, being the mean value 999 ms. The obtained standard deviation (1 ms) does not justify indeed the presence of two different bins.

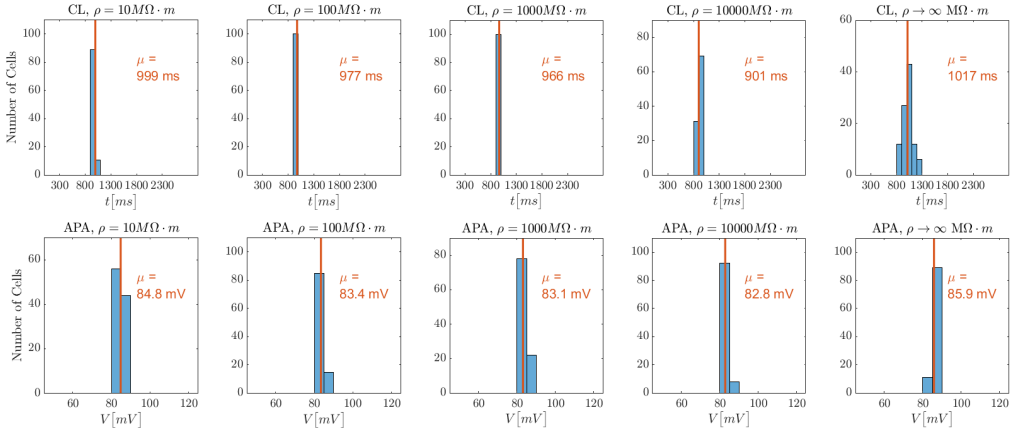

Figure 4.14: Histograms for 1D DM condition with $\sigma = 0.05$: CL (top, bin width = 100 ms) and APA (bottom, bin width = 5 mV) at different gap junctions coupling ($\rho = 10, 100, 1000, 10000$ and $\to \infty$ M$\Omega \cdot$ m from left to right). Vertical orange lines represent the mean value of the distributions, whose value is displayed on the right.

$\sigma = 0.1$

The uncoupled cells distribution (Figure 4.15) highlights that there are very slow cells (CL_{max} = 2573 ms) that contribute to extend the duration of the mean cy-

cle length, which is now 1046 ± 257 ms. Synchronization is reached for $\rho <= 1000\ \mathrm{M\Omega \cdot m}$, but at a higher frequency for poorer couplings: CL = 967 ± 1 ms ($\rho = 10\ \mathrm{M\Omega \cdot m}$), CL = 928 ± 1 ms ($\rho = 100\ \mathrm{M\Omega \cdot m}$) and CL = 859 ± 1 ms ($\rho = 1000\ \mathrm{M\Omega \cdot m}$). Even if faster cells try to drive all the other ones at a higher frequency, for $\rho = 10000\ \mathrm{M\Omega \cdot m}$ a uniform timing is not achieved (CL = 756 ± 46 ms).

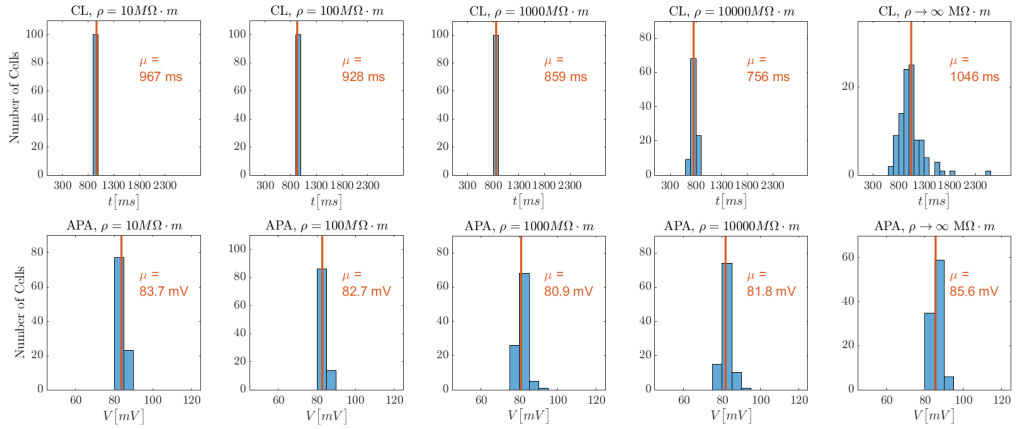

Figure 4.15: Histograms for 1D DM condition with $\sigma = 0.1$: CL (top, bin width = 100 ms) and APA (bottom, bin width = 5 mV) at different gap junctions coupling ($\rho = 10, 100, 1000, 10000$ and $\to \infty\ \mathrm{M\Omega \cdot m}$ from left to right). Vertical orange lines represent the mean value of the distributions, whose value is displayed on the right.

$\sigma = 0.1873$

The previous result is emphasized: for $\rho <= 1000\ \mathrm{M\Omega \cdot m}$, synchronization is still achieved, but at higher frequencies because of the heavier role of fast-pacing cells: CL = 903 ± 1 ms with $\rho = 10\ \mathrm{M\Omega \cdot m}$, CL = 845 ± 1 ms with $\rho = 100\ \mathrm{M\Omega \cdot m}$ and CL = 662 ± 1 ms with $\rho = 10\ \mathrm{M\Omega \cdot m}$. A wide distribution is now present if the cells are poorly coupled $\rho = 10000\ \mathrm{M\Omega \cdot m}$: CL is 689 ± 127 ms. Even if some cell that had a long CL is "dead" (i.e. it lost his spontaneous activity) now, for $\rho \to \infty\ \mathrm{M\Omega \cdot m}$ there is still a sufficient number of them able to provide as an output a mean CL that is longer than the homogeneous case: 1040 ± 463 ms vs 1019 ms. An analysis on non-excitable cells, with the comparison between WT and DM condition, will be made at the end of Section 4.2.5.

$\sigma = 0.3$

Opposite to what just stated for the $\sigma = 0.1873$ case, with $\sigma = 0.3$ many slow cells are no more excitable, therefore the mean CL in the uncoupled condition

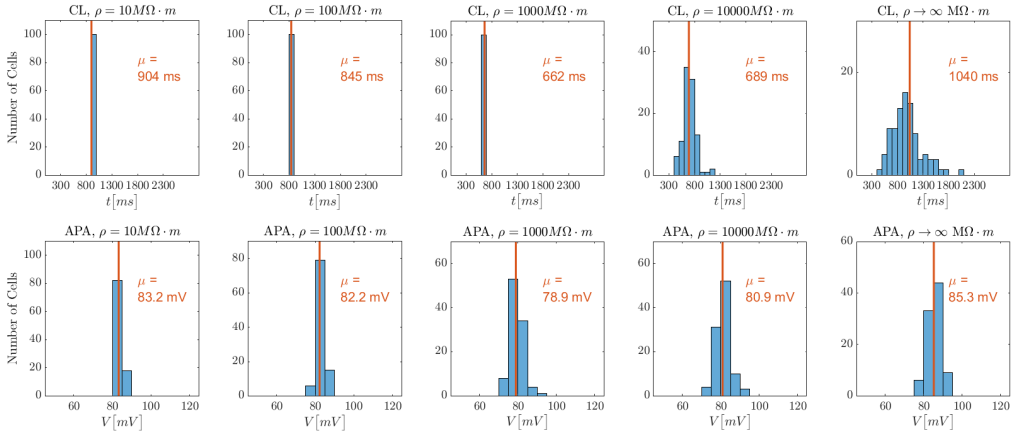

Figure 4.16: Histograms for 1D DM condition with $\sigma = 0.1873$: CL (top, bin width = 100 ms) and APA (bottom, bin width = 5 mV) at different gap junctions coupling ($\rho = 10, 100, 1000, 10000$ and $\to \infty$ M$\Omega \cdot$ m from left to right). Vertical orange lines represent the mean value of the distributions, whose value is displayed on the right.

is shorter than the homogeneous case: 906 $\pm$ 354 ms (Figure 4.17). The $\rho <=$ 10000 M$\Omega \cdot$ m case has, as expected, a shorter and more dispersed CL than before (645 $\pm$ 174), whereas with the other parameters settings, synchronization is always reached (CL = 814 $\pm$ 1 ms for $\rho = 10$ M$\Omega \cdot$ m, CL = 724 $\pm$ 1 ms for $\rho = 100$ M$\Omega \cdot$ m and CL = 457 $\pm$ 1 ms for $\rho = 1000$ M$\Omega \cdot$ m).

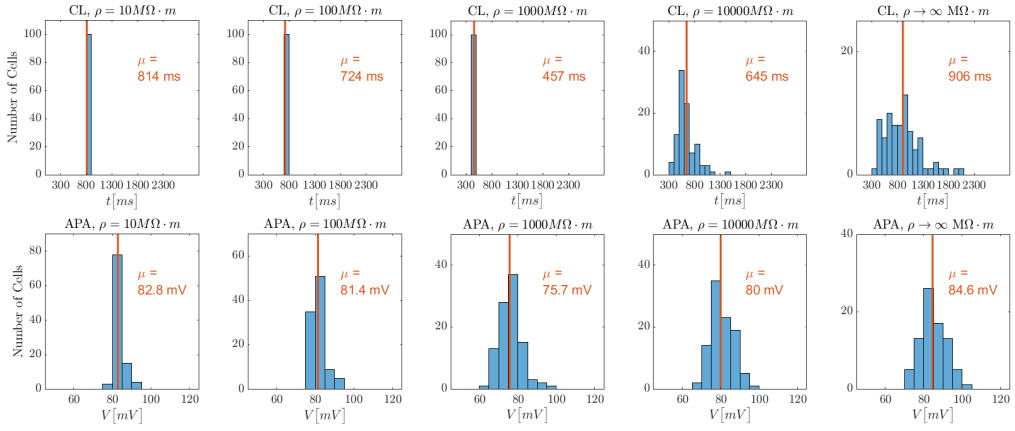

Figure 4.17: Histograms for 1D DM condition with $\sigma = 0.3$: CL (top, bin width = 100 ms) and APA (bottom, bin width = 5 mV) at different gap junctions coupling ($\rho = 10, 100, 1000, 10000$ and $\to \infty$ M$\Omega \cdot$ m from left to right). Vertical orange lines represent the mean value of the distributions, whose value is displayed on the right.

$\sigma = 0.4$

Even with the maximum standard deviation imposed, mutated cells achieve a complete synchronization in frequency if the resistivity is less or equal to 1000 MΩ · m, just as the healthy ones do (CL = 741 ± 1 ms for $\rho = 10$ MΩ · m, CL = 619 ± 1 ms for $\rho = 100$ MΩ · m and CL = 384 ± 1 ms for $\rho = 10$ MΩ · m, Figure 4.18). As usual instead, a resistivity of $\rho = 10000$ MΩ · m represents a too poor coupling for the cells to beat at the same frequency, therefore CL is widely spread (662 ± 554 ms), in this case more than the uncoupled condition (CL = 793 ± 306 ms). This is interestingly due to the fact that the 52nd cell of the fiber model has a last beat with a remarkably long CL (5248 ms; in the panel for $\rho = 10000$ MΩ · m in Figure 4.18 x axis limits were expanded to 5400 ms in order to show this spread bin). If this cell is uncoupled from other cells, it remains silent (Figure 4.19) since its parameters do not allow the onset of the AP (Table 4.3); if anyway it receives a little depolarizing contribution from neighbouring cells, it is able to show an action potential. The more compact distribution of the uncoupled condition is therefore explained by the absence of this cell, that acts as an outlier on the distribution of the $\rho = 10000$ MΩ · m case. Without its contribution indeed, the mean CL goes down to 614 ms (-7.2 %), but mostly its standard deviation becomes 294 ms (-46.9 %).

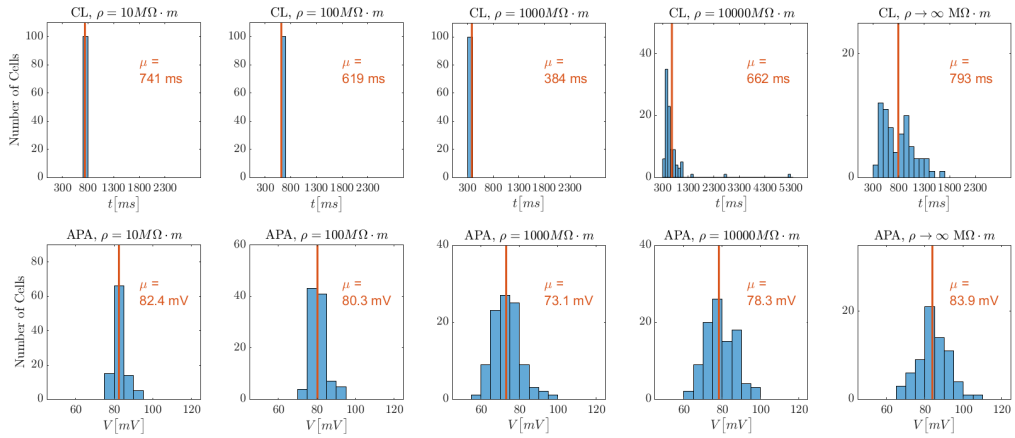

Figure 4.18: Results for 1D DM condition with $\sigma = 0.4$: CL (top, bin width = 100 ms) and APA (bottom, bin width = 5 mV) at different gap junctions coupling ($\rho = 10, 100, 1000, 10000$ and $\rightarrow \infty$ MΩ · m from left to right). Vertical orange lines represent the mean value of the distributions, whose value is displayed on the right.

Figure 4.20 shows the progressive decrease in the number of autorithmic cells due to increased cellular heterogeneity.

Permeability	$[nA/mM]$	**Conductance**	$[\mu S]$	**Current**	$[nA]$
P_{CaL}	0.5538	g_{KACh}	0.00348	I_{NaKmax}	0.12257
P_{CaT}	0.07269	g_{Kr}	0.00416	$_{NaCa}$	3.757
		g_{Ks}	0.000128		
		g_{Kur}	$1.255 \cdot 10^{-3}$		
		g_{Na}	0.0223		
		g_f	0.00453		
		g_{to}	$6.1 \cdot 10^{-3}$		

Table 4.3: Parameters for the 52nd cell of the 1D DM condition ($\sigma = 0.4$), with a CL of 5248 ms

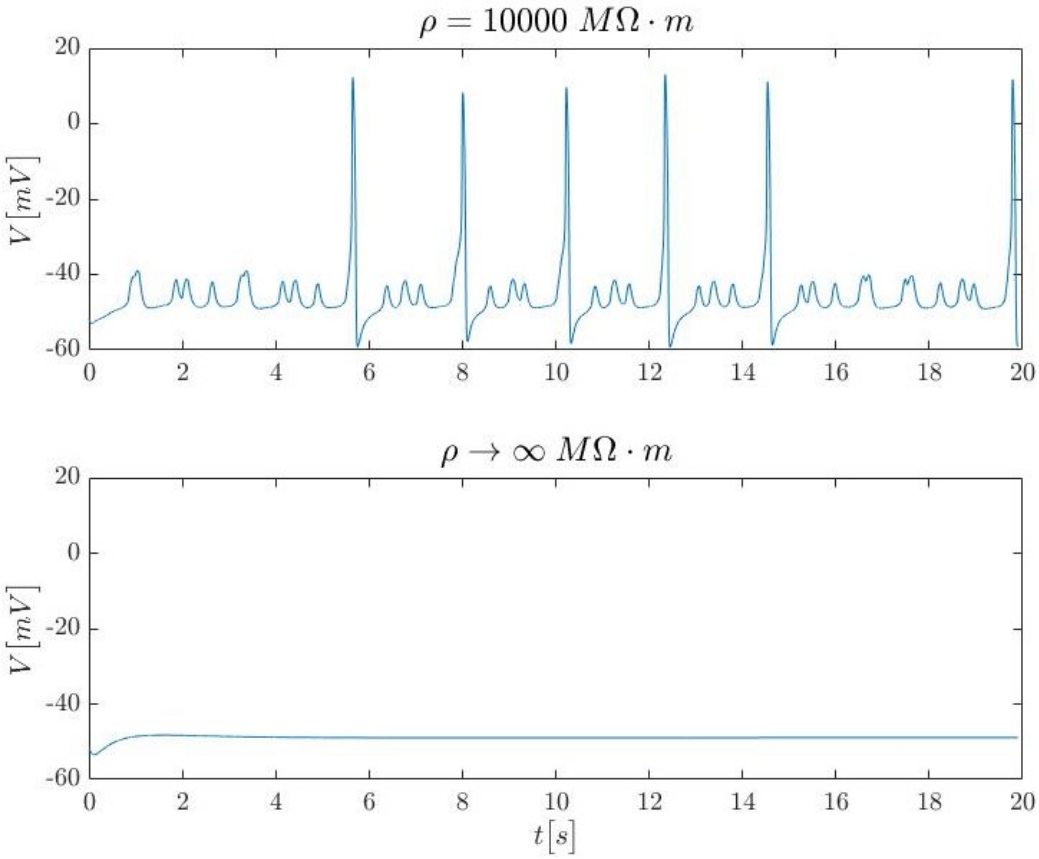

Figure 4.19: Activity of the 52nd cell of the fiber model ($\sigma = 0.4$, 1D DM condition): if this cell receives a minimal contribution ($\rho = 10000\ \mathrm{M\Omega \cdot m}$, top) from the neighbouring cells, it is able to achieve an action potential; instead, if it is totally uncoupled, it does not show any electrical activity ($\rho \to \infty\ \mathrm{M\Omega \cdot m}$, bottom).

4.1.5 1D DM Model Results at a glance

Similarly to the WT condition, the graphs in Figures 4.21 and 4.22 sum up what has been told so far for the mutated case. The trends of CL with respect to resis-

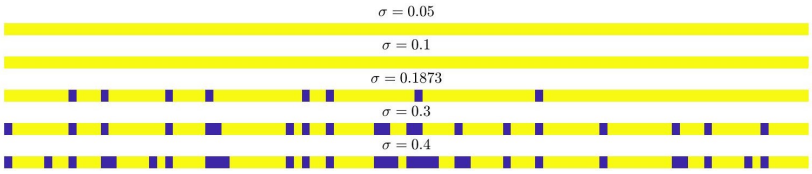

Figure 4.20: Color maps of the 1D DM model ($\rho \to \infty$ M$\Omega \cdot$ m): the color blue represents the cells that do not show action potentials, yellow represents cells with electrical activity. With the increase of cellular heterogeneity, the number of non-excitable cells grows: 0 for $\sigma = 0.05$; 1 (1 %) for $\sigma = 0.1$; 8 (8 %) for $\sigma = 0.1873$; 20 (20 %) for $\sigma = 0.3$; 30 (30 %) for $\sigma = 0.4$.

tivity and standard deviation are similar to that of the wild type condition (Figures 4.21a and 4.22a): I) decreasing the cellular coupling (i.e. increasing ρ) provides a higher frequency since faster cells are not inhibited by slower ones because of the protection of the poorer coupling (Figure 4.21a). This is true until ρ is too high (10000 M$\Omega \cdot$ m), condition in which the coupling is too poor to allow cells to influence each other. In this case indeed the standard deviation of the parameters is almost as high as in the uncoupled condition. II) An increase in dispersion of cellular parameters gives as a result a shorter CL, namely a higher pacing frequency (Figure 4.22a). This is due to the fact that slow cells become non-excitable with high σ; furthermore, if the cells are coupled, the main role is played by the faster ones which stimulate the others. Thus, mean CL decreases for these two reasons. $\rho = 10000$ M$\Omega \cdot$ m is an exception also in this condition: this resistivity is too high to allow fast cells to decrease the mean frequency beyond a certain degree (689, 645 and 662 ms for $\sigma = 0.1873$, 0.3 and 0.4 respectively.): mean CL is not shortened proportionally, but it "saturates". Regarding APA, nothing different from the WT condition was obtained with the mutation (Figures 4.21b and 4.22b): for low or high resistivities, mean APA is more similar to the nominal value than for $\rho = 1000$ M$\Omega \cdot$ m, since in those cases the cells are either totally coupled or can not influence each other in a relevant way. Halfway these two conditions, with $\rho = 1000$ M$\Omega \cdot$ m and a high degree of σ, for which the electrical load is highly heterogeneous, cells influence each other and therefore deliver a big current, thus reducing the amplitude of the AP.

The main difference with respect to the WT condition, as appears in Figures 4.21a and 4.22a, is the mean intrinsic CL of the cells, which in this case is substantially longer due to the mutations, as it was already obtained with the single cell model. However, high cellular heterogeneity and medium couplings ($\rho = 1000$ M$\Omega \cdot$ m), provide even in this case very short mean CLs, up to 384 ms. This value is similar to the maximum value of the mean CL obtained for the healthy condition (370 ms), meaning that cellular heterogeneity strongly compen-

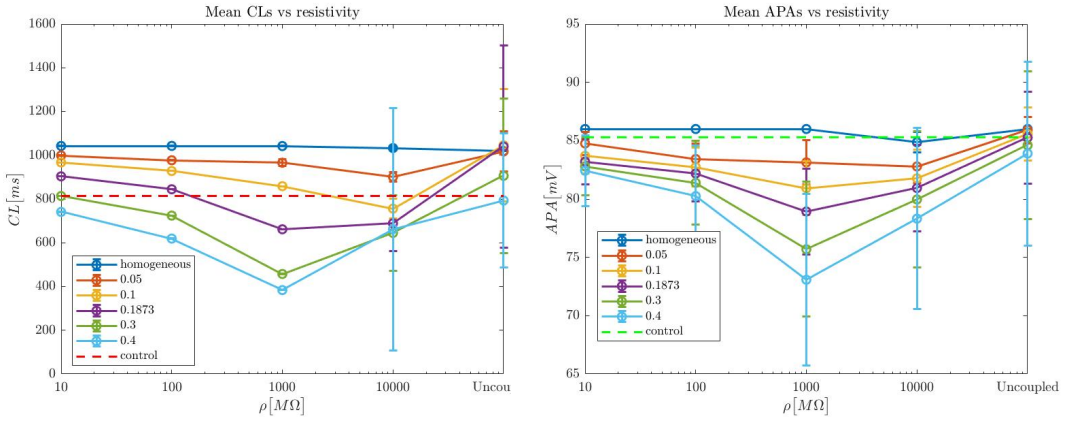

(a) *(b)*

Figure 4.21: Trends of CL and APA (± standard deviation) with respect to resistivity for different levels of cellular heterogeneity ($\sigma = 0.05, 0.1, 0.1873, 0.3$ and 0.4) and nominal control values (CL = 814 ms, APA = 85.3 mV). 1D DM condition.

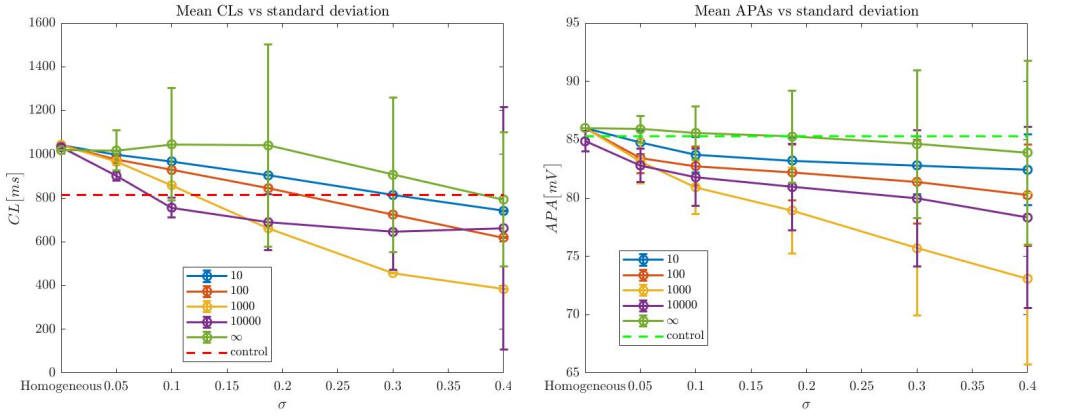

(a) *(b)*

Figure 4.22: Trends of CL and APA (± standard deviation) with respect to standard deviation for different values of gap junctions resistivity ($\rho = 10, 100, 1000, 10000$ and $\to \infty$ MΩ · m) and nominal control values (CL = 814 ms, APA = 85.3 mV). 1D DM condition.

sates for the effect of the mutation in both conditions. With this coupling, mean CL passed from 1019 ms (homogeneous case) to 384 ms ($\sigma = 0.4$), with a variation of -62.3%, bigger than the -54.5% of the WT (from 814 to 370 ms). The fact that cells have different parameters constitutes, as one would expect, a factor of robustness of the SAN system, since it reduces the detrimental effect of a loss of function of a fundamental current as I_f is.

Considering the supposed physiological values of heterogeneity ($\sigma = 0.1873$) and gap junctions resistivity ($\rho = 100\ \mathrm{M\Omega \cdot m}$, corresponding to a conductivity of $10\,\mathrm{nS/m}$, which is halfway the interval reported for the rabbit SAN [14]), it seems that the contribution of fast-pacing cells is too strong, bringing the CL of the WT condition from 814 to 681 ms and the one of the DM condition from 1019 to 845 ms. This could suggest that the human SAN has a lower degree of heterogeneity than the rabbit one ($\sigma = 0.1873$). Anyway this is unrealistic, since this feature represents a factor of robustness of the functioning of biological systems in general, and the human heart is probably more reliable than the rabbit one (but this is just an hypothesis).

More likely, this phenomenon is due to the simplifications made in the model, first of all having considered only one dimension instead of a 3D structure with a complex shape. If indeed the fast-pacing cells are surrounded by normal-pacing ones (as in a 3D tissue), the latters would have an inhibitory effect on them, since they would constitute a bigger load. Thus, they would slow fast-pacing cells down and therefore they would provide a mean CL more similar to the nominal one.

This hypothesis is supported by the results of the 2D simulations, which will be shown below.

4.2 2D Model Analysis

4.2.1 2D Parameter Randomization

Figure 4.23 shows the log-normal distributions of the parameters that have been randomized. Being now the number of cells equal to 2500, the shape of the distributions appears much smoother than the 1D case. WT and DM condition distributions coincides except for the g_f one, which was in the latter case multiplied by a factor 0.08 to simulate the effect of the mutations, as already did in 1D. The maximum, mean and minimum values for this conductance can be found again in two tables: Table 4.4 and Table 4.5 respectively for the WT and DM conditions.

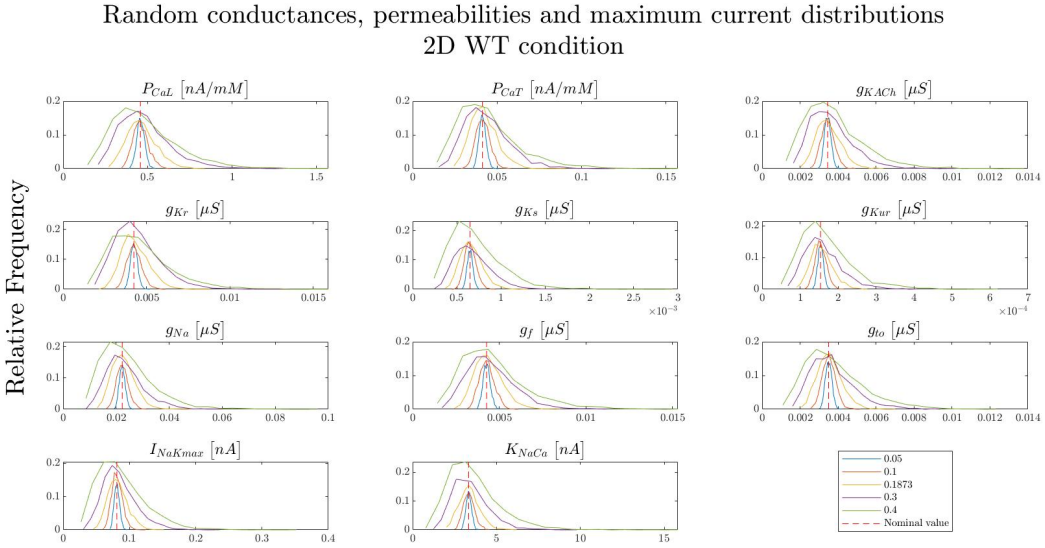

Figure 4.23: Comparison between the distributions of the parameters randomized in the study for the WT condition at different standard deviation levels. The DM condition has the same distribution of the WT one, except for g_f which is multiplied by a factor 0.08. Exact values for g_f are reported in Tables 4.4 and 4.5 respectively for the WT and DM conditions.

4.2.2 2D Wild Type condition

The uncoupled cells distributions for CL and APA are shown in Figure 4.24: higher levels of standard deviation (heterogeneity) lead to more widely spread distributions around the nominal values (814 ms for CL and 85.3 mV for APA). This is because cells have their own intrinsic frequency and with $\rho \to \infty$ M$\Omega \cdot$ m can not interact with one another to synchronize their pacing or amplitude.

	σ				
g_f	**0.05**	**0.1**	**0.1873**	**0.3**	**0.4**
mean	0.004 28	0.004 28	0.004 38	0.004 51	0.004 66
min	0.003 66	0.003 02	0.002 33	0.0015	$9.22 \cdot 10^{-4}$
max	0.005 00	0.006 09	0.008 35	0.011 11	0.015 16

Table 4.4: Conductance values for funny current at different values of standard deviation; WT condition (nominal value $g_f = 0.004\,27\,\mu S$)

	σ				
g_f	**0.05**	**0.1**	**0.1873**	**0.3**	**0.4**
mean	$3.42 \cdot 10^{-4}$	$3.44 \cdot 10^{-4}$	$3.49 \cdot 10^{-4}$	$3.57 \cdot 10^{-4}$	$3.70 \cdot 10^{-4}$
min	$2.93 \cdot 10^{-4}$	$2.51 \cdot 10^{-4}$	$1.91 \cdot 10^{-4}$	$1.35 \cdot 10^{-4}$	$9.88 \cdot 10^{-5}$
max	$4.00 \cdot 10^{-4}$	$4.69 \cdot 10^{-4}$	$6.18 \cdot 10^{-4}$	$8.83 \cdot 10^{-4}$	0.0012

Table 4.5: Conductance values for funny current at different values of standard deviation; DM condition (Nominal value $g_f = 3.42 \cdot 10^{-4}\,\mu S$)

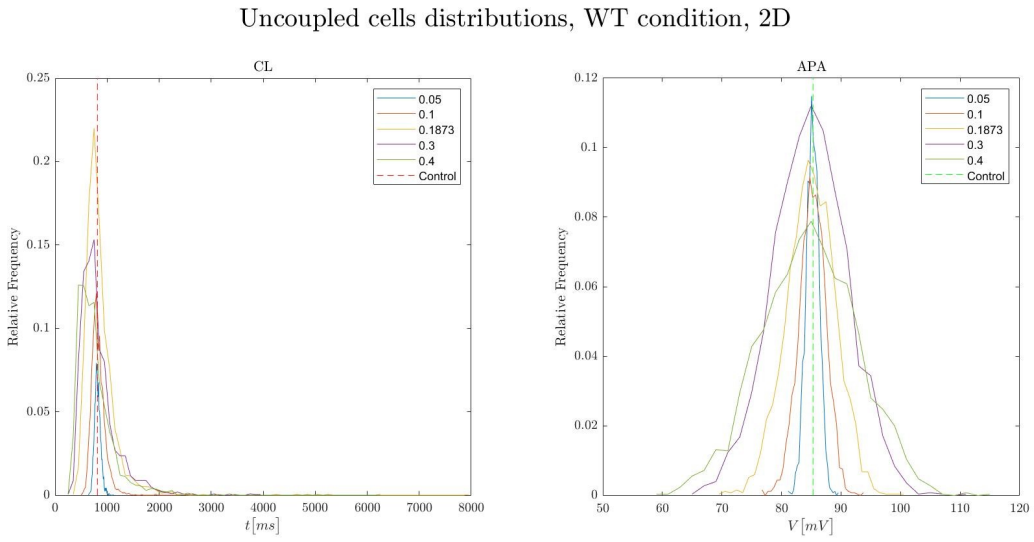

Figure 4.24: CL (left) and APA (right) distributions for uncoupled cells for different values of standard deviation ($\sigma = 0.05, 0.1, 0.1873, 0.3, 0.4$) and nominal values (CL = 814 ms, APA = 85.3 mV, dashed lines); 2D WT condition.

If on the contrary cells are coupled together, they will show different behaviours depending on the resistivity of the gap junction they were connected with. Similarly to the 1D case indeed, higher ρ hinder synchronization between cells in terms of frequency and phase. The heterogeneity has a dual effect instead: on one hand it provides more fast-pacing cells which are able to drive the other ones; on the other hand it spreads the distributions of CL and APA (Figure

4.24), thus making it more difficult for the cell to couple. Therefore the final result depends both on ρ and σ.

The results for the specific cases, at different levels of standard deviation, will be now shown and discussed.

Homogeneous cells ($\sigma = 0$)

The uncoupled condition presents as expected a mean CL of 814 ms, as every cell was set with the nominal values of all the model parameters. For $\rho = 10, 100$ and 1000 $M\Omega \cdot m$ CL has a slightly different duration (815 $\pm$ 1 ms, 813 $\pm$ 1 ms and 813 $\pm$ 1 ms respectively) because of the different initial conditions. An almost complete synchronization is achieved even with $\rho = 10000$ $M\Omega \cdot m$, but at a surprisingly high frequency: CL = 547 $\pm$ 19 ms (Figure 4.25).

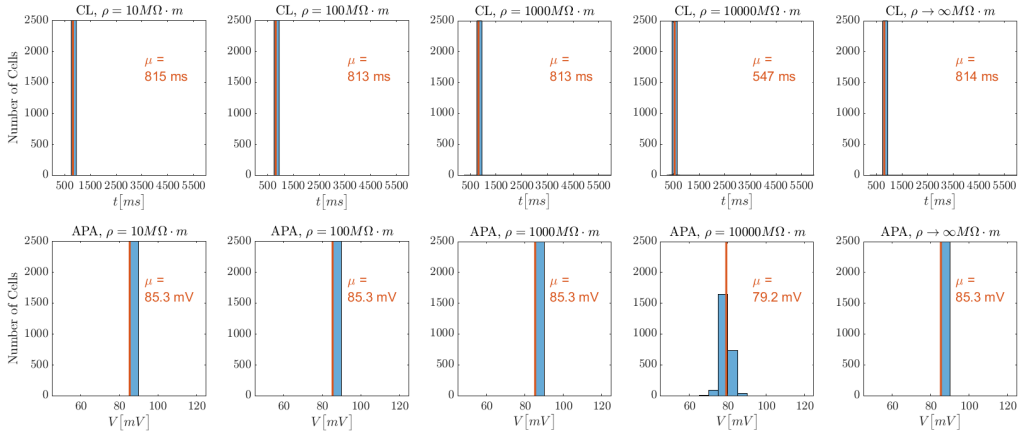

Figure 4.25: Histograms for 2D WT homogeneous condition: CL (top, bin width = 100 ms) and APA (bottom, bin width = 5 mV) at different gap junctions coupling ($\rho = 10, 100, 1000, 10000$ and $\to \infty$ $M\Omega \cdot m$ from left to right). Vertical orange lines represent the mean value of the distributions, whose value is displayed on the right.

$\sigma = 0.05$

An almost perfect synchronization is reached in all cases (Figure 4.26), only $\rho =$ 10000 $M\Omega \cdot m$ shows few cells not timed to the other ones (even if they all fall in the same bin): CL = 560 $\pm$ 11 ms. For lower resistivities, synchronization is totally achieved: CL = 813 $\pm$ 1 ms ($\rho = 10$ $M\Omega \cdot m$), CL = 812 $\pm$ 1 ms ($\rho =$ 100 $M\Omega \cdot m$) and CL = 803 $\pm$ 2 ms ($\rho = 1000$ $M\Omega \cdot m$, the two bins are again explained by the fact that the mean CL value is near the threshold - 800 ms - between two different bins, and therefore some CL fall inside another bin even if the dispersion is minimal: 2 ms). The duration of the mean CL for $\rho \to \infty$ $M\Omega \cdot m$

is slightly longer with respect to the nominal value in the homogeneous case: 817 $\pm$ 58 ms.

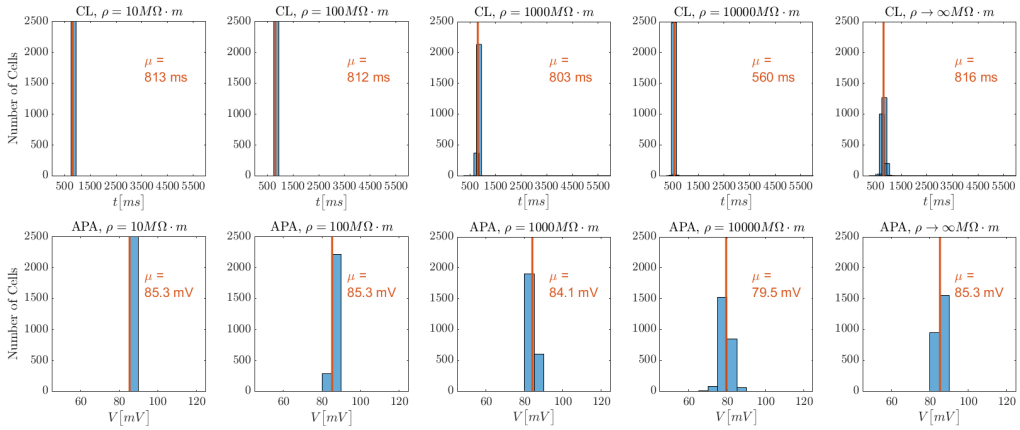

Figure 4.26: Histograms for 2D WT condition with $\sigma = 0.05$: CL (top, bin width = 100 ms) and APA (bottom, bin width = 5 mV) at different gap junctions coupling ($\rho = 10, 100, 1000, 10000$ and $\to \infty$ M$\Omega \cdot$ m from left to right). Vertical orange lines represent the mean value of the distributions, whose value is displayed on the right.

$\sigma = 0.1$

This case is similar to the previous one, with an almost complete synchronization in all cases (Figure 4.27): CL = 811 $\pm$ 1 ms ($\rho = 10$ M$\Omega \cdot$ m), CL = 808 $\pm$ 1 ms ($\rho = 100$ M$\Omega \cdot$ m), CL = 764 $\pm$ 3.9 ms ($\rho = 1000$ M$\Omega \cdot$ m) and CL = 558 $\pm$ 19 ms ($\rho = 10000$ M$\Omega \cdot$ m). This demonstrates that in 2D, being there more connections between the cells, they can interact more and therefore can more easily lead to synchronism. With $\rho = 10000$ M$\Omega \cdot$ m for example, the 2D model has a standard deviation for CL of 19 ms, smaller than that of the 1D case (31 ms). Finally, the mean CL value in the uncoupled condition continues on its growing trend, being now 829 $\pm$ 136 ms.

$\sigma = 0.1873$

Up to this standard deviation in the parameters (which, as already stated, is the measure of heterogeneity present in the rabbit SAN), a perfect synchronous timing is achieved for $\rho <= 1000$ M$\Omega \cdot$ m (Figure 4.28). Indeed, for $\rho = 10$ M$\Omega \cdot$ m CL is 806 $\pm$ 1 ms, for $\rho = 100$ M$\Omega \cdot$ m CL is 794 $\pm$ 1 ms and for $\rho = 1000$ M$\Omega \cdot$ m CL is 666 $\pm$ 3 ms. The coupling with $\rho = 10000$ M$\Omega \cdot$ m begins instead to be more spread (CL = 530 $\pm$ 28 ms), even if less than in the 1D case (CL = 581 $\pm$ 72 ms).

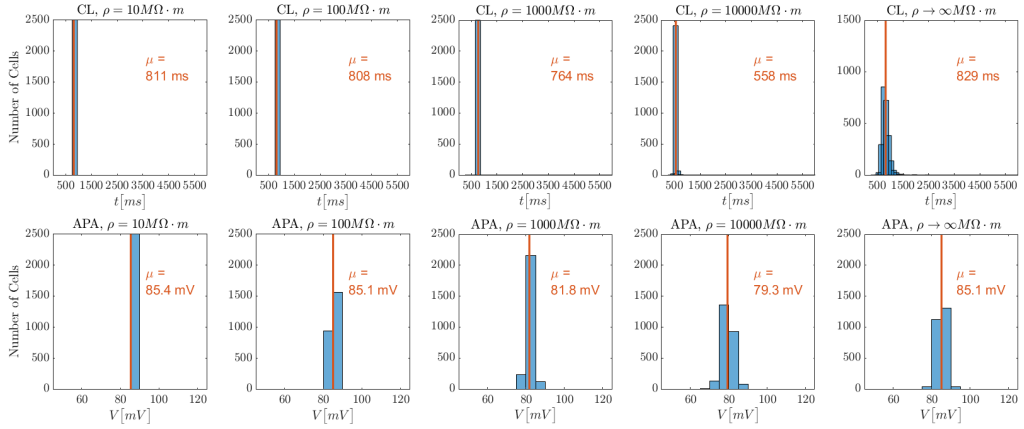

Figure 4.27: Histograms for 2D WT condition with $\sigma = 0.1$: CL (top, bin width = 100 ms) and APA (bottom, bin width = 5 mV) at different gap junctions coupling ($\rho = 10, 100, 1000, 10000$ and $\to \infty$ $\mathrm{M\Omega \cdot m}$ from left to right). Vertical orange lines represent the mean value of the distributions, whose value is displayed on the right.

This represents anyway an extremely poor coupling between the cells ($0.1\,\mathrm{nS/m}$), far from the physiologic condition.

The uncoupled condition shows again a duration of the cycle longer than the nominal case: CL = 856 ± 306 ms, meaning that slow cells are still beating.

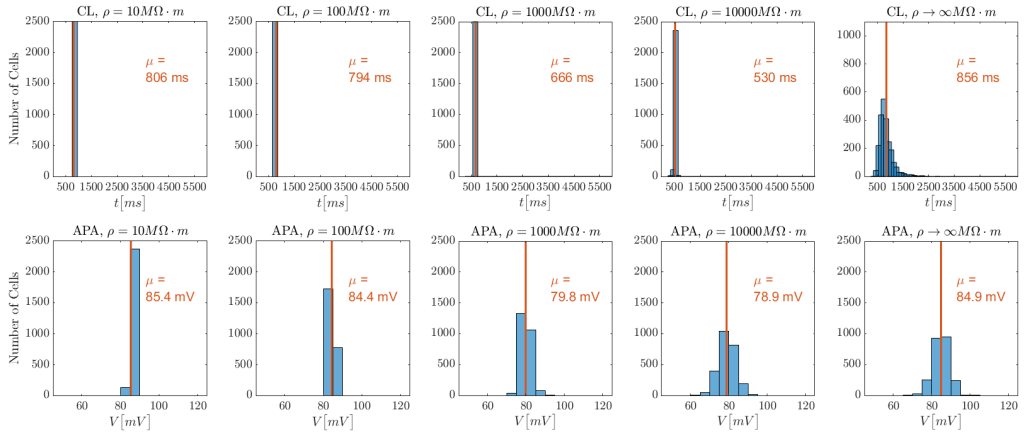

Figure 4.28: Histograms for 2D WT condition with $\sigma = 0.1873$: CL (top, bin width = 100 ms) and APA (bottom, bin width = 5 mV) at different gap junctions coupling ($\rho = 10, 100, 1000, 10000$ and $\to \infty$ $\mathrm{M\Omega \cdot m}$ from left to right). Vertical orange lines represent the mean value of the distributions, whose value is displayed on the right.

$\sigma = 0.3$

In this condition, cells do not reach a good synchronization for high coupling resistivities anymore: CL = 502 $\pm$ 70 ms for $\rho = 10000\ \mathrm{M\Omega \cdot m}$. With more physiological couplings, cells manage to beat at the same frequency: CL = 795 $\pm$ 1 ms ($\rho = 10\ \mathrm{M\Omega \cdot m}$), CL = 762 $\pm$ 1 ms ($\rho = 100\ \mathrm{M\Omega \cdot m}$) and CL = 513 $\pm$ 1 ms ($\rho = 10\ \mathrm{M\Omega \cdot m}$). This values show, as supposed in the previous section, that simulating a tissue with 2D connections between cells provides CLs more similar to the nominal value, opposed to what happened in 1D (where there were fewer links between different cells and therefore the role of fast-pacing cells was stronger). This is not true for $\rho = 10000\ \mathrm{M\Omega \cdot m}$, as will be discussed at the end of this section. Finally, CL is 828 $\pm$ 368 ms if the cells are uncoupled.

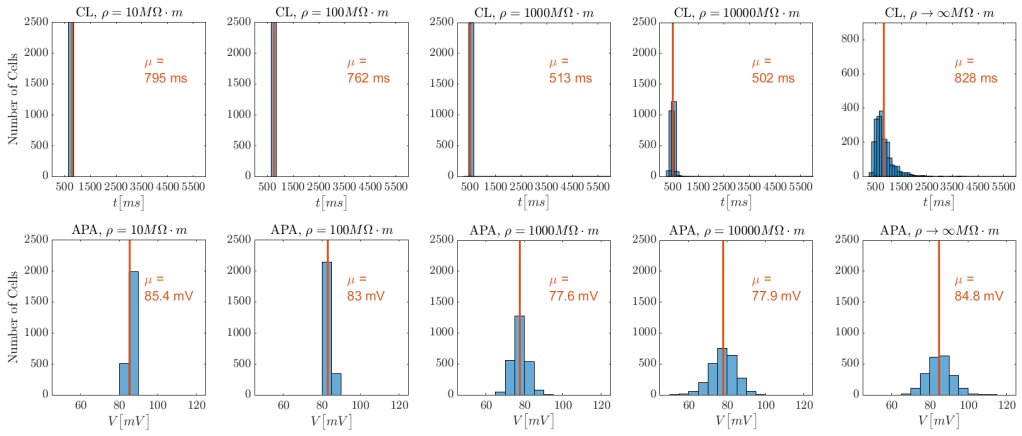

Figure 4.29: Histograms for 2D WT condition with $\sigma = 0.3$: CL (top, bin width = 100 ms) and APA (bottom, bin width = 5 mV) at different gap junctions coupling ($\rho = 10, 100, 1000, 10000$ and $\to \infty\ \mathrm{M\Omega \cdot m}$ from left to right). Vertical orange lines represent the mean value of the distributions, whose value is displayed on the right.

$\sigma = 0.4$

The maximum variability in the input variables of the model leads to a very spread distribution in the pacing frequency of the cells. Uncoupled cells have indeed a mean CL of 773 $\pm$ 425 ms, where the fastest cell has a CL of 247 ms and the slowest one of 6259 ms (in Figure 4.31 are showed the trends of their action potentials). This wide range of values is not reduced in the case of poor couplings even if the mean frequency rises (CL = 493 $\pm$ 174 ms with $\rho = 10000\ \mathrm{M\Omega \cdot m}$), whereas for lower resistivities a perfect synchronization is still achieved, even if at higher frequencies. Indeed, with $\rho = 10\ \mathrm{M\Omega \cdot m}$ CL is 784 $\pm$ 1 ms, for $\rho = 100\ \mathrm{M\Omega \cdot m}$ CL is 718 $\pm$ 1 ms and for $\rho = 1000\ \mathrm{M\Omega \cdot m}$ CL is 427 $\pm$ 1 ms.

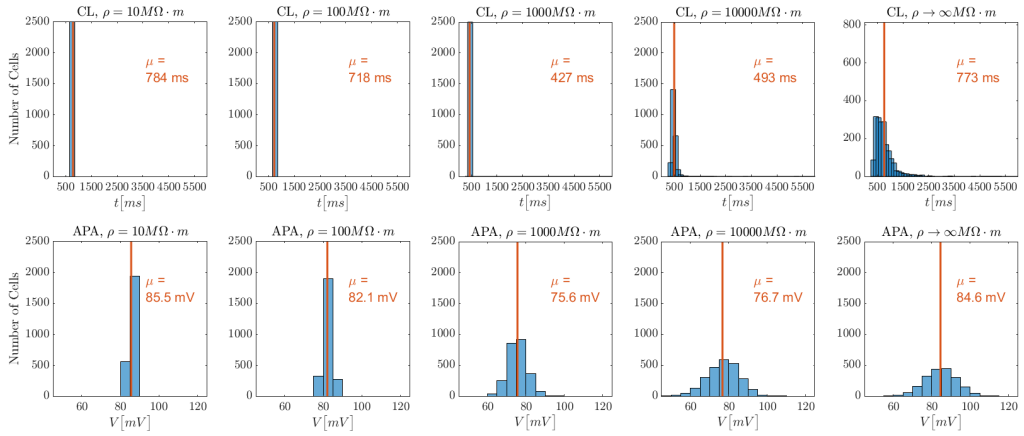

Figure 4.30: Histograms for 2D WT condition with $\sigma = 0.4$: CL (top, bin width = 100 ms) and APA (bottom, bin width = 5 mV) at different gap junctions coupling ($\rho = 10, 100, 1000, 10000$ and $\to \infty$ MΩ · m from left to right). Vertical orange lines represent the mean value of the distributions, whose value is displayed on the right.

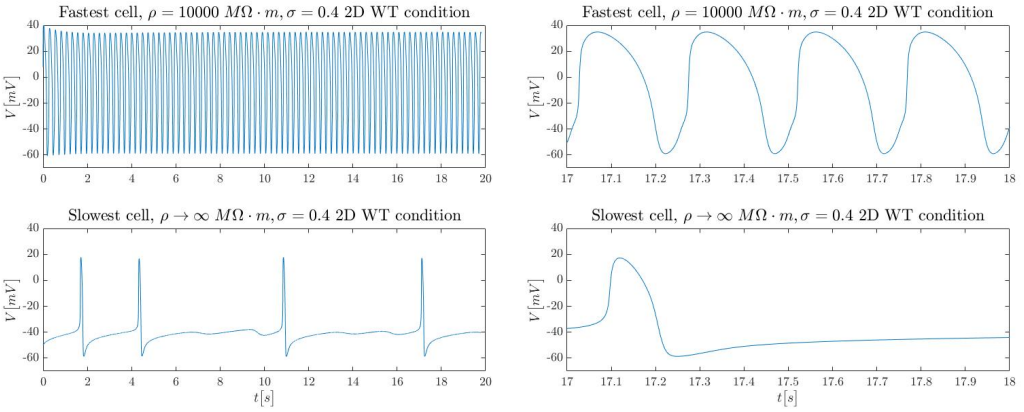

(a) *(b)*

Figure 4.31: Comparison between the fastest (top) and slowest (bottom) cells with $\sigma = 0.4$ for the uncoupled 2D WT condition. (a) activity for the entire 20 s of the simulation. (b) zoom on 1 s of activity. In this plot it can be seen that the fastest cell has a negligible diastolic depolarization phase (< 100 ms), whereas the slowest one has a remarkably long one (∼ 6 s). Nevertheless, it is notable that the AP is longer (> 200 ms) in the fastest cell, meaning that in this case repolarizing currents are particularly weak with respect to the depolarizing ones, as also the OS values highlight (almost +40 mV).

4.2.3 2D WT Model Results at a glance

Figures 4.32 and 4.33 sum up the results of the 2D wild type condition. High coupling resistivities ($\rho = 10000$ and $\rho \to \infty$ MΩ · m) prevent cells from synchro-

nizing; on the opposite, with $\rho \leq 1000\ \mathrm{M\Omega \cdot m}$ cells manage to beat at the same frequency, even if with $\rho = 1000\ \mathrm{M\Omega \cdot m}$ this is only possible with very short CLs because of the effect of fast-pacing cells (Figure 4.32a). APA has similar trends, but with a higher dispersion even with good cellular couplings, reflecting a bigger difficulty for the cells to homogenize this feature (Figure 4.32b).

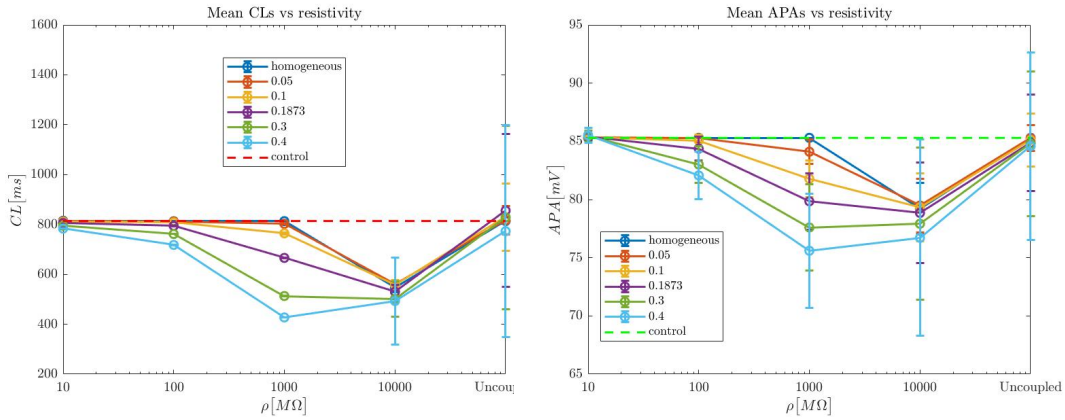

(a) (b)

Figure 4.32: Trends of CL and APA (± standard deviation) with respect to resistivity for different levels of cellular heterogeneity ($\sigma = 0.05, 0.1, 0.1873, 0.3$ and 0.4) and nominal values (CL = 814 ms, APA = 85.3 mV, dashed lines); 2D WT condition.

Regarding the trends of the CL with respect to heterogeneity, two results are worth of mention (Figure 4.33a). The first one is that for uncoupled cell, CL is longer than the nominal value for $\sigma = 0.1, 0.1873$ and 0.3, meaning that with these distributions of parameters, there are many slow-pacing cells that contribute to stretch the duration of the mean CL. The second noteworthy result is that with $\rho = 10000\ \mathrm{M\Omega \cdot m}$, CL tends to be very short at low σ and even with homogeneous cells. This is probably due to the particular random initial condition and the particular distribution of parameters with which the simulation started. Furthermore, this case does not have the same trend as $\rho = 1000\ \mathrm{M\Omega \cdot m}$, because of the effect of "saturation" that a poor coupling has on the shortening of the CL: starting from an already short CL, increasing σ does not provide a faster pacing. This is also true for the APA, in which the purple curve in Figure 4.33b starts from a value clearly detached from that of the curves representing the other ρ. In the same graph it is possible to asses that even with $\rho = 10\ \mathrm{M\Omega \cdot m}$, cells do not show the same amplitude of the action potential.

The principal aspect to note for this 2D WT case, is the stretching of the CL with respect to the 1D case (apart from the $\rho = 10000\ \mathrm{M\Omega \cdot m}$ case). In particular, for physiological levels of gap junction couplings ($\rho = 10/100\ \mathrm{M\Omega \cdot m}$, purple

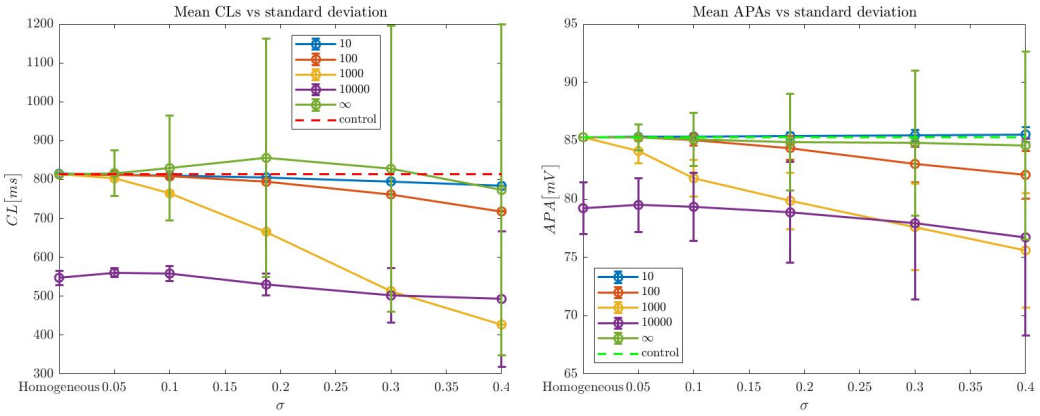

(a) *(b)*

Figure 4.33: Trends of CL and APA (± standard deviation) with respect to standard deviation for different values of gap junctions resistivity ($\rho = 10, 100, 1000, 10000$ and $\to \infty$ MΩ · m) and nominal values (CL = 814 ms, APA = 85.3 mV, dashed lines); 2D WT condition.

trace in 4.32a) and variability of the parameters ($\sigma = 0.1873$), CL is much more similar ($\sim$ 800 ms) to the nominal value (814 ms), with respect to the 1D case ($\sim$ 700 ms).

4.2.4 2D Double Mutant condition

As in the 1D case, the modal values of the uncoupled CL distributions differ from the nominal value of 814 ms (Figure, 4.34) because of the effect of the mutations. The mean CL for uncoupled homogeneous cells is still 1019 ms, as it is just the 2D extension of the 0D and 1D model. Being there more cells now, the distributions appear wider and smoother.

Next paragraphs will show the results for different degrees of heterogeneity and cellular couplings.

Homogeneous cells ($\sigma = 0$)

As in the wild type condition, the case with $\rho = 10000$ MΩ · m presents a short CL with a quite high dispersion for a homogeneous condition: CL = 640 ± 17 ms. With all the other couplings instead, CL is 1019 ± 1 ms: as usual, synchronization is easily reached with this settings. In addition, mean CL for the uncoupled set up is 1019 ms, as one would expect (Figure 4.35).

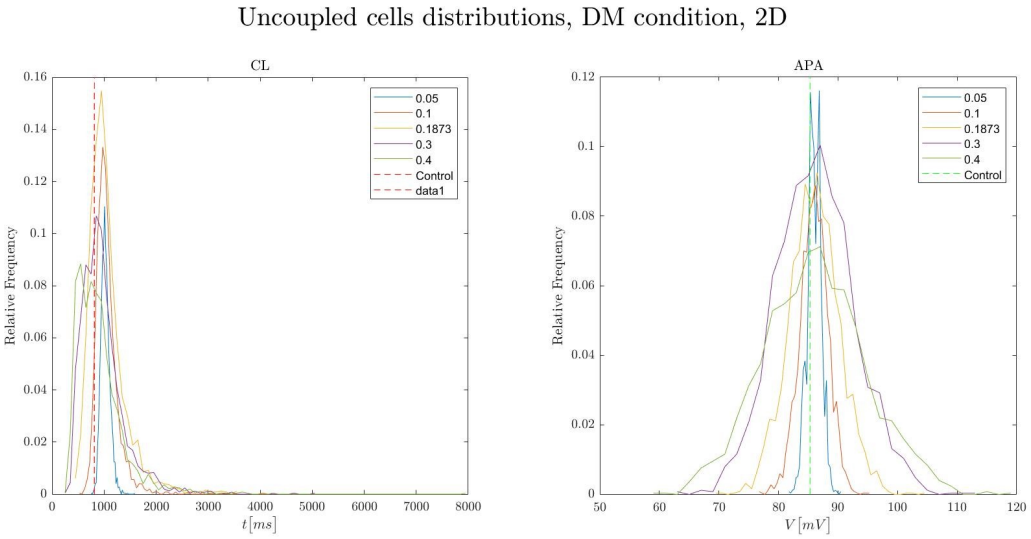

Figure 4.34: CL (left) and APA (right) distributions for uncoupled cells for different values of standard deviation ($\sigma = 0.05, 0.1, 0.1873, 0.3, 0.4$) and nominal values (CL = 814 ms, APA = 85.3 mV, dashed lines); 2D DM condition. Vertical orange lines represent the mean value of the distributions, whose value is displayed on the right.

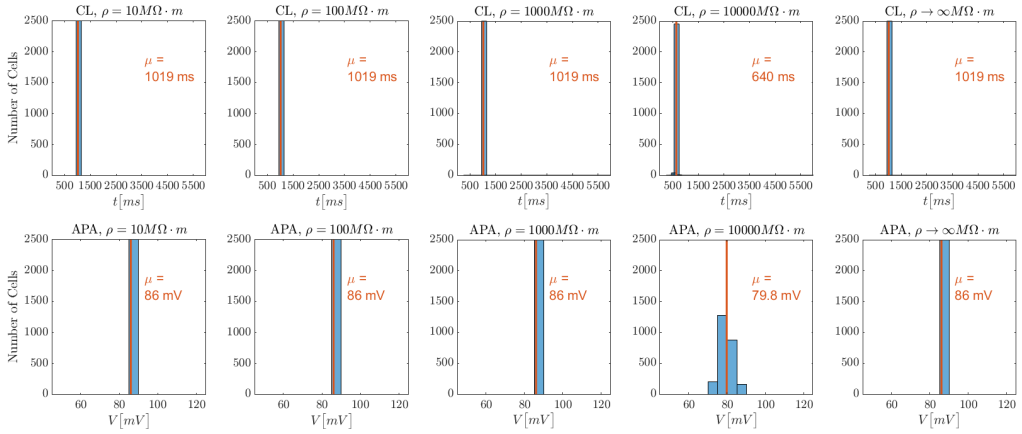

Figure 4.35: Histograms for 2D DM homogeneous condition: CL (top, bin width = 100 ms) and APA (bottom, bin width = 5 mV) at different gap junctions coupling ($\rho = 10, 100, 1000, 10000$ and $\rightarrow \infty$ MΩ · m from left to right).

$\sigma = 0.05$

Frequency is minimally increased: CL = 1017 ± 1 ms ($\rho = 10$ MΩ · m), CL = 1017 ± 1 ms ($\rho = 100$ MΩ · m), CL = 1005 ± 1 ms ($\rho = 10$ MΩ · m), CL = 636 ± 24 ms ($\rho = 10$ MΩ · m). With respect to the previous condition, for $\sigma = 0.05$ the uncoupled cell condition shows a spread distribution: CL = 1025 ± 86 ms

(Figure 4.36). Once again, the mean value is bigger than the nominal one, for the contribution of slow-pacing cells.

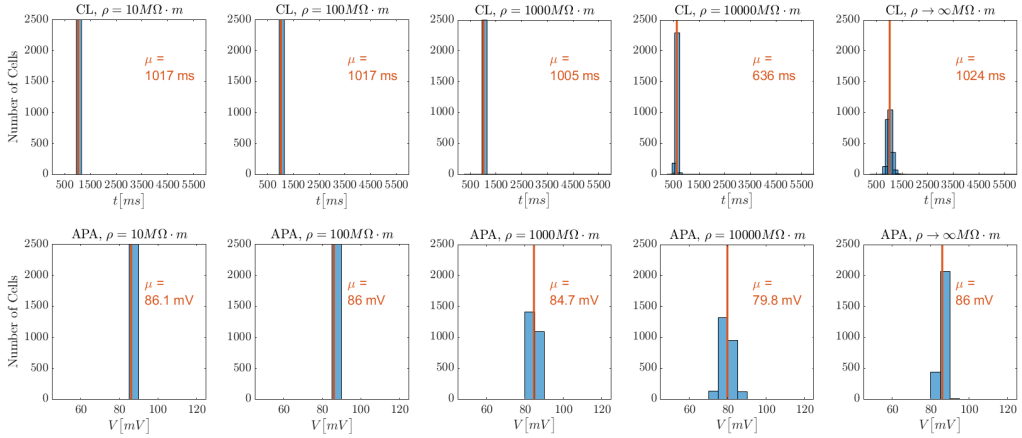

Figure 4.36: Histograms for 2D DM condition with $\sigma = 0.05$: CL (top, bin width = 100 ms) and APA (bottom, bin width = 5 mV) at different gap junctions coupling ($\rho = 10, 100, 1000, 10000$ and $\to \infty$ $M\Omega \cdot m$ from left to right). Vertical orange lines represent the mean value of the distributions, whose value is displayed on the right.

$\sigma = 0.1$

The behavior of the 2D tissue for $\sigma = 0.1$ is consistent with the results obtained with $\sigma = 0.05$ (CL = 1014 $\pm$ 1 ms with $\rho = 10$ $M\Omega \cdot m$; CL = 1012 $\pm$ 1 ms with $\rho = 100$ $M\Omega \cdot m$), only emphasized for $\rho = 1000$ $M\Omega \cdot m$ in terms of cycle duration: CL = 954 $\pm$ 2 ms. For $\rho = 10000$ $M\Omega \cdot m$ the obtained mean CL is 626 ms, with a standard deviation of 37 ms, whereas uncoupled cells have a CL of 1050 $\pm$ 216 ms (Figure 4.37).

$\sigma = 0.1873$

With the degree of heterogeneity consistent with physiological conditions, the effect of the mutation is minimally compensated with low resistivities (i.e. good couplings, which are also the most similar to the physiologic ones that have been simulated): for $\rho = 10$ $M\Omega \cdot m$ the resulting CL is 1009 $\pm$ 1 ms and for $\rho = 100$ $M\Omega \cdot m$ CL is 997 $\pm$ 1 ms. A more physiological cycle length is obtained with a worse coupling: CL = 838 $\pm$ 1 ms with $\rho = 1000$ $M\Omega \cdot m$, which anyway represents a quite poor cellular coupling relying on the values reported in literature (corresponding to 1 nS, it is at the lower boundary of the interval reported by Inada et al. [14] for the rabbit SAN). This means that even if the simulations

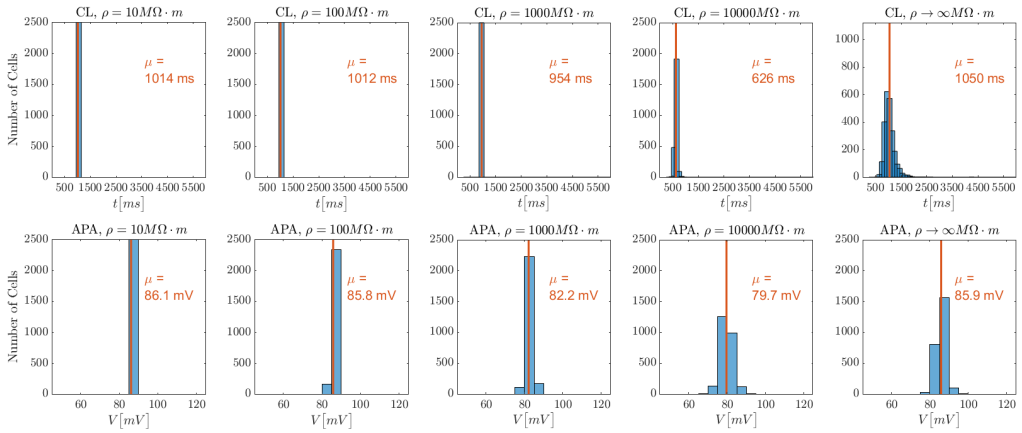

Figure 4.37: Histograms for 2D DM condition with $\sigma = 0.1$*: CL (top, bin width = 100 ms) and APA (bottom, bin width = 5 mV) at different gap junctions coupling (*$\rho = 10, 100, 1000, 10000$ *and* $\to \infty$ $\mathrm{M\Omega \cdot m}$ *from left to right). Vertical orange lines represent the mean value of the distributions, whose value is displayed on the right.*

give a good result, it is unlike to find the same behaviour in a real SAN. Moreover, further increasing the resistivity leads to higher frequencies: CL is 601 $\pm$ 46 ms with $\rho = 10000$ $\mathrm{M\Omega \cdot m}$, a gap junction coupling that again does not allow the cells to synchronize. The mean CL (1056 $\pm$ 379 ms) is still longer than the nominal mutated value if the cells are not linked together, meaning that - with this parameters settings - there still are slow-pacing cells beating (Figure 4.38).

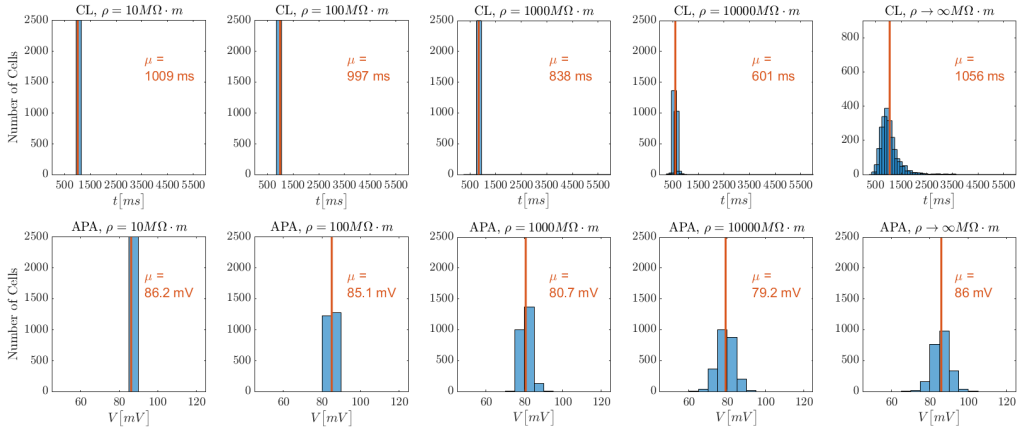

Figure 4.38: Histograms for 2D DM condition with $\sigma = 0.1873$*: CL (top, bin width = 100 ms) and APA (bottom, bin width = 5 mV) at different gap junctions coupling (*$\rho = 10, 100, 1000, 10000$ *and* $\to \infty$ $\mathrm{M\Omega \cdot m}$ *from left to right). Vertical orange lines represent the mean value of the distributions, whose value is displayed on the right.*

$\sigma = 0.3$

Contrarily to the previous case, the mean CL of the uncoupled cells is less than the mutated single-cell one: 973 $\pm$ 429 ms with respect to 1019 ms, meaning that some slow-pacing cell is no more excitable with this parameters setting. Anyway, cells with very long CL are still present: CL_{max} is indeed 5017 ms. Synchronization is achieved for $\rho < 1000$ M$\Omega \cdot$m: CL = 998 $\pm$ 1 ms ($\rho = 10$ M$\Omega \cdot$m), CL = 958 $\pm$ 1 ms ($\rho = 10$ M$\Omega \cdot$m) and CL = 629 $\pm$ 1 ms ($\rho = 10$ M$\Omega \cdot$m). As usual, $\rho = 10000$ M$\Omega \cdot$m prevents cells from beating with the same pace even if this greatly increases: CL = 571 $\pm$ 100 ms (Figure 4.39).

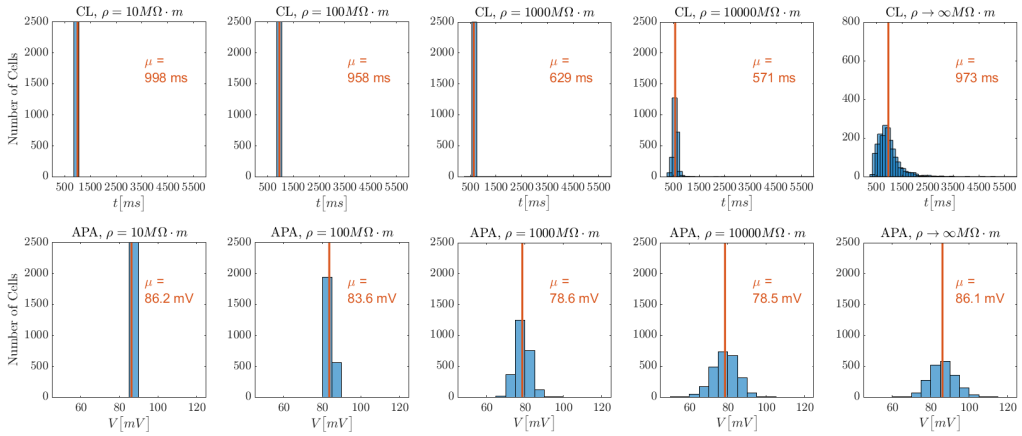

Figure 4.39: Histograms for 2D DM condition with $\sigma = 0.3$: CL (top, bin width = 100 ms) and APA (bottom, bin width = 5 mV) at different gap junctions coupling ($\rho = 10, 100, 1000, 10000$ and $\to \infty$ M$\Omega \cdot$m from left to right). Vertical orange lines represent the mean value of the distributions, whose value is displayed on the right.

$\sigma = 0.4$

In this case the uncoupled condition has a shorter CL than the previous case: CL = 905 $\pm$ 483 ms; nevertheless there are cells with an incredibly low frequency: CL_{max} is up to 7920 ms for the cell in position [9,9] (Figure 4.41). The coupling with $\rho = 10000$ M$\Omega \cdot$m only allows a partial synchronization, thus cells with a long CL do not undergo the influence of fast-pacing cells and are therefore still present ($CL_{max} = 6976$ ms); despite of the presence of very slow cells the mean CL is almost half the nominal mutated value: 568 $\pm$ 319 ms. The x axes of the $\rho = 10000$ and $\to \infty$ M$\Omega \cdot$m subplots were stretched in order to visualize the bins of this very long CLs. Lower coupling resistivities guarantee a complete synchronization instead (Figure 4.40): CL = 985 $\pm$ 1 ms ($\rho = 10$ M$\Omega \cdot$m), CL = 906 $\pm$ 1 ms ($\rho = 100$ M$\Omega \cdot$m), CL = 470 $\pm$ 1 ms ($\rho = 1000$ M$\Omega \cdot$m).

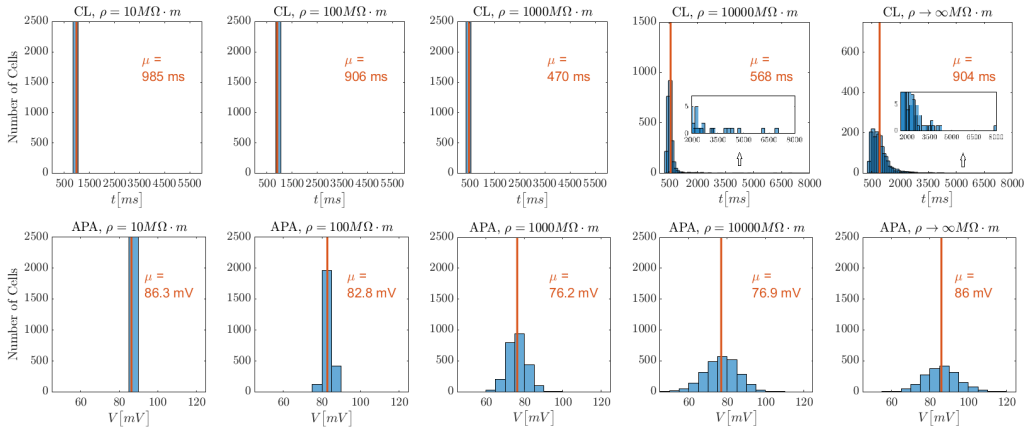

Figure 4.40: Histograms for 2D DM condition with $\sigma = 0.4$: CL (top, bin width = 100 ms) and APA (bottom, bin width = 5 mV) at different gap junctions coupling ($\rho = 10, 100, 1000, 10000$ and $\to \infty$ MΩ · m from left to right). Vertical orange lines represent the mean value of the distributions, whose value is displayed on the right.

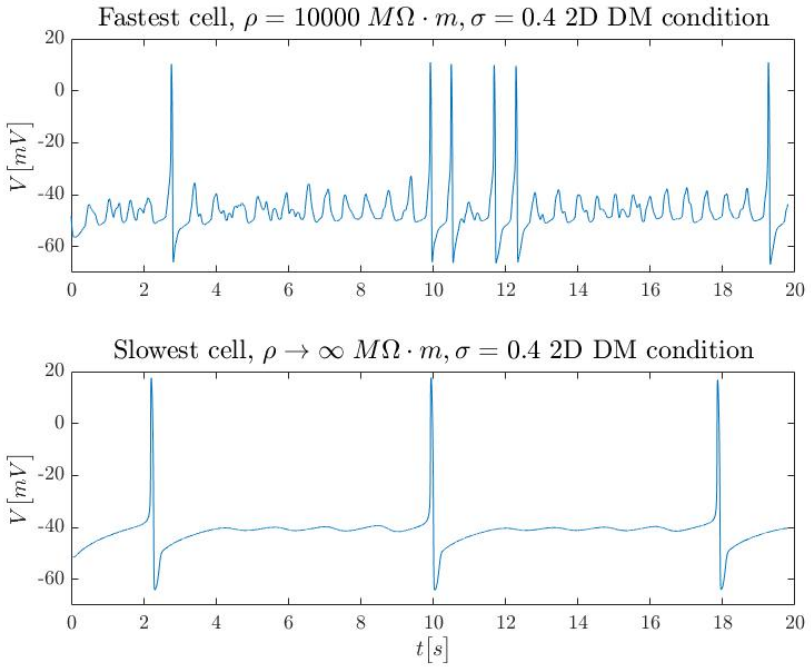

Figure 4.41: Action potential over the 20 s of simulation for the slowest cells with $\rho =$ 10000 MΩ · m (top) and $\rho \to \infty$ MΩ · m (bottom), $\sigma = 0.4$ 2D DM condition.

4.2.5 2D DM Model Results at a glance

The previous results are summarized in Figures 4.42 and 4.43. The first shows how the mutations affect the mean CL of the 2D model (Figure 4.43a): at low re-

sistivities it can be seen that the slowdown in frequency due to the I_f loss of function is not recovered, being the curve above the red dashed line. On the contrary, unlikely cellular couplings and standard deviations of the ionic conductances provide an excessive increase of frequency. As usual, poor cellular couplings do not allow the cells to synchronize their pacing frequency, resulting in a high dispersion of this feature. As the WT case, APA has a trend similar to CL, only with a higher dispersion (as can be appreciated in Figure 4.43b).

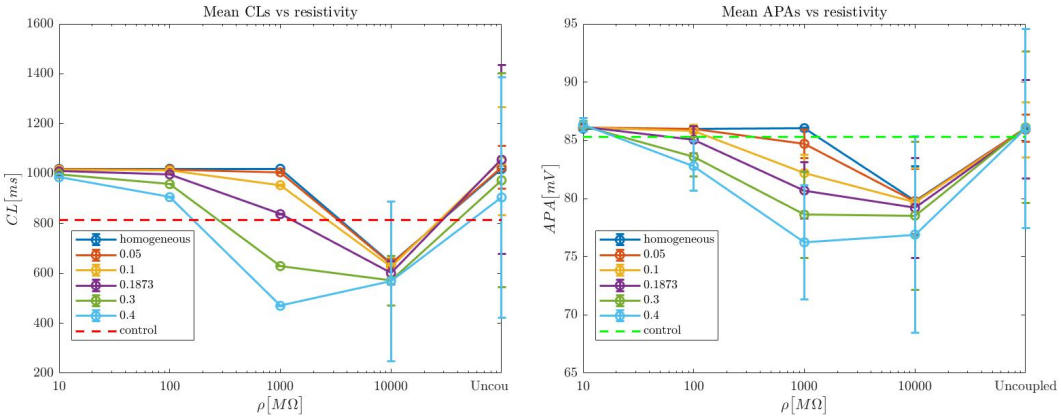

(a) *(b)*

Figure 4.42: Trends of CL and APA ($\pm$ standard deviation) with respect to resistivity for different levels of cellular heterogeneity ($\sigma = 0.05, 0.1, 0.1873, 0.3$ and 0.4) and nominal values (CL = 814 ms, APA = 85.3 mV, dashed lines); 2D DM condition.

About the effect of σ in the input parameters, the degree of heterogeneity mainly affects the ability of the cells to synchronize: the larger the dispersion of the conductances is, the larger the one of the features (CL and APA). In addition, at the increase of σ, the mean pacing frequency tends to increase.

Another aspect of the mutations is the increase in the number of non-excitable cells present in the model: 578 (23.1%) do not beat in the 2D WT condition, with respect to the 709 (28.4%) of the double mutated case (bot with $\rho \to \infty$ M$\Omega \cdot$m and $\sigma = 0.4$). Nevertheless, even if with very poor couplings, almost every cell starts beating again, as it is shown in Figure 4.44.

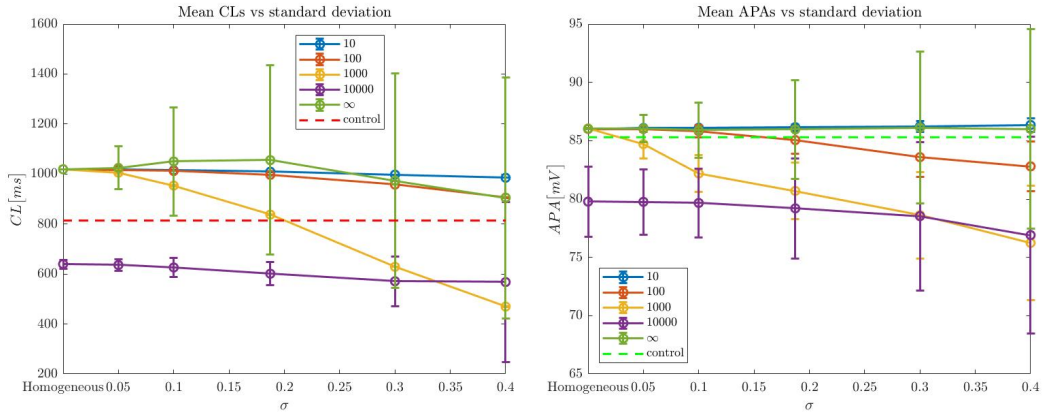

(a) *(b)*

Figure 4.43: Trends of CL and APA (± standard deviation) with respect to standard deviation for different values of gap junctions resistivity ($\rho = 10, 100, 1000, 10000$ and $\rightarrow \infty$ MΩ · m) and nominal values (CL = 814 ms, APA = 85.3 mV, dashed lines); 2D WT condition.

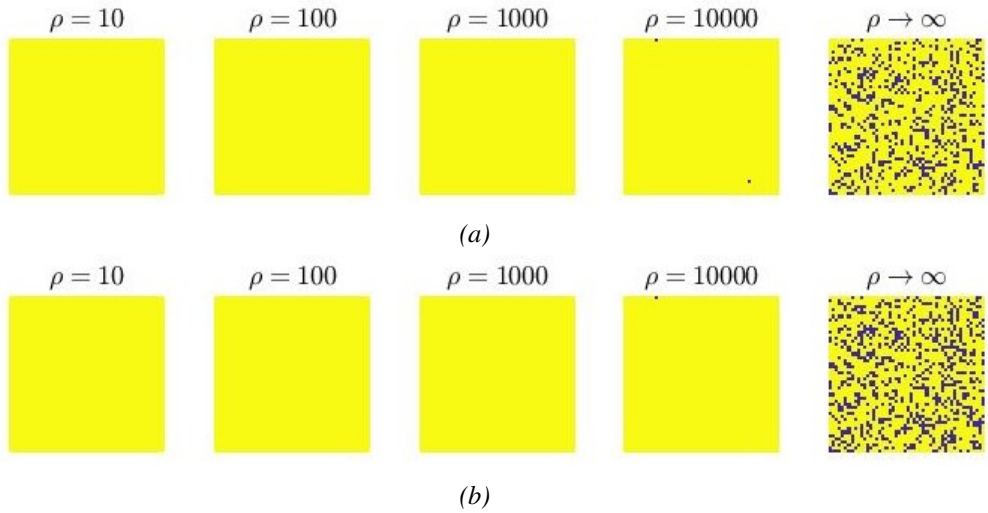

(a)

(b)

Figure 4.44: Color maps of the 2D models: the color blue represents the cells that do not show action potentials, yellow represent cells with electrical activity. (a) Comparison between the color maps of 2D WT condition, $\sigma = 0.4$, at different gap junction couplings. For $\rho \rightarrow \infty$ MΩ · m 576 cells (23.0%) are not beating. (b) Comparison between the color maps of 2D DM condition, $\sigma = 0.4$, at different gap junction couplings. For $\rho \rightarrow \infty$ MΩ · m 708 cells (28.3%) are not beating.

Figure 4.45 displays instead the effect of heterogeneity on the ability of the cells to show an AP.

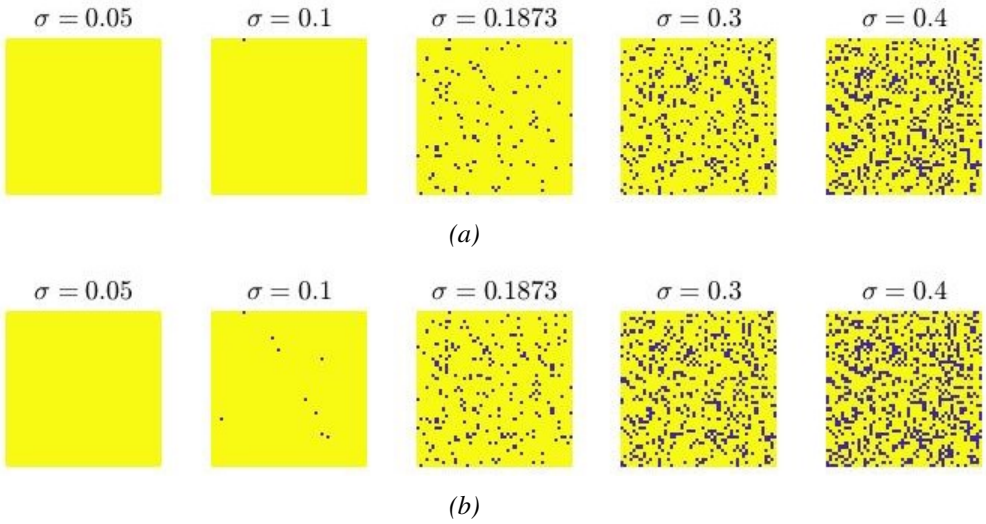

Figure 4.45: Color maps of the 2D models ($\rho \to \infty\,\mathrm{M\Omega \cdot m}$): the color blue represents the cells that do not show action potentials, yellow represents cells with electrical activity. With the increase of cellular heterogeneity, the number of non-excitable cells grows. (a) 2D WT Condition: 0 for $\sigma = 0.05$; 1 (0.04 %) for $\sigma = 0.1$; 98 (3.9 %) for $\sigma = 0.1873$; 351 (14.0 %) for $\sigma = 0.3$; 576 (23.0 %) for $\sigma = 0.4$; (b) 2D DM Condition: 0 for $\sigma = 0.05$; 9 (0.36 %) for $\sigma = 0.1$; 209 (8.4 %) for $\sigma = 0.1873$; 513 (20.5 %) for $\sigma = 0.3$; 708 (28.3 %) for $\sigma = 0.4$.

Finally, Tables 4.6 and 4.7 summarize all the results obtained with the simulations in terms of frequency (in bpm). As already noted while speaking of cycle lengths, some combination of cellular couplings and heterogeneities provide unrealistic pacings in 1D and also in 2D, even if to a lesser extent in the latter case. For example, $\rho = 1000\,\mathrm{M\Omega \cdot m}$ together with $\sigma = 0.3$ or 0.4 provides mean pacing frequencies of 142 and 162 bpm in 1D respectively, values that slightly decrease in 2D: 117 and 140 bpm. For lower coupling resistivities, namely more physiologic gap junctions conductances, beating rates more similar to the nominal value are obtained (73.7 bpm), especially in 2D: from 73.8 ($\sigma = 0.05$, + 0.1%) to 76.6 ($\sigma = 0.4$, + 3.9%).

	$\rho\,[\mathrm{M\Omega \cdot m}]$				
σ	**10**	**100**	**1000**	**10000**	∞
Homogeneous cells	73.7 (+ 0%) 58.9 (- 20.1%)	73.8 (+ 0.1%) 58.9 (- 20.1%)	73.7 (+ 0%) 58.9 (- 20.1%)	74.4 (+ 0.9%) 59.4 (- 19.4%)	73.7 (+ 0%) 58.9 (- 20.1%)
0.05	75.1 (+ 1.9%) 60.1 (- 19.5%)	76.6 (+ 3.9%) 61.4 (- 16.7%)	77.9 (+ 5.7%) 62.1 (- 15.7%)	82.5 (+ 11.9%) 66.6 (- 9.6%)	74 (+ 0.4%) 59 (- 29.9%)
0.1	77.6 (+ 5.3%) 62 (- 15.9%)	80.4 (+ 9.1%) 64.6 (- 12.3%)	85.2 (+ 15.6%) 69.9 (- 5.2%)	96.1 (+ 30.4%) 79.4 (+ 7.7%)	73.2 (- 0.7%) 57.4 (- 22.1%)
0.1873	83 (+ 12.6%) 66.4 (- 9.9%)	88.1 (+ 19.5%) 71 (- 3.7%)	110.4 (+ 49.8%) 90.7 (+ 23.1%)	103.3 (+ 40.2%) 87.1 (+ 18.2%)	74.3 (+ 0.8%) 57.7 (- 21.7%)
0.3	91.9 (+ 24.7%) 73.7 (+ 0%)	101.9 (+ 38.3%) 82.9 (+ 12.5%)	142.3 (+ 93.1%) 131.2 (+ 78%)	105.2 (+ 42.7%) 93.1 (+ 26.3%)	76 (+ 3.1%) 66.2 (- 10.2%)
0.4	100.6 (+ 36.5%) 81 (+ 9.9%)	115.7 (+ 57%) 96.9 (+ 31.5%)	162.2 (+ 120.1%) 156.4 (+ 112.2%)	103.1 (+ 39.9%) 90.6 (+ 22.9%)	82 (+ 11.3%) 75.7 (+ 2.7%)

Table 4.6: Mean frequency results for 1D WT (black) and 1D DM (grey) condition and relative percentage variation with respect to the control value: 73.7 bpm (corresponding to a CL of 814 ms).

	$\rho\,[\mathrm{M\Omega \cdot m}]$				
σ	**10**	**100**	**1000**	**10000**	∞
Homogeneous cells	73.6 (- 0.1%) 58.9 (- 20.1%)	73.8 (+ 0.1%) 58.9 (- 20.1%)	73.8 (+ 0.1%) 58.9 (- 20.1%)	109.6 (+ 48.7%) 93.8 (+ 27.3%)	73.7 (+ 0%) 58.9 (- 20.1%)
0.05	73.8 (+ 0.1%) 59 (- 19.9%)	73.9 (+ 0.3%) 59 (- 19.9%)	74.8 (+ 1.5%) 59.7 (- 19%)	107.1 (+ 45.3%) 94.4 (+ 28.1%)	73.5 (- 0.3%) 58.6 (- 20.5%)
0.1	74 (+ 0.4%) 59.1 (- 19.8%)	74.3 (+ 0.8%) 59.3 (- 19.5%)	78.5 (+ 6.5%) 62.9 (- 14.7%)	107.4 (+ 45.7%) 95.8 (+ 30%)	72.3 (- 1.9%) 57.1 (- 22.5%)
0.1873	74.5 (+ 1.1%) 59.5 (- 19.3%)	75.6 (+ 2.6%) 60.2 (- 18.3%)	90.1 (+ 22.3%) 71.6 (- 2.8%)	113.2 (+ 53.6%) 99.8 (+ 35.4%)	70.1 (-4.9%) 56.8 (- 22.9%)
0.3	75.5 (+ 2.4%) 60.1 (-18.5%)	78.8 (+ 6.9%) 62.7 (-14.9%)	116.9 (+ 58.6%) 95.4 (+ 29.4%)	119.6 (+ 62.3%) 105.1 (+ 42.6%)	72.5 (- 1.6%) 61.7 (- 16.3%)
0.4	76.6 (+ 3.9%) 60.9 (- 17.4%)	83.6(+ 13.4%) 66.3 (- 10%)	140.4 (+ 90.5%) 127.7 (73.3%)	121.7 (+ 65.1%) 105.6 (+ 43.3%)	77.6 (+ 5.3%) 66.3 (- 10%)

Table 4.7: Mean frequency results for 2D WT (black) and 2D DM (grey) condition and relative percentage variation with respect to the control value: 73.7 bpm (corresponding to a CL of 814 ms).

This indicates that fast pacing cells have the ability to drive the other ones, but only with medium-high resistivities ($\rho = 1000/10000\,\mathrm{M\Omega \cdot m}$): on one hand, medium-high ρ allow them not to be inhibited by the neighbouring slower cells; on the other hand, they let enough current flow and stimulate the slow-pacing cells. Probably in 3D, where fast-pacing cells would be surrounded by more normal-pacing ones, mean frequency would be more similar to the nominal value also for $\rho = 1000\mathrm{M\Omega \cdot m}$, since these cells would constitute a much bigger load for the fast ones and therefore would slow them down in a more relevant way. Another hypothesis could be that, to account for the higher frequency that was obtained in these models, the human SAN has a lower degree of heterogeneity than the rabbit one ($\sigma = 0.1873$). However, this is unrealistic since this feature represents a factor of robustness for biological systems in general, and the human heart is probably more reliable than the rabbit one. Nevertheless, no data about human SAN are available, thus this last statement remains only an hypothesis.

4.2.6 Simulations with tuned parameters

The previous results were also used as a sensitivity analysis to forecast what values of ρ (gap junction couplings) and σ (cellular heterogeneity) provide physiologic pacing frequencies. A standard deviation in the cellular parameters of 0.1873 was chosen for it represents the level of heterogeneity found in the rabbit SAN [39]. In multidimensional models, an important parameter is the conduction velocity (CV, in cm/s). Thus, for ρ it was selected a value that also allows to obtain a physiologic CV (i.e. in the range reported in literature for the SAN, section 1.1). About 10 cm/s were considered, since the measures from Csepe et al. [5] seemed more reliable than the generic values reported in the other cited works ([15], [16]). In the 2D case, $\rho = 100\,\mathrm{M\Omega \cdot m}$ was set (10 nS), since this value provided physiological values of CV: 10.8 cm/s on the x axis and 12.1 cm/s on y for the WT condition, 10.3 cm/s on x and 11.1 cm/s on y in case of double mutation. For the 1D model, the resistivity had to be lowered to $50\,\mathrm{M\Omega \cdot m}$ (corresponding to 20 nS) in order to get similar values of CV: 12.8 cm/s and 12.2 cm/s for WT and DM conditions respectively. A lower ρ was necessary since in 1D there are less connections that lower the total resistivity, as resistors in parallel do.

In all these configurations, a complete synchronization was achieved: CL = 609 ± 1 ms for 1D WT, CL = 928 ± 1 ms for 1D DM, CL = 794 ± 1 ms for 2D WT and CL = 997 ± 1 ms for 2D DM. Figure 4.46 shows how these results were obtained.

From these results (summarized in Table 4.8) it can be noticed that the mutations seem not to affect the conduction velocity, even if a single result has no statistical relevance. Moreover, in case of mutation, the cells manage in any case to reach a common frequency, but lower than the wild type condition. It must

	1D		2D	
CV [cm/s]	**WT**	**DM**	**WT**	**DM**
x	12.8	12.2	10.8	10.3
y			12.1	11.1

Table 4.8: Results for Conduction Velocity (in cm/s). In all the simulations $\sigma = 0.1873$ *was set, whereas* ρ *was 50* $\mathrm{M}\Omega \cdot \mathrm{m}$ *in 1D and 100* $\mathrm{M}\Omega \cdot \mathrm{m}$*, in 2D, for which case CV was computed on both x and y directions (Figure 4.46).*

be highlighted that "same frequency" does not mean that the cells have the same potential at the same time, but only that they have the same cycle length. Indeed, they can be out of phase, and this is the reason why a propagation can be seen in the 1D and 2D models. This is a condition halfway through a too high cellular coupling ($R \to 0$), where cells have the same potential at the same time and no propagation can be assessed ($CV \to \infty$), and a too low one ($R \to \infty$) in which case the propagation no longer exists ($CV \to 0$).

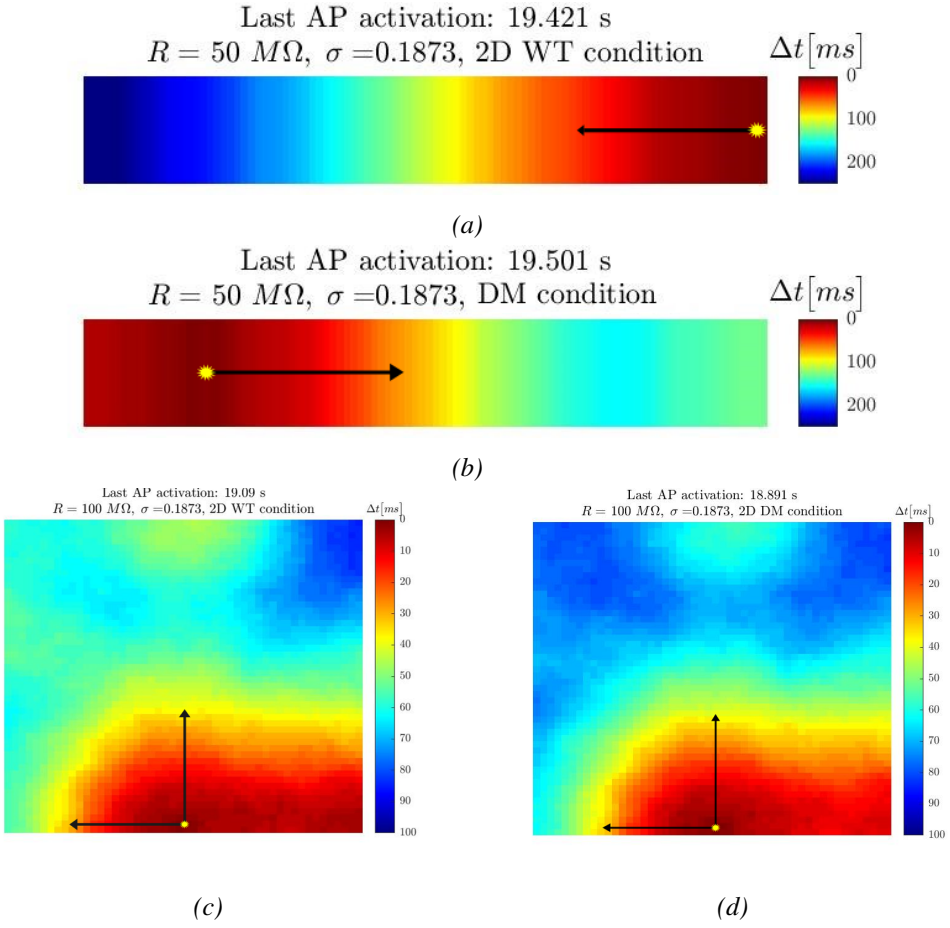

Figure 4.46: Activation maps of SAN tissue: time differences (in ms) for different cells to reach the same potentials (0 mV); dark red represent the earliest activation zones of the last AP, used as a reference to compute CV. The yellow star is the breakthrough point; black arrows indicates the direction on which CV was computed. In all the simulations $\sigma = 0.1873$ *was set, whereas* ρ *was 50* $\mathrm{M\Omega \cdot m}$ *in 1D and 100* $\mathrm{M\Omega \cdot m}$ *in 2D. (a) Propagation through a 1D fiber of the SAN, WT condition. (b) Propagation through a 1D fiber of the SAN, DM condition. (c) Propagation through a 2D fiber of the SAN, WT condition (x and y velocities were computed). (d) Propagation through a 2D fiber of the SAN, DM condition (x and y velocities were computed).*

Chapter 5

Conclusions

This thesis aimed to test the effects of the I479V/A485E Double Mutation affecting the HCN4 channel isoform reported by Servatius, Porro et al. [10] on a human sinoatrial computational model at many levels: HCN4 channel, single SAN cell (0D), SAN fiber (1D) and SAN tissue (2D). The patient presented in the study showed many symptoms, among which there was the bradycardia. As it is known from literature, the HCN channels are responsible for the I_f current, which is a key player in the onset of the action potential of the autorhythmic cells in the sinoatrial node. This anatomical structure governs indeed the rhythm of the heart under physiological conditions. This work tried to link the effect (bradycardia, i.e. the phenotype) to its cause (the mutations, i.e. the genotype) by analysing the results of simulations (run on GPU) of the action potential of human SAN cells on system of increasing complexity and physiologic resembling.

To achieve this, the work was split in two parts: in the first one a tool to load, display, analyse, fit and export electrophysiological data was developed during an internship at Elements Srl (Chapter 2). This was later used to reproduce the results of the study from Servatius in order to extract the relative decrease of the funny current conductance (g_f) in case of mutation with respect to the Wild Type condition. This feature was then given as an input to the Fabbri human SAN single cell model, to asses the decrease in terms of pacing frequency due to the mutations. The result was a Cycle Length of 1019 ms, compared to the 814 ms of a healthy cell. This translates into a frequency of 58.9 bpm instead of 73.7 (-20.1 %). The effect of an anti-arrhythmic drug to which the patient was subject, the amiodarone, was also simulated: the combined effect of the mutations and this drug pushes the CL up to 1030 ms (frequency = 58.3 bpm, -20.9 %), while the effect of amiodarone alone was lighter (CL = 946 ms, frequency = 63.4 bpm, -14 %).

The second part first presents how the 1D and 2D models were designed

and implemented (Chapter 3) and then shows the obtained results. Particularly, simulations with increasing values of cellular heterogeneity ($\sigma = 0$, 0.05, 0.1, 0.1873, 0.3 and 0.4) and gap junction resistivity ($\rho = 10, 100, 1000, 10000$ and $\rightarrow \infty \, \mathrm{M\Omega \cdot m}$) were run, in order to test the effect of cellular heterogeneity and coupling. The results (in terms of CL, APA and CV), show many interesting aspects: at the increase in cellular heterogeneity, the mean CL generally decreases since fast-pacing cells try to drive all the others. This depends on the strength of the coupling between each cell: if gap junction resistivity is too low ($\rho = 10/100 \, \mathrm{M\Omega \cdot m}$) fast cells are slowed down by the slow ones (since the latters constitute a too big electrical load for them), whereas if it is too high ($\rho = 10000 \, \mathrm{M\Omega \cdot m}$) a too little current flow is permitted and the mean CL is longer, since fast cells can not drive the other ones. For the intermediate values of ρ tested ($\rho = 1000 \, \mathrm{M\Omega \cdot m}$) at high σ (0.3/0.4), the shortest CLs are obtained. However, it is necessary to note that for physiological values of ρ ($\sim 100 \ \mathrm{M\Omega \cdot m}$) and σ (0.1873), the mean CL is the most similar to the nominal single cell value (814 ms) both in 1D (746) and 2D (794), in the WT condition. The fact that these results are lower than the nominal value (especially the 1D case) can be explained considering that an isolated fiber or tissue is not the physiologic working condition for a 3D complex-shaped structure as the SAN. Indeed, in the 1D and 2D models cells have less connections, therefore fast-pacing cell see a smaller electrical load and achieve to drive other cells in a greater extent.

Cellular synchronization is again the result of a trade-off between heterogeneity and resistivity: the bigger the σ indeed, the wider the dispersion in the parameters tends to be, but this is only true for poor couplings, since low resistivities allow a complete synchronization (in terms of CL) even with $\sigma = 0.3/0.4$ both in 1D and 2D.

What has just been said is also true for the DM condition, which anyway provides a greater relative shortening of the CL (with respect to the WT case) thanks to cellular heterogeneity: the shortest mean CL obtained is 384 ms (from 1019 ms, -62.3 %) with respect to the 370 ms of the WT condition (from 814, -54.5 %). Both these results were obtained with the maximum cellular heterogeneity simulated and $\rho = 1000 \, \mathrm{M\Omega \cdot m}$, that represents a halfway condition in which fast-pacing cells manage to deliver enough current to drive other cells, but without being slowed down by the huge electrical load they represent. This proves how cellular heterogeneity is a feature that represents a factor of robustness of biological system. Nevertheless, for physiological values of ρ and σ, in 2D the shortening is too weak (CL = 997 ms), thus proving the bradycardic effect of the mutations. In 1D the shortening is substantial (845 ms), but - as previously discussed - this result is mainly due to the unrealistic working condition and is therefore less reliable than the 2D one. Another effect of the mutation is the tendency to have - with poor cellular couplings - a more dispersed CL distribution. This is

due to a "geometric effect" - known in literature - for which longer CLs are more sensitive to little variation of current and therefore are intrinsically more variable. In other words, if the MDP and the TOP (i.e. Take-Off Potential, the membrane voltage value at which the AP is triggered) are fixed, a longer CL implies that the straight line connecting this two points (which approximates the diastolic depolarization phase) has a lower slope. Being $\delta V/\delta t$ this slope, the equation governing this phenomenon

$$\frac{\delta V}{\delta t} = \Sigma\, I_{ion}$$

tells that a low slope is obtained with a little total current; if the latter has a variation, this variation is relatively bigger with respect to the one that would be obtained with a higher slope. Therefore, this higher sensitivity explains the intrinsically bigger variability of slower cells. One more explanation could be that a smaller I_f (due to the mutations) leads to a weaker mutual driving by the cells, which in turn find it more difficult to couple with one another. However, this is not reported in literature and therefore remains only an hypothesis.

About the APA, the results show how cells tend to couple this feature in a lesser extent with respect to the CL. However, similarly to the CL, the mean APA is a trade-off between ρ and σ: the higher the cellular heterogeneity, the more dispersed the APA distribution is, but only for intermediate ranges of ρ. If this is too low indeed, all the cells are coupled at a value similar to the nominal one; if this is too high, cells can not influence each other and therefore the AP has an amplitude similar to 85.3 mV (the nominal value).

The decrease in pacing frequency and the larger dispersion of CL with high resistivities seem to be the only effects the mutations have on the models. Conduction velocity is indeed not affected: in 1D it is 12.8 cm/s for the WT condition and 12.2 cm/s for the DM one; in 2D it is 10.8 cm/s along the x axis (12.1 cm/s on the y direction) in the WT case and 10.3 cm/s (11.1 cm/s) in the DM one. It is necessary to highlight the fact that these results were obtained with physiologic values of cellular heterogeneity (σ = 0.1873) and ρ. Actually, these values were defined as "physiologic" precisely because they provide values of CV similar to the ones reported in literature. For the latter, in the 2D case a value of 100 $\mathrm{M\Omega \cdot m}$ was selected, since it provided a measure of CV similar to the ones reported in literature. In 1D instead, a lower resistivity (50 $\mathrm{M\Omega \cdot m}$) had to be used, since in this case there are less cellular connections (2 instead of 4) and thus the signal is transmitted with less efficacy. Again, this demonstrates that the 1D model lacks in reproducing the behaviour of a real 3D sinoatrial node, in which ρ could be, realistically, higher.

The main limitations of this work are indeed due to the fact that the mod-

els provide a simplified description of many features that can be found inside a real human sinoatrial node. First of all, the human SAN is a 3D structure with a complex shape. Here, only a straight fiber or a planar tissue are investigated. Second, its cells are not homogeneous but differ in shape, size, electrophysiological properties and so on; in this work cellular heterogeneity was taken into account in terms of main electrophysiological properties, but the transition from central SAN to the atrium was not considered, despite the importance of this characteristic for the effective functioning of the SAN. Finally, the SAN is not a structure which stands alone, but is surrounded by - and connected to - the right atrium, which constitutes an extraordinarily large electrical load. Other limitations could be the restricted number of cells taken into account, and the absence of fibroblasts or non-excitable tissue, which can alter the electrical behaviour of the sinoatrial node.

For these reasons the major improvements that could be carried out to these models are:

- the extension of the models to the 3D case;
- the increase in the number of simulated cells;
- the implementation of a gradient in the cellular properties from the centre of the SAN to its periphery;
- adding of the electrical load represented by the atrium;
- the inclusion of fibroblasts, blood vessel or other anatomical structure present in the SAN.

To conclude, these advances in the mathematical description of the human SAN could help to understand more deeply the functioning of a structure so important for our life. Besides this, these improvements could also lead to the possibility of simulating the effects of pathologies (such as arrhythmias) or other diseased conditions, thus providing a useful tool for the treatment of cardiac patients.

This work proposes itself as a step towards this direction.

Ringraziamenti

Non pensavo, tra le difficoltà dei primi anni di università, che sarei potuto arrivare fino a questo punto essendomi tolto così tante soddisfazioni.

Sicuramente la prima - dato che riguarda strettamente questo lavoro - è l'aver accresciuto la mia preparazione scientifica. Per quanto questa sia sicuramente ancora lacunosa (per demerito mio) e migliorabile sotto molti aspetti, ho imparato tanto durante la mia carriera scolastica, ma soprattutto durante questi mesi di redazione della tesi. Questo lo devo in primo luogo al Professor Severi, che mi ha permesso di costruire un progetto articolato e davvero interessante, e ai ragazzi di Elements, da cui tutto è partito. Ringrazio in particolare Federico, che mi ha dato la possibilità di svolgere il tirocinio per tesi presso questa azienda all'avanguardia, e Filippo, che mi ha attentamente seguito durante la mia permanenza in Elements, svelandomi molti trucchi di Matlab. Un ringraziamento speciale va ad Alan, che mi ha aiutato nella seconda parte della tesi e ha speso tonnellate di ore a correggere le bozze dell'elaborato e migliorare questo lavoro.

L'altro grande traguardo - spero non definitivo - è l'essere cresciuto come persona. Questo merito non va sicuramente a me, ma a tutti quelli che mi sono stati vicini in questi anni: primi fra tutti i miei genitori, che mi hanno sempre permesso di dedicarmi totalmente allo studio. Ad Eleonora ed Eleonora, rispettivamente sorella e morosa, per avermi sopportato sempre, e supportato quando serviva. A tutti i compagni di lezione e agli amici di sempre, ai professori che ho incontrato, ai miei zii e nonni dico grazie. Se sono anche solo lontanamente qualcosa di simile a un uomo, lo devo a voi. Spero in cambio di avervi aiutato almeno una volta ad essere migliori.

"La mia casa continuerà a viaggiare su due gambe
e i miei sogni non avranno frontiere"
- Che Guevara

Bibliography

[1] Keith, A., Flack, M., 1907. *The form and nature of the muscular connections between the primary divisions of the vertebrate heart*. J. Anat. Physiol. 41 (Pt 3), 172e189.

[2] Lewis, T., Oppenheimer, A., Oppenheimer, B.S., 1910. *The site of origin of the mammalian heart beat: the pacemaker in the dog*. Heart II, 147e169.

[3] James, T.N., 1961. *Anatomy of the human sinus node*. Anat. Rec. 141, 109e139.

[4] Li, N., Kalyanasundaram, A., Hansen, B.J. et al. *Impaired neuronal sodium channels cause intranodal conduction failure and reentrant arrhythmias in human sinoatrial node*. Nat Commun 11, 512 (2020). https://doi.org/10.1038/s41467-019-14039-8

[5] Csepe, T. A., Zhao, J., Hansen, B. J., Li, N., Sul, L. V., Lim, P., ... Fedorov, V. V. (2016). *Human sinoatrial node structure: 3D microanatomy of sinoatrial conduction pathways*. Progress in biophysics and molecular biology, 120(1-3), 164–178. doi:10.1016/j.pbiomolbio.2015.12.011

[6] Joyner, R.W., van Capelle, F.J., 1986. *Propagation through electrically coupled cells. How a small SA node drives a large atrium*. Biophys. J. 50 (6), 1157e1164.

[7] HODGKIN, A. L., & HUXLEY, A. F. (1952). *A quantitative description of membrane current and its application to conduction and excitation in nerve*. The Journal of physiology, 117(4), 500–544. doi:10.1113/jphysiol.1952.sp004764

[8] Noble D. (2007). From the Hodgkin-Huxley axon to the virtual heart. The Journal of physiology, 580(Pt 1), 15–22. doi:10.1113/jphysiol.2006.119370

[9] Y. Rudy, *From Genes and Molecules to Organs and Organisms: Heart*. In: Edward H. Egelman, editor: Comprehensive Biophysics, Vol 9, Simulation and Modeling, Harel Weinstein. Oxford: Academic Press, 2012. pp. 268-327.

[10] Servatius H, Porro A, Pless SA, Schaller A, Asatryan B, Tanner H, de Marchi SF, Roten L, Seiler J, Haeberlin A et al (2018): *Phenotypic spectrum of HCN4 mutations: a clinical case*. Circ Genomic Precis Med 11(2):e002033

[11] Fabbri, Alan (2018): *Computational modeling of human sinoatrial node: what simulations tell us about pacemaking*, [Dissertation thesis], Alma Mater Studiorum Università di Bologna. Dottorato di ricerca in Ingegneria biomedica, elettrica e dei sistemi <http://amsdottorato.unibo.it/view/dottorati/DOT547/>, 30 Ciclo.

[12] Chandler NJ, Greener ID, Tellez JO, et al. *Molecular architecture of the human sinus node: insights into the function of the cardiac pacemaker*. Circulation. 2009;119(12):1562–1575. doi:10.1161/CIRCULATIONAHA.108.804369

[13] Nikolaidou, T., Aslanidi, O. V., Zhang, H., & Efimov, I. R. (2012). *Structure-function relationship in the sinus and atrioventricular nodes*. Pediatric cardiology, 33(6), 890–899. doi:10.1007/s00246-012-0249-0

[14] Inada S, Zhang H, Tellez JO, et al. *Importance of gradients in membrane properties and electrical coupling in sinoatrial node pacing*. PLoS One. 2014;9(4):e94565. Published 2014 Apr 23. doi:10.1371/journal.pone.0094565

[15] Andrés Ricardo Pérez-Riera, Raimundo Barbosa-Barros, Rodrigo Daminello-Raimundo, Luiz Carlos de Abreu, Kjell Nikus, *Current aspects of the basic concepts of the electrophysiology of the sinoatrial node*, Journal of Electrocardiology, Volume 57, 2019, Pages 112-118, ISSN 0022-0736. https://doi.org/10.1016/j.jelectrocard.2019.08.013.

[16] Desplantez T, Dupont E, Severs NJ, Weingart R. *Gap junction channels and cardiac impulse propagation*. J Membr Biol. 2007;218(1-3):13–28. doi:10.1007/s00232-007-9046-8

[17] Li, N., Hansen, B. J., Csepe, T. A., Zhao, J., Ignozzi, A. J., Sul, L. V., … Fedorov, V. V. (2017). *Redundant and diverse intranodal pacemakers and conduction pathways protect the human sinoatrial node from failure*. Science translational medicine, 9(400), eaam5607. doi:10.1126/scitranslmed.aam5607

[18] Unudurthi, S. D., Wolf, R. M., & Hund, T. J. (2014). *Role of sinoatrial node architecture in maintaining a balanced source-sink relationship and synchronous cardiac pacemaking*. Frontiers in physiology, 5, 446. doi:10.3389/fphys.2014.00446

[19] Murphy C, Lazzara R. *Current concepts of anatomy and electrophysiology of the sinus node*. J Interv Card Electrophysiol. 2016;46(1):9–18. doi:10.1007/s10840-016-0137-2

[20] Lakatta EG, DiFrancesco D. *What keeps us ticking: a funny current, a calcium clock, or both?*. J Mol Cell Cardiol. 2009;47(2):157–170. doi:10.1016/j.yjmcc.2009.03.022

[21] Severi S, Fantini M, Charawi LA, DiFrancesco D. *An updated computational model of rabbit sinoatrial action potential to investigate the mechanisms of heart rate modulation*. J Physiol. 2012;590(18):4483–4499. doi:10.1113/jphysiol.2012.229435

[22] Himeno Y, Toyoda F, Satoh H, et al. *Minor contribution of cytosolic Ca2+ transients to the pacemaker rhythm in guinea pig sinoatrial node cells*. Am J Physiol Heart Circ Physiol. 2011;300(1):H251–H261. doi:10.1152/ajpheart.00764.2010

[23] DiFrancesco D. *Pacemaker mechanisms in cardiac tissue*. Annu Rev Physiol. 1993;55:455–472. doi:10.1146/annurev.ph.55.030193.002323

[24] Biel M, Schneider A, Wahl C. *Cardiac HCN channels: structure, function, and modulation*. Trends Cardiovasc Med. 2002;12(5):206–212. doi:10.1016/s1050-1738(02)00162-7

[25] Ramírez D, Zúñiga R, Concha G, Zúñiga L. *HCN Channels: New Therapeutic Targets for Pain Treatment*. Molecules. 2018;23(9):2094. Published 2018 Aug 21. doi:10.3390/molecules23092094

[26] Altomare C, Terragni B, Brioschi C, et al. *Heteromeric HCN1-HCN4 channels: a comparison with native pacemaker channels from the rabbit sinoatrial node*. J Physiol. 2003;549(Pt 2):347–359. doi:10.1113/jphysiol.2002.027698

[27] Li N, Csepe TA, Hansen BJ, et al. *Molecular Mapping of Sinoatrial Node HCN Channel Expression in the Human Heart*. Circ Arrhythm Electrophysiol. 2015;8(5):1219–1227. doi:10.1161/CIRCEP.115.003070

[28] Verkerk AO, Wilders R. *Pacemaker activity of the human sinoatrial node: an update on the effects of mutations in HCN4 on the hyperpolarization-activated current*. Int J Mol Sci. 2015;16(2):3071–3094. Published 2015 Jan 29. doi:10.3390/ijms16023071

[29] P. Welch (1967): *The use of fast Fourier transform for the estimation of power spectra: A method based on time averaging over short, modified periodograms*, in IEEE Transactions on Audio and Electroacoustics, vol. 15, no. 2, pp. 70-73. doi: 10.1109/TAU.1967.1161901

[30] *Unofficial Guide to the ABF File Format:* https://github.com/swharden/pyABF/tree/master/docs/advanced/abf-file-format

[31] *Axon^{TM} Binary File Format (ABF) User Guide:* http://mdc.custhelp.com/euf/assets/software/FSP_ABFHelp_2.03.pdf

[32] *Abfload script:* https://github.com/fcollman/abfload

[33] Verkerk AO, Wilders R, van Borren MM, et al. *Pacemaker current (I(f)) in the human sinoatrial node*. Eur Heart J. 2007;28(20):2472–2478. doi:10.1093/eurheartj/ehm339

[34] Baruscotti, M., Bucchi, A., Viscomi, C., Mandelli, G., Consalez, G., Gnecchi-Rusconi, T., ... DiFrancesco, D. (2011). *Deep bradycardia and heart block caused by inducible cardiac-specific knockout of the pacemaker channel gene Hcn4*. Proceedings of the National Academy of Sciences of the United States of America, 108(4), 1705–1710. doi:10.1073/pnas.1010122108

[35] Crumb WJ, Vicente J, Johannesen L, Strauss DG. *An evaluation of 30 clinical drugs against the comprehensive in vitro proarrhythmia assay (CiPA) proposed ion channel panel*. Journal of Pharmacological and Toxicological Methods. 2016;81:251–262. doi: 10.1016/j.vascn.2016.03.009.

[36] Xinrong Fan, Yongjun Chen, Pan Wu, Junlian Xing, Hui Chen, Tao Song, Jing Yang, Jun Zhang, Congxin Huang. *Novel electropharmacological activity of amiodarone on human HCN channels heterologously expressed in the Xenopus oocytes*, European Journal of Pharmacology, Volume 669, Issues 1–3, 2011, Pages 15-2, ISSN 0014-2999, https://doi.org/10.1016/j.ejphar.2011.07.039.

[37] *How to Optimize Data Transfers in CUDA C/C++*. https://devblogs.nvidia.com/how-optimize-data-transfers-cuda-cc/

[38] Anja Hagen, Anna Dietze, Stefan Dhein, *Human cardiac gap-junction coupling: effects of antiarrhythmic peptide AAP10*, Cardiovascular Research, Volume 83, Issue 2, 15 July 2009, Pages 405–415, https://doi.org/10.1093/cvr/cvp028

[39] A. Giovannini. *Parametric sensitivity analysis of the most recent computational models of rabbit cardiac pacemaking*. Bachelor's thesis, Biomedical Engineering, 2012

[40] Koussis, Jonathan (2017), *Analisi degli effetti dell'eterogeneità cellulare di un tessuto del nodo seno-atriale simulato attraverso la parallelizzazione in CUDA*. [Laurea magistrale], Università di Bologna, Corso di Studio in Ingegneria biomedica [LM-DM270] - Cesena <http://amslaurea.unibo.it/view/cds/CDS8198/>

[41] Campana, Chiara (2015), *A 2-dimensional computational model to analyze the effects of cellular heterogeinity on cardiac pacemaking*. [Laurea magistrale], Università di Bologna, Corso di Studio in Ingegneria biomedica [LM-DM270] - Cesena <http://amslaurea.unibo.it/view/cds/CDS8198/>

[42] CUDA installation guide. https://docs.nvidia.com/cuda/cuda-installation-guide-microsoft-windows/index.html

[43] GPU Coder prerequisites. https://it.mathworks.com/help/gpucoder/gs/install-prerequisites.html

[44] Code Generation by Using the GPU Coder App. https://it.mathworks.com/help/gpucoder/gs/gpu-code-generation-using-app.html

[45] CUDA Programming Information and Resources. http://cuda.ce.rit.edu/cuda_overview/cuda_overview.htm

[46] Introduction to GPUs. https://nyu-cds.github.io/python-gpu/02-cuda/

[47] Marco Nobile, Paolo Cazzaniga, Daniela Besozzi, Dario Pescini, Giancarlo Mauri. (2014). *cuTauLeaping: A GPU-Powered Tau-Leaping Stochastic Simulator for Massive Parallel Analyses of Biological Systems*. PloS one. 9. e91963. 10.1371/journal.pone.0091963.

[48] Measure and Improve GPU Performance https://it.mathworks.com/help/parallel-computing/measure-and-improve-gpu-performance.html